

**Breakdown of the
rotating wave
approximation in
sideband transitions
between a
superconducting
qubit and cavity**

Wouter Kessels



Master's thesis

Breakdown of the rotating wave approximation in sideband transitions between a superconducting quantum bit and cavity

by

Wouter Kessels

to obtain the degree of Master of Science
at the Delft University of Technology,
to be defended publicly on Wednesday March 18, 2020 at 14:30.

Student number: 4201248
Project duration: August 19, 2019 – March 18, 2020
Thesis committee: Prof. dr. Gary Steele, TU Delft, supervisor
Prof. dr. Sander Otte, TU Delft
Prof. dr. Simon Gröblacher, TU Delft
Byoung-moo Ann, TU Delft

A digital version of this thesis is available at <http://repository.tudelft.nl/>.



Abstract

The atomic beam experiment captures the fundamental interaction between matter and individual quanta of light. Control over the photonic state of the cavity will contribute to our understanding of this interaction and applications in the field of quantum engineering.

This thesis focusses on two-photon sideband transitions to control the effective coupling between an artificial atom and a cavity. A superconducting transmon qubit plays the role of the atom and a coplanar waveguide resonator mimics the cavity.

Based on numerical simulations with experimentally relevant parameters, we show that the rotating wave approximation on the Duffing oscillator's self-interaction and on the counter-rotating drive terms breaks down for sideband transitions. We demonstrate that the transition rates in a Kerr oscillator deviate significantly from those in a Duffing oscillator by up to a factor 2.8. The counter-rotating drive terms increase the transition rate by a maximum factor of 3.

Furthermore, measurements of sideband transition rates on a superconducting chip show an agreement of 57% to 65% with simulated transition rates, showing that our model has been able to capture the major relevant physical interactions.

Acknowledgements

Major gratitude I owe to *Gary Steele* and *Byoung-moo Ann* for introducing me to the wondrous world of superconducting qubits. With your guidance, experience, and our endlessly inspiring discussions, this thesis project has been an epic journey to become the cherry on my educational cake.

Gary, I like your strong personality. You have always given me honest and direct feedback. I was there to learn, so to my experience that has been a perfect match. It's not only the physics content that you taught me. Our research is cool but it is useless if we cannot transfer it to others. You have drilled me to focus on how to get the message across, how to sell my ideas, and to present my findings. Those skills are applicable to anything at anytime in life. As a final word of praise, I know that the days of a professor are filled with meetings, musts, stress, and, above all, a lack of sleep. But when I see you in the morning, carefully weighing the grounded coffee beans and frothing milk for your cappuccino, it is the eagerness to keep learning about physics that keeps you going every day. I find that inspiring.

Byoung-moo, I have been fortunate to have had such a great collaboration with you. I know supervising a student is demanding, but I have tried my very best to give as much as possible in return and to challenge you as well. We've had numerous deep discussions about extremely specific topics from which we both came out wiser. I am thankful for everything, from theoretical to experimental, that you taught me, for you letting me be part of your larger research, and for you being a very dedicated mentor.

I wouldn't have come close to this point of graduation if it weren't for my parents, *Han* and *Annet*. From my very early days you have supported me in becoming what I want to become. When I wanted to become an architect, you got my back. When I quit and chose to study physics, you got my back. The fascination for nature had actually always been at home, so it was no wonder that, even though I had no idea what to do with it, I chose physics. Just because I wanted to know how the universe works. As long as I chose what I was thrilled about, you supported me with everything you could. I am forever grateful that you have given me all the opportunities to have the best and most fruitful student days possible.

Sascha, where would I be without you. Especially during the last seven months you have been my rock. We are both deeply driven to achieve our goals, but we realize that life is much less fun if we do not vividly and consciously enjoy it. We have had numerous effective study sessions until late hours, but also, at times when stress levels seemed way harder to control than physics, you dragged me away from my computer to go out and don't think about work for a moment. Everything can wait, for example, when we go to Lisbon for a weekend. But all the times I had to work until late, you were completely understanding. That balance has kept me on track. I believe the two of us make the greatest team.

There are many more people that deserve special words of gratitude here. Let me start with the *Steele Lab team*. You guys have been inspiring to me and always eager to help. I know the world of academia is extremely demanding. Nonetheless, you have always been readily available whenever I had a question about anything. That makes for a very pleasant working environment.

I would like to thank my brother, *Stijn*, for the tight front cover's artwork. I wouldn't ever be able to produce a thesis without worrying about the looks. Your expertise on graphics and visualization has helped me give this report and my presentation slides just that bit of extra aesthetic care.

Most of the time me working on this project I have spent with my close friends of the AP Bikkels —*Hidde, Hina, Huib, Inge, Lisa, Max, Mees, Olaf, and Peter*. We've all run in different directions but still we stay closely in touch, especially after moving into the Penthouse. Always starting the day with a coffee break, having lunch at the same familiar purple couch, and keeping up an effective but relaxed working atmosphere has been a major pleasure. Furthermore, special thanks I devote to *Hina* for shooting and editing the GIF animation as part of my invitations.

Many thanks go as well to the independent members of my assessment committee *Sander Otte* and *Simon Gröblacher* for taking the time and effort to read this thesis, putting my knowledge to the test, and being part of my process of becoming an engineer.

Finally, I want to thank *you*, the reader, for reading this thesis and at least having partial interest in the work that I've done over the last seven months. Whether you have a background in (quantum) physics or something completely different, I sincerely hope you enjoy reading my work.

It has been an incredible journey.

Wouter

Contents

List of abbreviations	3
List of symbols	5
1 Motivation	7
1.1 The atomic beam experiment	8
1.2 The experiment on a chip	8
1.3 Related work	9
1.4 More applications of superconducting quantum circuits	9
1.5 Structure of the thesis	10
2 Theory of circuit quantum electrodynamics	11
2.1 The transmon qubit	12
2.1.1 The Josephson junction	12
2.1.2 The Cooper pair box	12
2.1.3 The transmon regime	13
2.1.4 Coupling to a cavity	15
2.1.5 Three representations of the transmon qubit	16
2.2 Consequences of the qubit-cavity coupling	18
2.2.1 Resonant coupling	18
2.2.2 Dispersive coupling	18
2.2.3 Beyond the Jaynes-Cummings model	19
2.3 Sideband transitions	20
2.3.1 The sideband drive	20
2.3.2 Determining the drive frequency	21
2.3.3 Impact of the drive on the qubit resonance	21
2.3.4 Sideband coupling	21
2.4 Interaction with the environment	22
2.4.1 Depolarization	22
2.4.2 Dephasing	23
2.4.3 Time evolution of an open quantum system	23
3 Methodology	25
3.1 Numerical simulations	26
3.1.1 Time evolution solver	26
3.1.2 Rise and fall	26
3.1.3 Batches	27
3.1.4 Sideband resonance condition	27
3.1.5 Convergent method	27
3.1.6 Transition rate	28
3.1.7 Parameters	29
3.2 Measurements	29
3.2.1 Cryogenic setup	29
3.2.2 Noise reduction	30

3.2.3 Device parameters	31
3.2.4 Sideband transitions	33
4 Results & discussion	35
4.1 Comparison of the Duffing and Kerr approximation	36
4.2 Counter-rotating drive terms	37
4.3 Experimental demonstration of sideband transitions	37
4.3.1 Red sideband transitions	38
4.3.2 Blue sideband transitions	40
5 Conclusions	43
6 Outlook	45
Bibliography	49
Appendices	53
A Simulations of the atomic beam experiment	55
A.1 Setup	55
A.2 Results	57
B Measurement and fitting data	59
C Analytical derivation of the sideband coupling	61
D Drive effects on the qubit	63
D.1 Kerr oscillator	63
D.2 Duffing oscillator	64
D.3 Two-level system	64
E Derivation of the sideband fitting models	67
E.1 Blue sideband transitions	67
E.2 Red sideband transitions	68
F Simulations of the quantum Rabi model	69
F.1 Results	70
G Bichromatic driving	71
H Simulation results	73

List of abbreviations

AC	alternating current
ASG	arbitrary signal generator
CPB	Cooper pair box
CPW	coplanar waveguide
DC	direct current
FWHM	full-width-half-maximum
IF	intermediate frequency
LME	Lindblad master equation
LO	local oscillator
LPF	lowpass filter
QED	quantum electrodynamics
QND	quantum non-demolition
RAM	random-access memory
RF	radio frequency
RWA	rotating wave approximation
SB	sideband
TLS	two-level system
VNA	vector network analyzer

List of symbols

$\hat{a}^{(\dagger)}$	cavity (creation) annihilation operator
$\hat{b}^{(\dagger)}$	qubit (creation) annihilation operator
\hat{C}	collapse operator
C_B	shunt capacitance
C_g	gate capacitance
C_J	capacitance of the Josephson junction
C_Σ	total capacitance
e	electron charge, exponential
$ e\rangle$	qubit first excited state
E	energy
E_C	charging energy
E_J	Josephson energy
$ f\rangle$	qubit second excited state
g	bare qubit-cavity coupling strength
$ g\rangle$	qubit ground state
g_s	qubit-storage cavity coupling strength
g_{sb}	effective sideband coupling strength
h	Planck constant
\hbar	reduced Planck constant, $h/2\pi$
$\hat{\mathcal{H}}$	Hamiltonian operator
$\hat{\mathcal{H}}_c$	Hamiltonian operator of the cavity
$\hat{\mathcal{H}}_{CPB}$	Hamiltonian operator of the Cooper pair box
$\hat{\mathcal{H}}_d$	Hamiltonian operator of the drive
$\hat{\mathcal{H}}_D$	Hamiltonian operator of the undriven Duffing system
$\hat{\mathcal{H}}_g$	Hamiltonian operator of the qubit-cavity interaction
$\hat{\mathcal{H}}_{JC}$	Jaynes-Cummings Hamiltonian operator
$\hat{\mathcal{H}}_K$	Hamiltonian operator of the undriven Kerr system
$\hat{\mathcal{H}}_R$	Rabi Hamiltonian operator
$\hat{\mathcal{H}}_q$	Hamiltonian operator of the qubit
k_B	Boltzmann constant
L_J	Josephson inductance
\hat{n}	number operator of Cooper pairs
$ n\rangle$	qubit charge number state
n_{ac}	AC gate charge, rms number of vacuum induced Cooper pairs
n_{dc}	DC gate charge
n_g	gate (offset) charge
N_c	number of simulated cavity levels
N_q	number of simulated qubit levels
P	probability
P_d	drive power at the ASG output port
P_{VNA}	probe power at the VNA output port
Q	quality factor
R	cost function
S_{21}	measured cavity transmission coefficient
t	time
T	temperature

T_1	depolarization time
T_2	dephasing time
T_{bulk}	simulation time between the rise and fall
T_{fall}	simulation falling time
T_{rise}	simulation rising time
T_{tot}	total simulation time, $T_{\text{rise}} + T_{\text{bulk}} + T_{\text{fall}}$
$\hat{\mathcal{U}}$	unitary operator
$\hat{\alpha}^{(\dagger)}$	cavity-like normal-mode annihilation (creation) operator
$\hat{\beta}^{(\dagger)}$	qubit-like normal-mode annihilation (creation) operator
γ	qubit linewidth
γ_1	qubit depolarization rate
γ_2	qubit dephasing rate
$\delta\omega_q$	driven qubit frequency shift
Δ_{ij}	difference frequency, $\omega_i - \omega_j$
ϵ_d	drive strength
ϵ_p	probe strength
ζ_c	dressed cavity anharmonicity
ζ_g	undressed qubit anharmonicity
$\tilde{\zeta}_q$	dressed qubit anharmonicity
η	driven qubit frequency modulation
θ_R	Rabi angle
κ	cavity linewidth
κ_1	cavity depolarization rate
κ_2	cavity dephasing rate
λ	wavelength
$\hat{\rho}$	density matrix operator
$\hat{\sigma}_i$	i -component Pauli matrix
$\hat{\sigma}_+$	Pauli creation operator
$\hat{\sigma}_-$	Pauli annihilation operator
Σ_{ij}	sum frequency, $\omega_i + \omega_j$
φ	gauge-invariant phase difference
$\hat{\varphi}$	gauge-invariant phase difference operator
χ	AC Stark shift
χ_c	cavity self-Kerr
χ_q	qubit self-Kerr
χ_{qc}	qubit-cavity cross-Kerr
$ \psi\rangle$	quantum state
ω_c	angular undressed cavity frequency parameter
$\tilde{\omega}_c$	angular dressed cavity frequency
ω_d	angular drive frequency
ω_p	angular probe frequency
ω_q	angular undressed qubit frequency parameter
$\tilde{\omega}_q$	angular dressed qubit frequency
Ω_{sb}	angular sideband transition rate



1. Motivation

As physicists we try to grasp the fundamentals of nature. We want to understand why the universe works as it does, and why we see what we see. One of the most fundamental interactions around us are those between matter and light. This interaction gives colour to our planet Earth, satellite navigation to our smartphones, and to living creatures the ability to bathe in the sun. If we really want to understand this interaction between light and matter, we have to dig into it to its most fundamental form —when a single photon meets a single atom. At these smallest scales, quantum mechanics runs the show. Specifically, it is the field of quantum electrodynamics that describes the interaction between quantized matter with a quantized electromagnetic field. To test our existing theories, we have to measure them at the scales of individual quanta. These scales have long been out of reach for scientists, until the last few decades. In this thesis, we will explore the interaction between a single artificial atom and a single quantum of light.

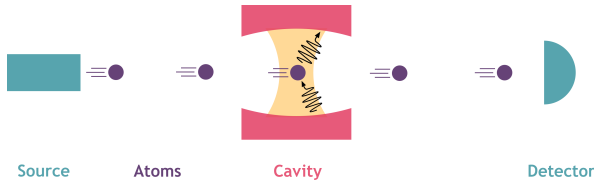


Figure 1.1: Simple, schematic setup of the atomic beam experiment. A source produces atom that pass through a cavity. Inside the cavity, these atoms interact coherently with the cavity field. Subsequently, they leave the cavity and are picked up by a detector. By measuring the phase shift of the atoms after they have interacted with the cavity, a non-demolition measurement can be performed of a single photon inside the cavity.

1.1 The atomic beam experiment

The atomic beam experiment of Serge Haroche has accomplished to observe and control individual quanta of light [1, 2]. In this experiment, a source shoots off circular Rydberg atoms that are subsequently prepared into a superposition state between the ground state $|g\rangle$ and excited state $|e\rangle$. Next, they pass through a cavity, which consists of two highly reflective mirrors. While the atom is in between these mirrors, the quantum nature of the atom and the cavity field gives rise to coherent exchange of a single excitation [3]. From an experimental point of view, it is very challenging to detect the interaction between an individual atom and photon due to the weak coupling between light and matter. But when the atom is trapped between two highly reflective mirrors, the probability of interaction between the photon and the atom is strongly increased [4]. The field of physics that studies these interactions inside a cavity is known as cavity quantum electrodynamics (cavity QED).

When the atom leaves the cavity, it has experienced a phase shift if a single photon is left inside the cavity. Normally, when you observe a photon, it is absorbed by your eye or by a photodetector. But in his experiment, Haroche has accomplished to determine the presence of a single photon inside the cavity without destroying it. Although it was Braginsky who in 1977 first proposed the idea of such a quantum non-demolition measurement [5], it was Haroche who managed to perform one. In 2012 Serge Haroche and David J. Wineland [6] were both rewarded the Nobel prize “for ground-breaking experimental methods that enable measuring and manipulation of individual quantum systems.” [7]

1.2 The experiment on a chip

This thesis is part of the larger project to perform the atomic beam experiment on a solid-state chip with the aim to control the photonic state of the cavity. On a chip, instead of physically shooting real atoms through a

cavity, we imitate the atomic beam experiment in an all-electrical circuit. The field of research on the quantum behaviour of light-matter interaction in electrical circuits is known circuit quantum electrodynamics (circuit QED). In our circuitry, the atom is represented by a superconducting¹ transmon quantum bit (qubit),² and the optomechanical cavity by an electrical resonator. The amazing thing is that the transmon qubit is visible by the naked eye and is built up from billions and billions of atoms, but it has a quantized set of energy levels and in some ways really behaves as a single atom.

The big advantage of circuit QED is that the properties of all our circuit elements can be engineered [9]. Especially for the atoms, where in cavity QED we are limited by the atoms nature provides us, in circuit QED we can produce and tune all the shapes, parameters and characteristics ourselves (and in some setups even tune *in situ*), only limited by our fabrication techniques and imagination. Furthermore, the large size of the artificial atom gives the potential for much stronger coupling between the qubit and the on-chip cavity. This is because the qubit's effective dipole moment can be orders of magnitude larger than those of alkali and Rydberg atoms, which are typically used in cavity QED [3]. In the newly emerged parameter regimes, the coupling strengths overwhelm the decay rates, which allow for strong coherent interactions [10]. These regimes have made it possible to experimentally test phenomena in quantum optics that were long only theoretically predicted [11]. Finally, the quantum dynamics on our macroscopic chip can be conveniently controlled with classical microwave light fields.

An important difference between cavity and circuit QED is that in the latter, the artificial atom cannot physically move, nor can the cavity. They stay mounted and fixed on the chip under all circumstances. One may wonder how this allows for imitating the atomic beam experiment, where the atoms spatially pass through the cavity. To this extend we locate the qubit and cavity close to each other on the chip, but engineer them to have very different excitation energies. When we leave the chip at rest, there is no energy exchange between the qubit and cavity, because the excitation

¹Superconducting means that there is zero electrical resistance when an electrical current is present. This remarkable phenomenon appears for certain materials below a specific critical temperature T_C . Below T_C , it is energetically favourable for electrons to pair up, which makes them behave as spin-1 bosons, resulting in the total loss of electrical resistance [8].

²A quantum bit is the quantum analogue of a classical bit. Where the classical bit can be either 0 or 1, the quantum bit can be any combination of the two. There are numerous types of quantum bits possible in both cavity and circuit QED. The only requirement they have to satisfy is that they have at least two accessible states that exhibit quantum properties [4].

of one requires a different amount of energy than the excitation of the other. This situation mimics the atom being outside of the cavity.

The other situation, where the atom is inside the cavity and does exchange energy with it, can be created in different ways. One way is by using a superconducting loop, interrupted by two Josephson junctions (called a SQUID [12]). This loop can be used as a qubit of which we can tune the resonance frequency *in situ* by applying a magnetic field through the loop. To mimic the atom passing through the cavity, we tune the qubit to resonance with the cavity, which results in coherent interaction between the two. The disadvantage of this method is that the SQUID is very sensitive the flux noise, which reduces the decoherence time.

Another way to let the qubit and cavity coherently interact is by irradiating a single-junction qubit with a microwave light field. When the frequency and intensity of the light field are just right, it induces transitions between the qubit and cavity. These are called *sideband transitions*. Within this thesis project, we have chosen for the latter method to mimic the atom's passage through the cavity. It is the generation of these sideband transitions that is the focus of this thesis.

1.3 Related work

So far, the atomic beam experiment has not yet been performed on a chip. Some pioneers have made great leaps in the last 16 years, though, that provide us with the tools for our experiment. In 2004 Nature published the work of Wallraff et al. on the first strong coherent interaction between a superconducting qubit and cavity on a chip [3]. This marked the birth of circuit QED.

For a superconducting circuit element to function as an artificial atom, it is required to be sufficiently anharmonic in its energy level spacings, so that different transitions can be controlled separately. Josephson junctions behave as nonlinear inductors [13] and play an important role in the anharmonicity. There are three types of Josephson junction-based qubits that can be used as an artificial atom —charge, phase [14], and flux [15] qubits. In this thesis, we will consider only the charge qubit, which is based on the Cooper pair box (CPB) [16]. In 2007, Koch et al. made a formidable adjustment to the existing designs. They shunted the CPB with a large capacitance, which reduced the charging energy to be many times smaller than the Josephson energy [17]. This made the qubit practically insensitive to charge noise, while maintaining sufficient anharmonicity. This qubit is known as the *transmon* qubit and is nowadays the standard in numerous applications of quantum engineering.

The required type of sideband transitions —mediated by two photons —were first demonstrated in circuit QED by Wallraff et al. in 2007 [18]. To the best of our knowledge, all studies on two-photon sideband transitions in circuit QED up to now have considered only the two-level approximation of the transmon qubit [18–20]. No such quantitative study had yet been performed on the multi-level model of the transmon qubit. The novelty of this thesis is the contribution to our understanding of two-photon sideband transitions when we do account for the higher levels of the superconducting transmon qubit.

1.4 More applications of superconducting quantum circuits

A lot of research within circuit QED is performed to explore fundamental quantum optics. People are, however, well aware of the wide landscape of possible technical applications that circuit QED brings. One of these is quantum computing. When using the possibility of quantum phenomena such as superposition and entanglement in quantum computations, the computational space grows exponentially and allows for massive parallel operations [21]. Today, circuit QED offers the leading architecture for a scalable quantum computer with many qubits [11]. In 1982, Richard Feynman already proposed to simulate one quantum system with another quantum system [22]. As a matter of fact, classical computers are inherently inefficient at modelling many complex computation problems, ranging from medicinal drug discovery to finding superconductivity at high temperatures [21]. Today there are many examples of quantum simulations of, for example, condensed-matter physics, small molecular systems [23, 24], and chemical processes [25] (an extensive overview of the applications can be found in [26]).

One remarkable paper was published last year in Nature, in which scientists from Google claim they have achieved quantum supremacy [27]. The task of their transmon-based quantum computer was to sample the output of a pseudo-random quantum circuit. It took the quantum computer 200 seconds to sample one instance 1 million times, where, according to Google's estimations, the state-of-the-art supercomputer would require 10,000 years to do the job.³ This example brings the transmon-based quantum processors a step closer to the practical use of quantum information processing.

³Though IBM responded that the computation could actually be performed in 2.5 days on their most powerful supercomputer [28].

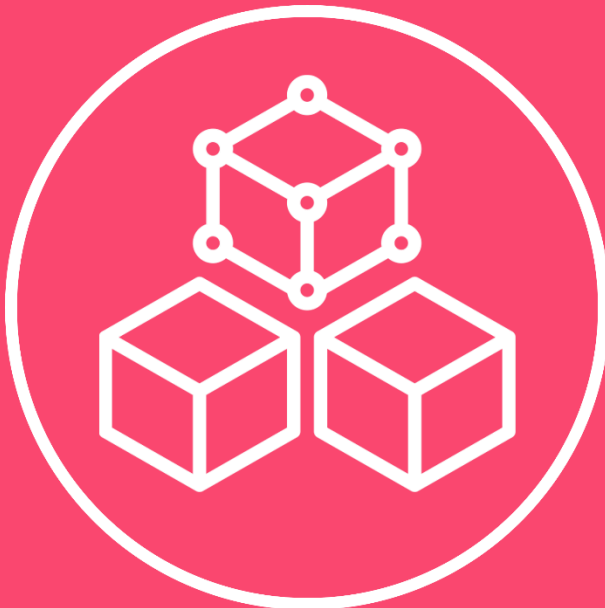
With a rigorous study on relevant phenomena in circuit QED, such as driving effects in a superconducting transmon qubit and control over the effective coupling to a cavity, we hope with this thesis to contribute to the rapidly growing field of quantum engineering.

1.5 Structure of the thesis

This thesis will proceed in the next chapter with discussing circuit QED on a theoretical level, setting the basis for our mathematical and physical understanding of the different elements and interactions on the chip. In the following chapter, we describe the methods that are used to perform numerical simulations of the sideband transitions and experimental measurements on the chip. The main results are presented and discussed in chapter 4. The conclusions of this thesis's work are combined in chapter 5 and an outlook together with recommendations for future research is given in chapter 6. Additional information and results can be found in the appendices, such as numerical simulations of the atomic beam experiment, the quantum Rabi model, and bichromatic driving.

This thesis goes deep into the quantum mechanics and mathematics, which is why I have to consider a baseline of the reader's knowledge. I assume that the reader has at least basic understanding of quantum mechanics and is familiar with its mathematical formulations.⁴

⁴Footnotes will often provide information that is natural to quantum physicists but perhaps not to most other readers.



2. Theory of circuit quantum electrodynamics

In this chapter we discuss circuit QED on a theoretical level to obtain the required understanding of the physics and of the mathematical formulations. We will start by deriving the transmon qubit and discuss three models commonly used to approximate it with —the Duffing oscillator, the Kerr oscillator, and the two-level system. The physical phenomena are discussed that appear when we couple the qubit to a cavity, and we will see how to induce the desired sideband transitions for the atomic beam experiment and what effect they have on our qubit. Finally, we will discuss the non-idealities that arise from our superconducting chip interacting with its environment.

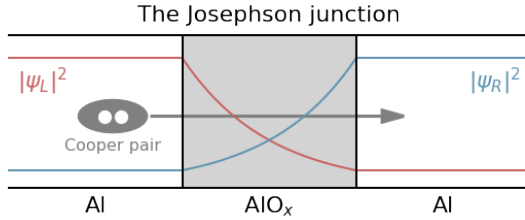


Figure 2.1: Schematic image of a Josephson junction. The squared magnitudes of the wavefunctions decay exponentially from both sides of the barrier, resulting in a finite probability of a Cooper pair tunneling through the barrier.

2.1 The transmon qubit

As our artificial atom we choose the transmon qubit. It can be viewed as an *LC*-oscillator where the linear inductor L is replaced by a non-linear one. Furthermore, the transmon qubit is characterized by its convenient insensitivity to charge noise. This section will start at the key component of the transmon qubit —the Josephson junction, and work from this point towards three useful transmon models that we will investigate in this thesis—the Duffing oscillator, the Kerr oscillator and the two-level system.

2.1.1 The Josephson junction

We start the construction of our artificial atom with the Josephson junction. This junction is built up of two superconducting electrodes, which are separated from each other by a thin insulating material [13] (see figures 2.1 and 2.2). In the superconducting state, electrons with opposite spin pair up into so-called Cooper pairs. Because of the insulating barrier, these pairs cannot be electrically conducted through the junction. Instead, they can coherently tunnel through the insulating barrier, resulting in a phase difference φ of the macroscopic wave function between one side of the barrier and the other.

Let us have a look at the mathematical description. In the presence of a potential difference V across the junction, the phase evolves like

$$\hbar \frac{d\varphi}{dt} = 2eV \quad (2.1)$$

[29], where the factor 2 comes from the fact that we consider paired electrons. The Josephson effect tells us that the current through and the voltage over the junction are related to the phase φ as

$$I_J = I_0 \sin \varphi, \quad (2.2)$$

$$V = \frac{\Phi_0}{2\pi} \frac{d\varphi}{dt}, \quad (2.3)$$

where I_0 is the maximum current that can flow through the junction, the so-called critical-current parameter. $\varphi = \phi_L - \phi_R$ is the gauge-invariant superconducting phase difference across the junction and $\Phi_0 = h/2e$ is the superconducting flux quantum. We gain more insight from these two expressions by taking the time derivative of I_J and the substitution of V . This yields the differential equation

$$\frac{dI_J}{dt} = I_0 V \frac{2\pi}{\Phi_0} \cos \varphi. \quad (2.4)$$

Furthermore, we know that an inductor is defined by

$$V = L \frac{dI}{dt}. \quad (2.5)$$

This leads us to the finding that the Josephson junction can be regarded as a non-linear inductor with a Josephson inductance $L_J = \Phi_0/(2\pi I_0 \cos \varphi)$. The effect that makes the Josephson junction an inductor is kinetic inductance, generated by the momentum of the charged Cooper pairs. We know that the Cooper pair wavefunction reduces exponentially from the boundary to the middle of the insulating barrier. This means that the probability of finding a Cooper pair in the middle of the barrier is lowest and on the edges it is highest. When Cooper pairs travel all the way across the junction, their momentum in the middle of the barrier must be larger than around the edges. This momentum is what the energy is stored in. The total energy stored in the junction is given by

$$U_J = \int VI_J dt = -E_J \cos \varphi, \quad (2.6)$$

with $E_J \equiv I_0 \Phi_0 / 2\pi$ the so-called Josephson energy, which is the energy associated with an electron tunneling across the junction.

2.1.2 The Cooper pair box

A first artificial atom is made by connecting two superconducting islands by a Josephson junction in series to a capacitor. This configuration is called the Cooper pair box (CPB) and is qualitatively described by two relevant energy scales [9, 16]. On one hand, there is the energy E_J stored in the junction as a current passes through. On the other hand, there is the charging energy $E_C = e^2/(2C_\Sigma)$ of a single electron on the capacitance, which is, in other words, the energy required to add a single electron to the capacitance [30]. Here, the total capacitance $C_\Sigma = C_g + C_J$ of the CPB to ground is the sum of the gate capacitance C_g and the effective (normally very small) capacitance C_J of the two electrodes of the Josephson junction. The Hamiltonian operator describing the total energy of the CPB is neatly derived in [21] using circuit quantization. It is given by

$$\hat{\mathcal{H}}_{\text{CPB}} = 4E_C(\hat{n} - n_g)^2 - E_J \cos \hat{\varphi}. \quad (2.7)$$

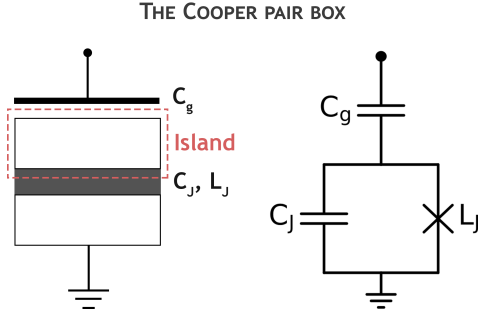


Figure 2.2: Schematic circuit representation of a Cooper pair box. The island is separated from the rest of the circuit by a capacitor C_g and the Josephson barrier.

Here, \hat{n} is the discrete number operator of Cooper pairs that have tunneled through the junction and $\hat{\varphi}$ is the operator of the gauge-invariant phase φ across the junction. $n_g = (Q_r + C_g V_g)/2e$ is the gate charge (also called offset charge), which is a continuous variable and may either intentionally, or unintentionally and uncontrollably fluctuate [17, 31]. Here, V_g is the voltage at the gate and Q_r is the offset charge induced by the environment. The factor of 4 in front of E_C follows from the fact that the charging Coulomb energy for a Cooper pair is four times as large as for a single electron [31]. The infinitely many energy levels of the CPB can be divided into two categories [32]. The first contains the levels below E_J , confined by the cosine Josephson potential. The second category contains the unconfined states, above the cosine potential. These very high excitations, however, are usually considered irrelevant and neglected.¹

We can visualize this system by a quantum rotor in a gravitational field [17]. A mass is connected to a stiff, massless rod of finite length, which can rotate around its pivot axis without friction (see fig. 2.3). In this analogy, the location of the mass is completely determined by the polar angle φ . The (discrete) angular momentum conjugate is then given by the number operator \hat{n} . The charging energy E_C becomes a measure for the moment of inertia, and the Josephson energy E_J represents the torque on the rotor, produced by the gravitational force. To capture the origin of n_g , we imagine the rotor also carrying charge and being in a uniform magnetic field, parallel to the pivot axis (perpendicular to the plane of motion). The non-zero offset charge n_g is identified by the effect to the angular momentum due to the force of the magnetic field on the charged mass.

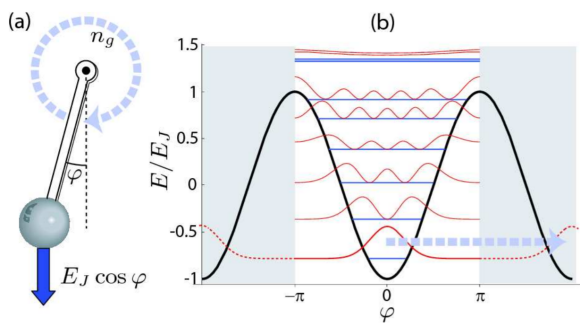


Figure 2.3: Retrieved from [17]. A quantum rotor as analogy for the Cooper pair box. The Cooper pair box can be viewed as a charged stiff-rod quantum rotor in a constant magnetic field represented by n_g . Its position is completely determined by the phase φ and its angular momentum by the discrete \hat{n} .

Charge basis representation

The CPB regime is defined by the condition $E_C \gg E_J$, so the capacitive charging of the island is the dominant energy scale in the CPB. This is why the CPB is also known as a charge qubit. In this regime it is a natural choice to capture the dynamics in the eigenbasis $|n\rangle$ of Cooper pair number operator \hat{n} , labelled by the number of excess Cooper pairs on the island [16]. \hat{n} is then defined as

$$\hat{n} = \sum_n n |n\rangle \langle n|, \quad (2.8)$$

where the sums runs from $-\infty$ to $+\infty$. The phase operator is subsequently given through the canonical commutation relation $[\hat{n}, e^{i\hat{\varphi}}] = e^{i\hat{\varphi}}$ by

$$e^{-i\hat{\varphi}} = \sum_n |n+1\rangle \langle n|. \quad (2.9)$$

Noting that we can write the cosine from eq. (2.7) into the exponential from eq. (2.9) by $\cos \hat{\varphi} = \frac{1}{2}(e^{+i\hat{\varphi}} + e^{-i\hat{\varphi}})$, we obtain the CPB's Hamiltonian in the charge basis:

$$\begin{aligned} \hat{\mathcal{H}}_{\text{CPB}} = & 4E_C \sum_n (n - n_g)^2 |n\rangle \langle n| \\ & - \frac{E_J}{2} (|n+1\rangle \langle n| + |n\rangle \langle n+1|). \end{aligned} \quad (2.10)$$

2.1.3 The transmon regime

For many applications, we require the qubit to be sufficiently anharmonic and stable in order to be useful. Let us first examine the stability of the Cooper pair box.

Stability

If we calculate the eigenenergies (height of the energy levels) of the CPB Hamiltonian as a function of the offset charge n_g in the CPB regime where $E_C \gg E_J$, we notice that the energies required to excite the CPB from one level to another are extremely strong

¹The unconfined states appear, however, to play a crucial role in the dynamics in the case of very strong driving [32].

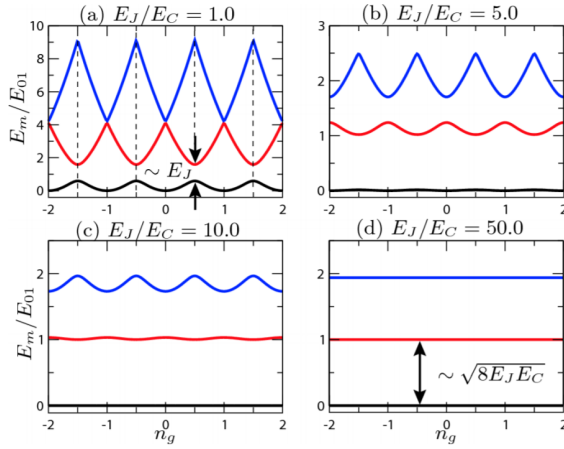


Figure 2.4: Retrieved from [17]. Energy levels for different ratios of E_J/E_C . Increasing this ratio, achieved by shunting the Cooper pair box with a large capacitance, eliminates the strong dependence on gate bias n_g and thus sensitivity to charge noise. The arrows in (a) indicate the sweet spot. The regime in (d) where $E_J \gg E_C$ is known as the transmon regime.

functions of n_g [17] (see (a) of fig. 2.4). If we were able to control the gate charge to unlimited precision, we would have stable transition energies between the levels. But in reality, electrons from the environment, zero point quantum fluctuations and imperfections in the instrumentation creating the gate bias induce fluctuations in n_g and thus in the transition frequencies. This charge dispersion subsequently results in the loss of information about the CPB's phase (see section 2.4.2).

One way to deal with this strong charge dispersion is to try to bias the gate voltage to the CPB's charge degeneracy point (at half-integer values of n_g , also known as the *sweet spot*) where the derivative of the transition frequency as a function of n_g is zero (arrows in (a) of fig. 2.4). This way, gate charge fluctuations have minimal impact on the transition frequencies.

Another method to minimize this impact was invented by Koch et al. [17], which shunts the junction by a large capacitance C_B . This minimizes the charging energy $E_C = e^2/2C_\Sigma$, where the total capacitance is now given by $C_\Sigma = C_J + C_g + C_B$, and turns E_J into the dominant energy scale. Koch et al. have shown that the charge dispersion reduces exponentially with E_J/E_C , so the higher this ratio, the less sensitive the CPB is to charge noise. They have called the CPB that operates in the regime where $E_J \gg E_C$, the *transmon*. If we look at fig. 2.4, we see that the transmon is essentially insensitive to gate charge noise and basically every n_g can be considered a sweet spot.

Anharmonicity

As discussed in the introduction of this thesis, we require the transmon qubit to be sufficiently anharmonic in order to control individual transitions. A harmonic oscillator has all its energy levels equidistantly spaced and is therefore not suited as a qubit. That is because if we apply a pulse (with an undefined number of photons) at its first transition frequency, we do not only excite it to its first excited state, but probably also to higher excited states (see fig. 2.5). Thus, if we denote the qubit ground state by $|g\rangle$, the first excited state by $|e\rangle$, and the second excited state by $|f\rangle$, we require that transition frequency ω_{ge} from $|g\rangle$ to $|e\rangle$ is sufficiently detuned from the transition frequency ω_{ef} from $|e\rangle$ to $|f\rangle$. We define the anharmonicity to be $\zeta_q = \omega_{ge} - \omega_{ef}$.

There are two effects at the origin of the anharmonicity of a CPB [33]. The first is that the quantum fluctuations become larger for higher excitations. The zero-point fluctuations of the phase are given by

$$\phi_{ZPF} = \sqrt{\langle 0 | \hat{\phi}^2 | 0 \rangle} = \sqrt{\frac{\hbar L}{2C}}, \quad (2.11)$$

where the flux ladder operator is given by $\hat{\phi} = \phi_{ZPF}(\hat{b} + \hat{b}^\dagger)$. Here, \hat{b} and \hat{b}^\dagger are the ladder (annihilation and creation, respectively) operators of the qubit excitations. In the extend of eq. (2.11), we find for higher excitations that

$$\sqrt{\langle n | \hat{\phi}^2 | n \rangle} = \phi_{ZPF} \sqrt{2n + 1}. \quad (2.12)$$

The second effect contributing to the anharmonicity is the non-linear dependence on the phase φ due to the cosine in eq. (2.7). Together, these effects result in non-degenerate transition frequencies between higher excited states.

The CPB regime manifests itself with large anharmonicity, but is, as discussed, sensitive to gate charge fluctuations. On the other hand, the transmon is not sensitive to gate charge fluctuations, but the anharmonicity decreases when we increase the ratio E_J/E_C . Fortunately, while the sensitivity to charge noise reduces exponentially with E_J/E_C , the anharmonicity only decreases algebraically with a slow power law. So within the transmon regime, the charge dispersion is greatly reduced while only a small amount of anharmonicity is sacrificed [17].

Returning to the quantum rotor analogy, large E_J/E_C corresponds to a strong gravitational pull, so the rotor will typically stay near its point of lowest potential energy, equal to $\varphi = 0$. For these small angles, the anharmonicity will only be a small perturbation on the harmonic behaviour [17, 21, 33, 34] and we can capture

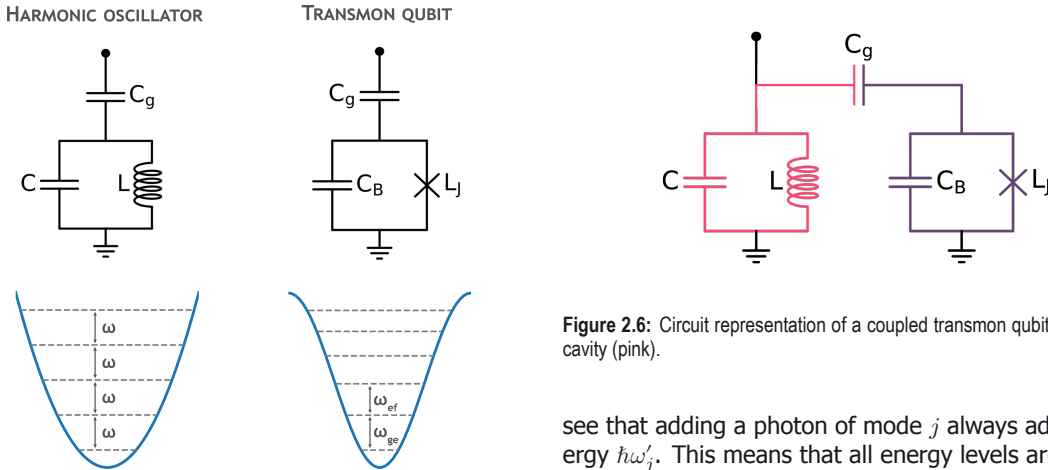


Figure 2.5: Comparison of the energy level spacing of a harmonic oscillator and transmon qubit. The quadratic potential of the harmonic oscillator gives rise to equidistant energy levels, all separated by the same amount of energy, which makes it unsuitable as a qubit. In the cosine potential of the transmon qubit, the transition energies between different subsequent energy levels vary. This yields control over the individual transitions between transmon states.

the leading anharmonicity by truncating the Taylor expansion of $-E_J \cos \hat{\varphi}$ after fourth order.

$$\hat{\mathcal{H}}_q = 4E_C(\hat{n} - n_g)^2 + \frac{1}{2}E_J\hat{\varphi}_J^2 - \frac{1}{24}E_J\hat{\varphi}_J^4 \quad (2.13)$$

This shows that the transmon is well-described by a *Duffing oscillator*.

2.1.4 Coupling to a cavity

To mimic the atomic beam experiment on our chip, we need in addition to the artificial atom a cavity. We choose this to be a superconducting coplanar waveguide (CPW) resonator, which is a quasi-one-dimensional transmission line, consisting of a narrow center conductor and two nearby parallel ground planes along the conductor at constant distance. It has (infinitely) many standing wave resonances, which all depend on the length of the transmission line. Each standing wave mode j is well-described by a simple parallel LC -resonator, which all connected in series construct the CPW resonator. This is described by the Hamiltonian

$$\hat{\mathcal{H}}_{HO} = \sum_j \hbar\omega'_j \left(\hat{a}_j^\dagger \hat{a}_j + \frac{1}{2} \right), \quad (2.14)$$

where $\hat{a}_j^{(\dagger)}$ is the annihilation (creation) operator of a photon of mode j with frequency ω'_j . These operators satisfy the commutation relation $[\hat{a}_j, \hat{a}_{j'}^\dagger] = \delta_{j,j'} [8]$.² We

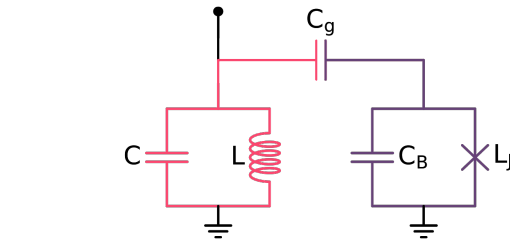


Figure 2.6: Circuit representation of a coupled transmon qubit (purple) and cavity (pink).

see that adding a photon of mode j always adds an energy $\hbar\omega'_j$. This means that all energy levels are equidistantly spaced, which makes the CPW resonator a harmonic oscillator. If we stay near the resonance of a single cavity mode with frequency ω'_c , all the other modes may be neglected and the sum over j in eq. (2.14) can be dropped [30]. Adding eq. (2.14) to the transmon Hamiltonian in eq. (2.13) yields

$$\begin{aligned} \hat{\mathcal{H}} = & 4E_C(\hat{n} - n_g)^2 + \frac{1}{2}E_J\hat{\varphi}_J^2 - \frac{1}{24}E_J\hat{\varphi}_J^4 \\ & + \hbar\omega'_c \left(\hat{a}^\dagger \hat{a} + \frac{1}{2} \right). \end{aligned} \quad (2.15)$$

For the analysis of the system dynamics, a constant energy offset corresponds to a global phase shift of the system and thus plays no role. Consequently, a redefinition of zero energy allows us to ignore the constant $\frac{1}{2}\hbar\omega'_c$.

How can we now create coupling between the qubit and the CPW resonator? At this point we have only considered two separated electronic circuit elements. In fact, the coupling is hidden in the gate charge n_g . If we fabricate the CPW resonator (which we'll just refer to as *the cavity* from now on, hence the subscript c in eq. (2.15)) with an open end, the open boundary condition of its field requires zero current at that end but maximum voltage. If we now locate the qubit in this region, the cavity field will create a voltage difference across the two islands [9, 17, 30]. From this effect follows the coupling between the qubit and the cavity.

Consequently, n_g is now not only the effective gate charge offset induced by the environment, but also that induced by the number of photons inside the cavity. It can be decomposed into a constant (DC) part and a fluctuating (AC) part. As we have seen in the previous section, the transmon qubit is typically insensitive to DC noise. The AC response arises from the qubit coupling to fluctuations in n_g that oscillate at the qubit's resonance frequency. The response increases with a

²The Kronecker delta $\delta_{j,j'}$ equals 1 when $j = j'$, and 0 otherwise.

power law according to $(E_J/E_C)^{1/4}$ [17]. This effect is where the coupling between the qubit and the cavity comes from.

The fluctuating part of n_g can be written in the photon ladder operators such that

$$n_g = n_{dc} + n_{ac}(\hat{a} + \hat{a}^\dagger), \quad (2.16)$$

where n_{ac} is the rms number of vacuum induced Cooper pairs, given by $2eV_{\text{rms}}^0(C_g/C_\Sigma)$. After neglecting the DC component, the charging term of eq. (2.15) can be written as

$$4E_C(\hat{n} - n_g)^2 = 4E_C(\hat{n} - n_{ac}(\hat{a} + \hat{a}^\dagger))^2. \quad (2.17)$$

The term quadratic in n_{ac} contains photon conserving terms and two terms which either create or annihilate two photons. The non-conserving terms are rapidly rotating in the interaction picture. As a consequence, the amplitudes of these transitions are small and we can neglect these terms. This approximation is also known as the rotating wave approximation (RWA) [35].

$$4E_C n_{ac}^2 (\hat{a} + \hat{a}^\dagger)^2 \approx 8E_C n_{ac}^2 \hat{a}^\dagger \hat{a} \quad (2.18)$$

We see that we can combine this term with $\hbar\omega_c' \hat{a}^\dagger \hat{a}$ from eq. (2.15) and define a new cavity frequency as $\omega_c = \omega_c' + 8E_C n_{ac}^2 / \hbar$. Note that in cavity QED we can measure the cavity frequency when it is empty from real atoms, and that we can measure the atoms outside the cavity. However, in circuit QED, because the transmon and the cavity are fixed on the chip and always coupled, it is not really possible to speak of ω_c as a pure cavity parameter, nor of E_C as purely a transmon parameter [34]. Both the qubit and cavity are affected by the other.

As a last step towards an explicit expression of the coupling, we define the Cooper pair number operator as

$$\hat{n} = -\frac{i}{2} \left(\frac{E_J}{2E_C} \right)^{1/4} (\hat{b} - \hat{b}^\dagger) \quad (2.19)$$

[36]. After substitution of this expression into the term linear in n_{ac} , the coupling between the qubit and the cavity is determined by the cross products between the qubit's and cavity's ladder operators:

$$\hat{\mathcal{H}}_g = i\hbar g(\hat{b} - \hat{b}^\dagger)(\hat{a} + \hat{a}^\dagger), \quad (2.20)$$

with the coupling strength parameter (or *vacuum Rabi coupling*) g defined as $\hbar g = 4E_C n_{ac} \left(\frac{E_J}{2E_C} \right)^{1/4}$. The interaction (coupling) Hamiltonian $\hat{\mathcal{H}}_g$ describes the coherent exchange of energy between the qubit and the quantized electromagnetic field inside the cavity. This exchange is particularly observable when the coupling g is much larger than the decoherence rates of the qubit

and cavity [3].³ Section 2.2 will extensively elaborate on the consequences of this coupling to the system.

The total Hamiltonian is now described by the sum of the energy associated with the qubit, the cavity, and with the interaction.

$$\begin{aligned} \hat{\mathcal{H}} = & \underbrace{4E_C \hat{n}^2 + \frac{1}{2} E_J \hat{\varphi}^2}_{\hat{\mathcal{H}}_q} - \frac{1}{24} E_J \hat{\varphi}^4 \\ & + \underbrace{\hbar\omega_c \hat{a}^\dagger \hat{a}}_{\hat{\mathcal{H}}_c} + \underbrace{i\hbar g(\hat{b} - \hat{b}^\dagger)(\hat{a} + \hat{a}^\dagger)}_{\hat{\mathcal{H}}_g} \end{aligned} \quad (2.21)$$

In the transmon's charge basis, this equation reads

$$\begin{aligned} \hat{\mathcal{H}} = & \hbar \sum_j \omega_j |j\rangle \langle j| + \hbar\omega_c \hat{a}^\dagger \hat{a} \\ & + \hbar \sum_{i,j} g_{i,j} |i\rangle \langle j| (\hat{a} + \hat{a}^\dagger), \end{aligned} \quad (2.22)$$

which is known as the *generalized Rabi Hamiltonian* [34] (this name will become clear from section section 2.1.5). The dipole coupling energies $\hbar g_{i,j}$ vary for different pairs of transmon states and are given by $n_{ac} \langle i | \hat{n} | j \rangle$ [17].

2.1.5 Three representations of the transmon qubit

When coupled to a cavity, we can approximate the transmon qubit by three different types of oscillators —the Duffing oscillator, the Kerr oscillator, and the two-level system. The Duffing oscillator is a simplification of the shunted Cooper pair box, the Kerr is a simplification of the Duffing oscillator, and the two-level system is in its turn a simplification of the Kerr oscillator. Within this thesis, the focus is on the Duffing and Kerr oscillator. The two-level system will be especially useful for providing insight in the consequences of the coupling between the qubit and cavity (section 2.2).

The Duffing oscillator

In section 2.1.3, we have argued that it is valid for a transmon to expand the cosine in the CPB Hamiltonian to fourth order due to the small phase deviations from $\varphi = 0$. The resulting Hamiltonian form of the transmon in eq. (2.13) describes a Duffing oscillator. We will now work out the Hamiltonian of eq. (2.21) to obtain a more useful expression for the system's total energy.

The number operator \hat{n} and phase operator $\hat{\varphi}$ are related through the canonical commutation relations

³Decoherence will be explained in section 2.4.

$[\hat{n}, \hat{\varphi}] = i$ and $\hat{n} = i \frac{\partial}{\partial \hat{\varphi}}$. With \hat{n} defined as in eq. (2.19), we define $\hat{\varphi}$ as

$$\hat{\varphi} = \left(\frac{E_J}{2E_C} \right)^{-1/4} (\hat{b} + \hat{b}^\dagger). \quad (2.23)$$

This gives us the qubit Hamiltonian as

$$\begin{aligned} \hat{\mathcal{H}}_q = & \sqrt{8E_J E_C} (\hat{b} - \hat{b}^\dagger)^2 + \sqrt{\frac{1}{2} E_J E_C} (\hat{b} + \hat{b}^\dagger)^2 \\ & - \frac{E_C}{12} (\hat{b} + \hat{b}^\dagger)^4. \end{aligned} \quad (2.24)$$

In the first line we recognize a harmonic oscillator with bare frequency $\omega'_q = \sqrt{8E_J E_C}/\hbar$. The last term, containing the fourth power of the qubit's ladder operators, defines the *quantum Duffing oscillator*. It contains photon conserving elements and elements that create or annihilate two or four photons. Important to note is that the first transition frequency of this Duffing oscillator is not equal to ω'_q . It deviates from ω'_q by roughly E_C due to the fourth-power term. For example, if we choose $\omega'_q/2\pi = 6.500$ GHz and $E_C/\hbar = 0.200$ GHz, then by diagonalizing $\hat{\mathcal{H}}_q$ we find the qubit's first transition to correspond to a frequency of 6.286 GHz. So, similarly to ω'_c and E_C , ω'_q is rather a convenient parameter of the system to write the total Hamiltonian as

$$\begin{aligned} \hat{\mathcal{H}}_D = & \hbar\omega'_q \hat{b}^\dagger \hat{b} - \frac{E_C}{12} (\hat{b} + \hat{b}^\dagger)^4 + \hbar\omega_c \hat{a}^\dagger \hat{a} \\ & + \hbar g (\hat{b} + \hat{b}^\dagger) (\hat{a} + \hat{a}^\dagger). \end{aligned} \quad (2.25)$$

Note that in $\hat{\mathcal{H}}_q$ we have switched to the convention without imaginary prefactor.

The Kerr oscillator

A common approximation is to neglect the qubit's self-interaction, expressed by the non-conserving, off-diagonal elements in the second term in eq. (2.25). These self-interacting terms are much more rapidly rotating in the interaction picture than the diagonal elements. If we apply a rotating wave approximation on the self-interaction we can express the Duffing oscillator by a *Kerr oscillator*:

$$-\frac{E_C}{12} (\hat{b} + \hat{b}^\dagger)^4 \approx -\frac{E_C}{2} \left(\hat{b}^\dagger \hat{b}^\dagger \hat{b} \hat{b} + 2\hat{b}^\dagger \hat{b} + \frac{1}{2} \right). \quad (2.26)$$

The first term on the right-hand side $-\frac{1}{2} E_C \hat{b}^\dagger \hat{b}^\dagger \hat{b} \hat{b}$ is called the Kerr non-linearity. If we discard the constant $-E_C/4$, which corresponds to an irrelevant global phase shift, and we define the new qubit frequency as $\omega_q = \omega'_q - E_C/\hbar$, we arrive at the total Hamiltonian in the Kerr approximation:

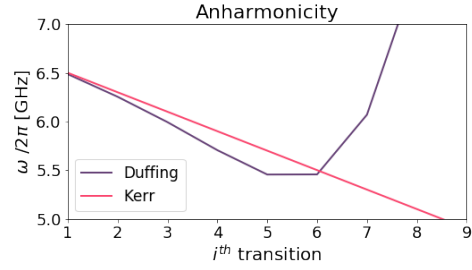


Figure 2.7: Anharmonicity of the Duffing an Kerr oscillator. The i^{th} transition frequency is numerically calculated from diagonalization of a 10-level qubit.

$$\begin{aligned} \hat{\mathcal{H}}_K = & \hbar\omega_q \hat{b}^\dagger \hat{b} - \frac{E_C}{2} \hat{b}^\dagger \hat{b}^\dagger \hat{b} \hat{b} + \hbar\omega_c \hat{a}^\dagger \hat{a} \\ & + \hbar g (\hat{b} + \hat{b}^\dagger) (\hat{a} + \hat{a}^\dagger). \end{aligned} \quad (2.27)$$

An important qualitative difference between the Duffing an Kerr oscillator is that the latter has a constant anharmonicity of E_C between two adjacent transitions, whereas the higher anharmonicities of a Duffing oscillator do not scale linearly (see fig. 2.7).

The two-level system

We could simplify the model even more by restricting ourselves to only the first two qubit levels in eq. (2.22), which we denote by $|g\rangle$ and $|e\rangle$. This *two-level system* (TLS) is especially useful for computational means where the two levels form a bit [20]. Where a classical bit can unambiguously be either 0 or 1, a qubit living in a two-dimensional Hilbert space can be in any superposition state between the states $|g\rangle$ and $|e\rangle$:

$$|\psi\rangle = \alpha |g\rangle + \beta |e\rangle, \quad (2.28)$$

where the weights α and β are complex scalars. Since the probabilities of finding the qubit in its ground or excited state are $P_g = |\alpha|^2$ and $P_e = |\beta|^2$, respectively, the weights are normalized as $|\alpha|^2 + |\beta|^2 = 1$.

One has to take care with the approximation by a TLS, for the validity of the approximation depends on the transition amplitude to higher states being negligibly small. This is especially the case when the anharmonicity is sufficiently large and $g \ll |\omega_q - \omega_c| \ll E_C$. The validity of these interparameter relations will become clear in the next section, where we discuss the consequences of the coupling between the qubit and cavity.

Although the TLS plays only a limited role in this thesis, we will discuss it here nonetheless, since it has convenient analytical properties that will help us

understand the consequences of the coupling between the qubit and cavity, discussed in section 2.2.

Within the two-level approximation, the coupled system can be described by the *quantum Rabi model* (QRM), which is characterized by the *Rabi Hamiltonian*

$$\hat{\mathcal{H}}_R = \frac{\hbar}{2}\omega_q\hat{\sigma}_z - \hbar\omega_c\hat{a}^\dagger\hat{a} + \hbar g\hat{\sigma}_x(\hat{a} + \hat{a}^\dagger), \quad (2.29)$$

where $\hat{\sigma}_i$ represents the i -component Pauli spin- $\frac{1}{2}$ matrix. Within the QRM, it is common to apply a RWA on the interaction Hamiltonian and ignore simultaneous (de)excitations of the qubit and cavity, since the terms exchanging energy between the qubit and cavity ($\hbar g(a\hat{\sigma}_+ + \hat{a}^\dagger\hat{\sigma}_-)$) nearly conserve all energy and the counter-rotating terms are rapidly rotating in the interaction picture. Neglecting the counter-rotating terms is typically done when the energy required to excite both the qubit and cavity is much larger than the coupling strength and energy difference between them: $\omega_q + \omega_c \gg g, |\omega_q - \omega_c|$ [30]. At this point, we have arrived at the well-known *Jaynes-Cummings Hamiltonian*

$$\hat{\mathcal{H}}_{JC} = \frac{\hbar}{2}\omega_q\hat{\sigma}_z - \hbar\omega_c\hat{a}^\dagger\hat{a} + \hbar g(\hat{a}\hat{\sigma}_+ + \hat{a}^\dagger\hat{\sigma}_-). \quad (2.30)$$

The big advantage of this Hamiltonian form is that it is analytically solvable [30].

2.2 Consequences of the qubit-cavity coupling

We have seen that coupling the cavity to the qubit allows for interaction between the two. There are, however, numerous non-trivial effects arising from this interaction. For the sake of illustration, we will show these effects according to the simplest model —the Jaynes-Cummings model of eq. (2.30), since in this form, the model is analytically solvable.

In cavity QED, when we locate an atom inside a cavity, the atom and cavity become entangled. Similarly, in circuit QED, if we couple the transmon qubit to the CPW resonator, they become entangled [3]. The qubit's bare ground and excited states ($|g\rangle, |e\rangle$), and the cavity photon number states $|n\rangle$ are then no longer the system's eigenstates. Instead, we have to consider the 'dressed' eigenstates with shifted eigenenergies. There are primarily two regimes to consider —the resonant regime and the dispersive regime.

2.2.1 Resonant coupling

In the resonant regime our qubit and cavity are mutually at resonance, $\omega_q \simeq \omega_c$. Differently, we can quantify the

allowed detuning Δ_{qc} between the qubit and cavity as $|\Delta_{qc}| \equiv |\omega_q - \omega_c| \ll g$. The bare (uncoupled) energy levels are degenerate and the wavelength of the photon emitted by the qubit matches the length of the cavity. However, when we couple the qubit and cavity, the new eigenstates of the system are fully hybridized superpositions of the qubit and cavity states:

$$\frac{1}{\sqrt{2}}(|g, n\rangle \pm |e, n-1\rangle). \quad (2.31)$$

These states are split by an energy difference of $2\hbar g\sqrt{n+1}$, called the vacuum Rabi splitting. The degenerate levels $|g, 1\rangle$ and $|e, 0\rangle$, for example, mix and split up with an energy difference $2g$ [30].

The entangled, dressed eigenstates of the system have the remarkable consequence that the qubit and cavity will automatically interchange energy. An excited qubit, for example, is not an eigenstate of the system. Specifically, if we place an initially excited atom inside an initially empty cavity, the coupled system will be in an equal superposition of the states $|e, 0\rangle$ and $|g, 1\rangle$ [21]. The probability to measure the atom in its excited state (and consequently measure zero photons in the cavity) will oscillate sinusoidally with a rate $2g$. This rate is called the *vacuum Rabi frequency*.⁴ The same effect holds for circuit QED. If more photons are involved in the process, the Rabi frequency scales as $2g\sqrt{n+1}$ [31]. In the picture of cavity QED, it is clear that the oscillation rate increases with the photon number n , since there are more photons present inside the cavity with which the atom can interact. Note that since we consider a two-level atom, it can only absorb one photon at a time. In the case of a multi-level qubit, with first-transition frequency ω_{ge} equal to the cavity frequency, the anharmonicity (if sufficiently large) prevents the qubit from being excited to its $|f\rangle$ state.

2.2.2 Dispersive coupling

In the dispersive coupling regime, the detuning between the qubit and the cavity frequency is much larger than their coupling strength: $|\Delta_{qc}| \gg g$. In this regime, we would observe no oscillatory exchange of energy, because the qubit excitation energy does not match the cavity photon wavelength. Instead, there are virtual photons that mediate the dispersive interaction and induce shifts to the system's eigenstates [30]. The interplay between the qubit and cavity becomes apparent

⁴It is called 'vacuum' Rabi frequency because the oscillation would also be observed in the case that both the atom (qubit) and cavity are initially in their ground state. This is because vacuum fluctuations in the cavity can trigger the excitation of the atom (qubit) [30].

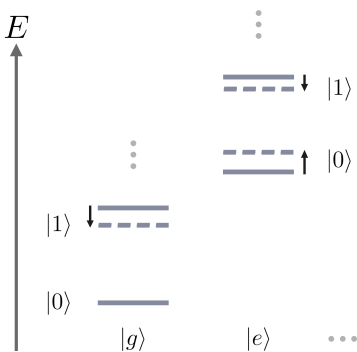


Figure 2.8: Schematic energy level diagram of a dispersively coupled qubit and cavity. Solid lines are the bare energy levels of the uncoupled system. Striped lines are their dressed equivalents (shifts are drawn out of proportion).

after a unitary⁵ Schrieffer-Wolff transformation \hat{U} :

$$\hat{U} = \exp \left[\frac{g}{\Delta_{qc}} (\hat{\sigma}_+ \hat{a} + \hat{\sigma}_- \hat{a}^\dagger) \right] \quad (2.32)$$

[20, 37]. To second order in g , the Jaynes-Cummings Hamiltonian transformed by \hat{U} becomes

$$\hat{\mathcal{H}}'_{JC} = \hat{U} \hat{\mathcal{H}}_{JC} \hat{U}^\dagger + i(\partial_t \hat{U}) \hat{U}^\dagger \quad (2.33)$$

$$= \hbar \omega_c \hat{a}^\dagger \hat{a} + \frac{\hbar}{2} \left(\omega_q + 2 \frac{g^2}{\Delta_{qc}} \hat{a}^\dagger \hat{a} \right) \hat{\sigma}_z \quad (2.34)$$

$$= \hbar \left(\omega_c + \frac{g^2}{\Delta_{qc}} \hat{\sigma}_z \right) \hat{a}^\dagger \hat{a} + \frac{\hbar}{2} \omega_q \hat{\sigma}_z. \quad (2.35)$$

We see that the coupling term from eq. (2.30) is replaced by the state-dependent frequency shift $\chi = g^2/\Delta_{qc}$, also known as the *dynamical* or *AC Stark shift*. Interestingly, it can be interpreted in two different ways [9, 30, 31]. In eq. (2.34), it shows a shift of the qubit frequency depending on the number of photons inside the cavity. Alternatively, it may be seen as a shift of the cavity frequency depending on the qubit state (eq. (2.35)). This phenomenon has lead to a remarkable quantum measurement technique. Firstly, it suggests that we can measure the state of the qubit by measuring the cavity (and vice versa). And secondly, since eq. (2.35) commutes with both the cavity photon number and qubit polarization, it tells us that we can do so without altering the state of the qubit. Such a measurement of the qubit through the cavity is called a quantum non-demolition (QND) measurement. This is what Serge Haroche [1] and Dave Wineland [6] won the Nobel Prize for in 2012, when they independently from

the other developed these techniques with real atoms. The same QND measurements have been demonstrated in circuit QED [38].

How can we now understand this frequency shift physically? We have not changed anything about the geometry of the CPW resonator. It has still the same length and the same open and/or closed ends. The subtlety of this lies in the boundary conditions of the cavity's field. The vicinity of the qubit changes the boundary conditions at the open end of the CPW and with that the cavity's normal modes. It is this effect that shifts the frequency at which we find resonance in the cavity.

2.2.3 Beyond the Jaynes-Cummings model

The analytical calculation of the multi-level transmon's dispersive level shifts is much more tedious. This is partly because the coupling strength varies between different qubit levels. Koch et al. provide perturbative formulas in [17] to calculate the shifted energy levels, but they have appeared not to be sufficiently accurate for the applications within this thesis, where we will require precisions up to 100 kHz or even 10 kHz.

There are three important messages to be given here. The first is that, qualitatively, the dressed energy levels of a dispersively coupled transmon qubit and cavity are shifted with respect to the bare energy levels, whether we consider a Duffing oscillator or Kerr oscillator for the transmon. Secondly, we have to stress that the amount by which and in what direction the different levels shift, depends on the model that we consider. Lastly, because of these dispersive shifts, the QND measurement is not unique to the Jaynes-Cummings model as described earlier in this section, but is as well possible within the Duffing and Kerr approximations.

Quantitatively, the amplitudes of the dispersive shifts are easily calculated by numerical diagonalization of the total model Hamiltonian. This method leads to a straight forward calculation of the dressed qubit and cavity frequencies, $\tilde{\omega}_q$ and $\tilde{\omega}_c$, respectively. These are defined as the single-photon frequencies required to excite the system from the dressed $|g, 0\rangle$ state to $|e, 0\rangle$ or $|g, 1\rangle$.

$$\hbar \tilde{\omega}_q = E_{|e,0\rangle} - E_{|g,0\rangle} \quad (2.36)$$

$$\hbar \tilde{\omega}_c = E_{|g,1\rangle} - E_{|g,0\rangle} \quad (2.37)$$

⁵A unitary transformation is a mathematical transformation to move to a different frame of perspective while preserving the inner product. This means that when $|\psi\rangle$ is an eigenstate of $\hat{\mathcal{H}}$, then the transformed $|\psi'\rangle$ is an eigenstate of the transformed Hamiltonian $\hat{\mathcal{H}}'$.

2.3 Sideband transitions

In the atomic beam experiment, the coupling arises when the atom passes between the cavity mirrors. Outside the cavity, the atom is disentangled from the cavity field. In circuit QED, however, the qubit and the CPW resonator are mounted on the chip substrate and the coupling cannot be turned off. How then can we mimic the atom's passage through the cavity?

In the previous section on the qubit-cavity coupling, we have seen that, in the resonant regime, Rabi oscillations appear. If the qubit and cavity frequency are far detuned from one another, though, that is in the dispersive regime, there is no exchange of energy. Apart from the energy level shifts, it is as if the qubit and cavity don't see each other. Therefore, we can use this regime to mimic the atom not being inside the cavity field. And the coherent interaction between the atom and the cavity when the atom passes between the mirrors? We will realize those Rabi oscillations with so-called *sideband transitions*. This section elaborates on how to realize these coherent interactions between the qubit and the cavity when they are dispersively coupled. From this point, we will leave the two-level system behind and consider only the multi-level Duffing and Kerr oscillators.

In this thesis we will consider two types of sideband transitions [18, 20]. The *red* sideband transitions are between the dressed states $|e, 0\rangle$ and $|g, 1\rangle$. This mimics the situation where an initially excited atom passes through an initially empty cavity, or where an atom in its ground state enters the cavity in which one photon is present. In the Rabi oscillations in circuit QED, the excitation of the qubit is transferred to the cavity as a photon, and subsequently absorbed again by the qubit. The *blue* sideband transitions are simultaneous (de)excitations of both the qubit and the cavity, that is between the dressed states $|e, 1\rangle$ and $|g, 0\rangle$. The names 'red' and 'blue' originate from the fact that the wavelength of a photon involved in a red transition is longer than that of a photon mediating a blue sideband transition. Both transitions are drawn in fig. 2.9.

2.3.1 The sideband drive

To induce these sideband transitions we have to add a coherent⁶ drive to the system [19]. The moment this drive is turned on in our circuit QED experiment rep-

⁶A coherent quantum state is a special superposition of all possible Fock states, which shows the dynamics most resembling the oscillatory behaviour of a classical harmonic oscillator. Explicitly, a coherent state is the eigenstate of the photon annihilation operator: $\hat{a}|\alpha\rangle = \alpha|\alpha\rangle$. Thus, annihilating a photon from a coherent state yields the same state. The probability of finding a specific number of photons is Poissonian distributed with the mean photon number given by $\langle\alpha|\hat{a}^\dagger\hat{a}|\alpha\rangle = |\alpha|^2$. All photons from a coherent state are in phase [31].

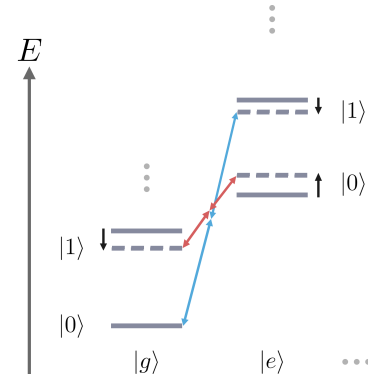


Figure 2.9: Monochromatic two-photon sideband transitions in a schematic energy level diagram of a coupled qubit and cavity. Solid lines are the bare energy levels of the uncoupled system. Striped lines are their dressed equivalents (shifts are drawn out of proportion). The red transitions exchange energy between the qubit and cavity by transitioning between the dressed states $|e, 0\rangle$ and $|g, 1\rangle$. The blue sideband transitions (de)excite the qubit and cavity simultaneously between the states $|e, 1\rangle$ and $|g, 0\rangle$.

resents the atom entering the cavity in the cavity QED experiment. The atom leaving the cavity we mimic by turning off the drive. The drive in circuit QED is an electromagnetic light field, coupled to either the qubit or the cavity. In this thesis, we will consider it only to be coupled directly to the qubit and not to the cavity. Experimentally, it is realized by a drive line (voltage source) to the qubit (see fig. 2.10). We write its Hamiltonian as

$$\hat{\mathcal{H}}_d = 2\epsilon_d \cos(\omega_d t) (\hat{b} + \hat{b}^\dagger), \quad (2.38)$$

where $2\epsilon_d$ is the drive amplitude and ω_d is the drive frequency. The total driven Hamiltonian is then given by $\hat{\mathcal{H}} = \hat{\mathcal{H}}_q + \hat{\mathcal{H}}_c + \hat{\mathcal{H}}_g + \hat{\mathcal{H}}_d$.

Often the drive Hamiltonian $\hat{\mathcal{H}}_d$ is approximated by removing the counter-rotating terms in the interaction picture [20]. If we map $\hat{\mathcal{H}}_d$ to the interaction picture, there are terms of \hat{b} and \hat{b}^\dagger rotating at $\omega_d + \omega_q$ and $\omega_d - \omega_q$, where ω_q is the frequency corresponding to the transition induced by \hat{b} and \hat{b}^\dagger .

$$\begin{aligned} \hat{\mathcal{H}}_{d, I.P.} = & \frac{2\epsilon_d}{2} \left(\hat{b} e^{+i(\omega_d - \omega_q)t} + \hat{b}^\dagger e^{-i(\omega_d - \omega_q)t} \right. \\ & \left. + \hat{b} e^{-i(\omega_d + \omega_q)t} + \hat{b}^\dagger e^{+i(\omega_d + \omega_q)t} \right) \end{aligned} \quad (2.39)$$

If ω_q is such that $\omega_d + \omega_q \gg \omega_d - \omega_q$, the terms with the sum frequency are rotating much faster than the terms with the difference frequency. We call the former the counter-rotating terms and neglecting them corresponds to the rotating wave approximation. After transforming back, we are left with

$$\hat{\mathcal{H}}'_d = \epsilon_d \left(\hat{b} e^{+i\omega_d t} + \hat{b}^\dagger e^{-i\omega_d t} \right). \quad (2.40)$$

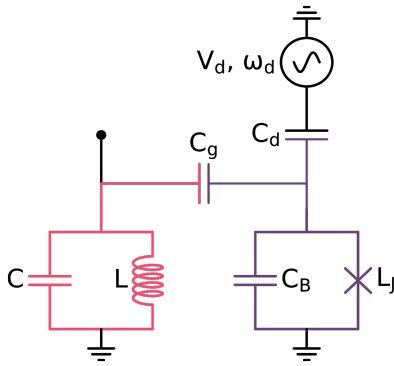


Figure 2.10: Circuit representation of a coupled qubit (purple) and cavity (pink). A voltage source capacitively coupled to the qubit acts as a drive.

We will see the effect of this RWA in chapter 4.

2.3.2 Determining the drive frequency

What drive frequency ω_d is required to induce the sideband transitions? A naive first guess would be that we need the difference frequency $|\Delta_{qc}| = |\omega_q - \omega_c|$ for the red sideband transitions and the sum frequency $\Sigma_{qc} = \omega_q + \omega_c$ for the blue sideband transitions. However, we then forget that in order to have transitions in the first place, we require the qubit and cavity to be coupled, which shifts the energy levels. A second guess would thus be to use the dressed difference frequency $|\tilde{\Delta}_{qc}| = |\tilde{\omega}_q - \tilde{\omega}_c|$ and dressed sum frequency $\tilde{\Sigma}_{qc} = \tilde{\omega}_q + \tilde{\omega}_c$, though parity selection rules forbid single-photon processes for a transmon [19, 39]. As a consequence, we need to consider transitions involving two drive photons. In addition to these effects on the required drive frequency, there is yet a third modification to take into consideration. Driving the qubit will affect the energy levels, which endure an additional shift depending on the drive strength ϵ_d and the drive frequency ω_d . Section 2.3.3 will elaborate on the extend to which the qubit transition frequency is modified. For now, we will denote this driving shift by $\delta\omega_q$.

The relevant two-photon transitions presented in this thesis are realized by a monochromatic (single-tone) drive. This type of drive has a single frequency $\omega_d = (\tilde{\omega}_q + \delta\omega_q \pm \tilde{\omega}_c)/2$, so we need two photons from this drive in order to induce a red (difference frequency) or blue (sum frequency) transition [19]. Another possibility would be to use two different drive tones with different strengths. Such a bichromatic drive is explained and demonstrated in appendix G.

2.3.3 Impact of the drive on the qubit resonance

This section discusses the shift and modulation of the first qubit transition frequency as a consequence of the applied drive field.⁷ We make the assumption that the drive shifts only the qubit levels and that the amount by which the levels shift is unrelated to the dispersive coupling shifts ($\chi \ll g$). The total shift of the levels is then assumed to be the sum of the shift by driving and the shift by coupling. Likely, both effects are in reality not fully uncorrelated, but because the dispersive coupling shift is very small compared to the qubit frequency ($|\omega_q - \tilde{\omega}_q| \ll \omega_q$), the error of this approximation is assumed to be small as well.

To calculate the qubit's frequency shift due to the drive, we apply a mathematical transformations that moves us to the displaced frame of the drive. This is done through the unitary Schrieffer-Wolff transformation

$$\hat{U} = e^{-\xi(t)\hat{b}^\dagger + \xi^*(t)\hat{b}} \quad (2.41)$$

[40], where

$$\xi(t) = \frac{\epsilon_d}{\Delta_{dq}} e^{-i\omega_d t} - \frac{\epsilon_d}{\Sigma_{dq}} e^{+i\omega_d t}. \quad (2.42)$$

Here, $\Delta_{dq} = \omega_d - \omega_q$ and $\Sigma_{dq} = \omega_d + \omega_q$. Appendix D discusses the origin of this transformation more extensively. \hat{U} transfers all $\hat{b} \rightarrow \hat{b} + \xi(t)$ and $\hat{b}^\dagger \rightarrow \hat{b}^\dagger + \xi^*(t)$. Writing out the transformed Duffing Hamiltonian $\hat{\mathcal{H}}'_D$ (see appendix D) yields the finding that the drive has shifted the qubit frequency by a constant $\delta\omega_q$ and modulated by an oscillating $\eta(t)$.

$$\begin{aligned} \delta\omega_q + \eta(t) = & -2\epsilon_d^2 E_C \left(\frac{1}{\Delta_{dq}^2} + \frac{1}{\Sigma_{dq}^2} - \frac{2}{\Delta_{dq}\Sigma_{dq}} \right) \\ & \times (1 + \cos 2\omega_d t). \end{aligned} \quad (2.43)$$

The constant shift $\delta\omega_q$ (which we will call the *driven qubit shift*) shows us that the qubit's transition frequency is modulated as a function of the drive strength ϵ_d and drive frequency ω_d . $\eta(t)$ oscillates at twice the drive frequency and will be responsible for the so-called micromotion discussed in chapter 3. In appendix D, we show that a similar modulation of the qubit frequency happens for the Kerr oscillator, but where $\delta\omega_q$ and $\eta(t)$ have different amplitudes.

2.3.4 Sideband coupling

To obtain the effective coupling in the atomic beam experiment, we are interested in the rate at which the

⁷Parts of this section will be submitted for publication.

sideband transitions will occur. We can analytically calculate this rate for the Duffing oscillator, thanks to theory Byoung-moo Ann developed during this thesis project.⁸ Appendix C discusses the derivation into detail. In this section, we will only briefly outline the most important steps.

The first step is going to the normal mode basis of the undriven Duffing Hamiltonian $\hat{\mathcal{H}}_D$ where the explicit coupling term $\hat{\mathcal{H}}_g$ is eliminated. In this basis, the new qubit-like operator $\hat{\beta}$ and cavity-like operator $\hat{\alpha}$ are linear combinations of \hat{b} and \hat{a} . The dressed states $|e, 0\rangle$ and $|g, 1\rangle$ are eigenstates of the new normal mode Hamiltonian, with $\tilde{\omega}_q$ and $\tilde{\omega}_c$ as corresponding eigenvalues. This Hamiltonian is given by

$$\begin{aligned}\hat{\mathcal{H}}'_D = & \tilde{\omega}_q \hat{\beta}^\dagger \hat{\beta} + \tilde{\omega}_c \hat{\alpha}^\dagger \hat{\alpha} \\ & - \frac{1}{12} [\chi_q^{1/4} (\hat{\beta} + \hat{\beta}^\dagger) + \chi_c^{1/4} (\hat{\alpha} + \hat{\alpha}^\dagger)]^4\end{aligned}\quad (2.44)$$

[41], where χ_q and χ_c are the qubit's and cavity's self-Kerr, respectively. Subsequently, we add the drive to the system and go to the displaced frame of the drive through the same Schrieffer-Wolff transformation as of eq. (2.41), but now considering the normal mode operators $\hat{\beta}$ and $\hat{\beta}^\dagger$ instead, and the dressed qubit frequency $\tilde{\omega}_q$ in $\xi(t)$. In the normal mode basis, the interactions are mediated by the sideband drive, so the sideband coupling is captured by the cross-terms of the qubit and cavity normal mode operators that depend on $\xi(t)$. Within the Duffing approximation, the sideband transition rate to first order is then given by

$$\Omega_{sb} = 2\chi_q^{3/4} \chi_c^{1/4} \epsilon_d^2 \left(\frac{1}{\tilde{\Delta}_{dq}^2} + \frac{1}{\tilde{\Sigma}_{dq}^2} - \frac{2}{\tilde{\Delta}_{dq} \tilde{\Sigma}_{dq}} \right), \quad (2.45)$$

with $\tilde{\Delta}_{dq} = \omega_d - \tilde{\omega}_q$ and $\tilde{\Sigma}_{dq} = \omega_d + \tilde{\omega}_q$. The qubit's self-Kerr χ_q is within the dispersive regime well-approximated by $\chi_q \approx E_C$ [41]. The cavity's self-Kerr χ_c is related to χ_q through the cross-Kerr as $\chi_{qc} = \sqrt{\chi_q \chi_c}$. The cross-Kerr can be calculated by diagonalization of the undriven Hamiltonian $\hat{\mathcal{H}}_D$ as $2\chi_{qc} = (E_{|e,0\rangle} - E_{|g,1\rangle}) - (E_{|e,1\rangle} - E_{|g,2\rangle})$.

From eq. (2.45) we see that the transition rate scales quadratically with the drive strength and linear with the drive power. From this formula we can also expect that the blue transitions will be characterized by a faster rate than the red (for equal ϵ_d). This is since $\tilde{\Delta}_{dq}$ will be much smaller than in the red case, which has a large impact on Ω_{sb} .

⁸Therefore it has not yet been published. This part will be submitted for publication.

2.4 Interaction with the environment

Ideally, we would like to have a system that is completely stable, of which the transition frequencies do not change over time, and that is not affected by the environment. Yet, it should have an open port to the outside world through which we can measure and control its state. Reality is that no system is ever entirely isolated from the outside world. Moreover, if our system were completely isolated, it would also be decoupled from our measurement instruments. There would be no way to gain information about it. Decoupling from noise sources and strong coupling to our measurement instruments and control electronics is one of the main experimental challenges in qubit and setup design [11]. The interaction with the environment, which can be modelled as a bath with many degrees of freedom, inherently leads to noise in our measurements in an unpredictable and uncontrolled way [4]. The loss of information into the environment due to the coupling to fluctuations in it is called decoherence. In mathematical terms, the Hamiltonian dynamics preserves the purity of the wavefunction, whereas the coupling to the environment causes the density matrix ρ to be mixed, leading to fundamental uncertainty about the quantum state our system is in.⁹ There are two contributions with characteristic time scales that lead to the loss of coherence—depolarization and dephasing.

2.4.1 Depolarization

Depolarization is the undesired and uncontrolled change of the qubit or cavity state [4]. The name originates from the two-level atom where its $|g\rangle$ and $|e\rangle$ states are represented by the poles on the so-called Bloch sphere. When the atom is initially in its excited state, it can spontaneously loose its energy by emitting a photon and falling back to its ground state. On the other hand, if noise sources from the environment are of sufficiently high frequency near ω_{ge} , the atom can absorb a photon of this frequency and become excited. Obviously, these processes are not unique for a two-level atom, but hold as well for the different possible transitions of a multi-level transmon qubit and a harmonic oscillator. In the case of a CPW resonator, for example, the transmission line will not be perfectly transparent and photons may escape from the ends [42].

⁹Note that a superposition of, for example, $|g\rangle$ and $|e\rangle$ states is not a mixed state but in fact a pure state. Though the outcome of a measurement of $\hat{b}^\dagger \hat{b}$ is random, we know for certain that the system is in this superposition state. This state $|\psi\rangle$ can then be fully described by a column vector. A mixed state, on the other hand, is a statistical ensemble of possible states, which is not fully described by a column vector but by a density matrix ρ . Because of the uncontrollable interactions with the environment, there is fundamental uncertainty about what quantum state the system is in.

The total depolarization rate is given by the sum of the absorption rate and the emission rate [20]:

$$\Gamma_1 = \Gamma_{\uparrow} + \Gamma_{\downarrow}. \quad (2.46)$$

In the quantum limit, the negative and positive frequency contribution of the spectral noise density is asymmetric. Therefore, the relaxation rate Γ_{\downarrow} and the absorption rate Γ_{\uparrow} can be different. To control and measure the system's state, the states are required to be sufficiently long-lived compared to the manipulation times. So we have to enhance the depolarization time $T_1 = 2\pi/\Gamma_1$. To suppress the absorption by the qubit and cavity, we cool down the system to very low cryogenic temperatures (10 mK in our case), where $k_b T \ll \hbar\omega$. With the thermal noise exponentially suppressed, $\Gamma_{\uparrow} \approx 0$ and $\Gamma_1 \approx \Gamma_{\downarrow}$. That is why the depolarization rate is commonly referred to as the energy (or longitudinal) relaxation rate. We use the notation Γ_1 for the general case and save γ_1 and κ_1 for, respectively, the qubit and the cavity.

Systems that show multiple Rabi cycles before the energy is lost to the environment are said to operate in the strong coupling regime, that is $g \gg \Gamma_1$. The coherent interaction between the qubit and the cavity is the dominant form of interaction. In the opposite regime, where $g \ll \Gamma_1$, the interaction is basically incoherent and dominated by the damping rates γ_1 and κ_1 . For many applications, coherent interaction is required and we require operating in the strong coupling regime. Circuit QED provides the easy part of strong qubit-cavity coupling for the Rabi cycles, manipulation and readout. The more difficult part is the close to perfectly shielding of the chip from interactions with the environment so that dissipative loss is suppressed and quantum vacuum fluctuations do not trigger spontaneous emission [30].

2.4.2 Dephasing

Dephasing is the randomization of the phase difference between two eigenstates [43]. The dephasing rate Γ_2 is a combination of the depolarization rate Γ_1 and the pure dephasing rate Γ_{φ} :

$$\Gamma_2 = \frac{\Gamma_1}{2} + \Gamma_{\varphi}. \quad (2.47)$$

Depolarization is included because the coherent superposition of two eigenstates, say $|g\rangle$ and $|e\rangle$, is destroyed if the qubit makes a transition between them. The pure dephasing arises from adiabatic fluctuations in the energy spacing between two eigenstates. The latter is non-dissipative, so it does not involve any energy exchange with the environment. Dephasing is what gives the qubit and cavity spectrum their finite linewidth, which we define as the spectrum's

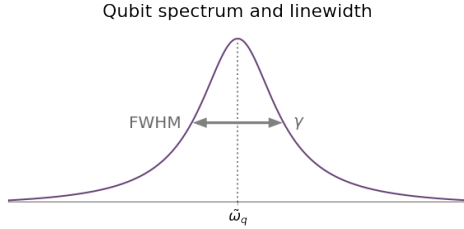


Figure 2.11: Lorentzian shape of the qubit spectrum. The linewidth γ arises from the dephasing rate and is defined by the full-width-half-maximum (FWHM) of the spectrum.

full-width-half-maximum (FWHM, see fig. 2.11).

Here, we should distinguish Γ_2 from Γ_2^* . Where the former describes an intrinsic timescale for the decoherence, the latter is a measure for an ensemble of repeatedly performed measurements. Fluctuations on the timescale of at least one measurement then result in different conditions for different measurements, which reduces the actual observed decoherence time from $T_2 = 2\pi/\Gamma_2$ to $T_2^* = 2\pi/\Gamma_2^*$ [43]. T_2^* is associated with both homogeneous and inhomogeneous broadening of the spectrum and can be measured by a Ramsey experiment [44]. T_2 can be determined by spin-echo measurements [45], which eliminate the inhomogeneous broadening effects [31].

In the discussion of the transmon regime in section 2.1.3, we have seen that the transmon qubit is practically insensitive to DC and low-frequency noise. This minimizes the pure dephasing for the transmon qubit and we can approximate its dephasing rate by $\gamma_2 \simeq \gamma_1/2$.

2.4.3 Time evolution of an open quantum system

The time evolution of the state of an open quantum system interacting with its environment can be completely described by the Lindblad master equation (LME). The dynamics are captured by the density matrix $\hat{\rho}$, Hamiltonian $\hat{\mathcal{H}}$ and collapse operators \hat{C}_n as

$$\begin{aligned} \frac{d\hat{\rho}}{dt} &= \underbrace{-\frac{i}{\hbar} [\hat{H}_{tot}(t), \hat{\rho}(t)]}_{\text{Liouvillian, unitary evolution}} \\ &+ \underbrace{\sum_n \frac{1}{2} (2\hat{C}_n \hat{\rho}(t) \hat{C}_n^\dagger - \hat{\rho}(t) \hat{C}_n^\dagger \hat{C}_n - \hat{C}_n^\dagger \hat{C}_n \hat{\rho}(t))}_{\text{Lindbladian, non-unitary evolution}} \end{aligned} \quad (2.48)$$

[46]. We see that the state of the system, described by $\hat{\rho}$, evolves in a unitary way (through the Liouvillian) and

non-unitary way (through the Lindbladian). The Liouvilian describes the evolution of the qubit-cavity system as if it were completely disentangled from the environment. The non-unitary part, on the other hand, does represent the interaction with the environment, leading to a loss of coherence. The collapse operators \hat{C}_n quantify the dissipation and dephasing.



3. Methodology

In this chapter, we discuss the methods and parameters that we have used for the numerical simulations and measurements of sideband transitions. The numerical simulations were performed to predict the physical behaviour of the chip and to explore the influences of the different parameters. The measurements were performed to experimentally demonstrate the sideband transitions and to test our understanding of them.

An important decision in the beginning of the project has been to make use of a single-junction transmon qubit, rather than a double-junction SQUID.¹ The latter consists of superconducting loop interrupted by two Josephson junctions [17, 18, 47] and has the advantage that its overall transition frequency can be tuned in situ by applying a magnetic field through the loop. This characteristic is the device's disadvantage as well, because the SQUID has to be shielded extremely well from environmental fields to minimize dephasing. To not suffer from this experimental difficulty, we have chosen to use a single-junction transmon qubit that is by no means affected by flux noise.

3.1 Numerical simulations

The simulations of the Duffing and Kerr oscillator are based on the Hamiltonians $\hat{\mathcal{H}}_D$ of eq. (2.25) and $\hat{\mathcal{H}}_K$ of eq. (2.27), respectively, where they are coupled to the cavity. Analytically, these models take on an infinitely large Hilbert space (an infinite amount of energy levels), but since this is impossible to simulate computationally and since we are only interested in the low-excitation regime, we truncate the Hilbert space after 10 qubit levels and 10 resonator levels. We have checked that expansion of the 10×10 -dimensional Hilbert space does not yield more accuracy and that thus 10 levels is sufficient to encompass the lower levels that we are interested in.

All simulations are performed in Python with use of the QuTiP package [48, 49]. The code written for all simulations in this thesis is open-source and made public on GitHub.²³

3.1.1 Time evolution solver

All time-domain simulations are performed by the mesolve module of QuTiP, which provides functions to solve the Lindblad master equation of eq. (2.48). Strictly speaking, the LME is not meant for time-dependent problems since it is derived from a system described by a time-independent Hamiltonian. However, in many cases (and especially for weak driving) the LME turns out to be useful for solving time-dependent problems [50]. Its validity will be checked in chapter 4 by comparing it to analytical theory.

In the simulations within this thesis we will not consider the qubit's and cavity's decoherence rates (non-unitary evolution). This has two advantages. Firstly, it is easier to find the sideband transition rate. As we ap-

ply just the right drive frequency for the resonance condition, we will see full population inversion that is not reduced by decay. Secondly, calculating the Lindbladian is very computationally expensive. So by restricting ourselves to the Liouvillian, we dramatically reduce the computation times without the loss of crucial information.⁴

3.1.2 Rise and fall

In our simulations of the sideband transitions, we initialize the system at $t_0 = 0$ in an eigenstate of the un-driven and uncoupled system. When considering the red sideband transitions, we initialize the cavity in its ground state and the qubit in its excited state. When interested in the blue sideband transitions, both the qubit and cavity start in their ground state.

$$\begin{aligned} |\psi\rangle_{0,R} &= |e\rangle_q \otimes |0\rangle_c \\ |\psi\rangle_{0,B} &= |g\rangle_q \otimes |0\rangle_c \end{aligned} \quad (3.1)$$

To mimic the time-domain experiment, we have to couple to the qubit and cavity, which shifts the energy levels of the coupled system with respect to those of the uncoupled system. Step-wise adding the coupling and drive at full strength (a diabatic kick) will induce dramatic oscillatory behaviour in the qubit and cavity populations. Therefore, in order to let the system adapt to the dressed and driven eigenstates, the coupling strength $g(t)$ and drive strength $\epsilon_d(t)$ are adiabatically increased during a time $T_{\text{rise}} = 10 \text{ ns} \gg 2\pi/\epsilon_d$. This way, the system's state adiabatically follows the shift of the now dressed $|g, 0\rangle$ or $|e, 0\rangle$ energy level, which decreases the amplitude of the micromotion.⁵ Another reason to adiabatically increase the drive specifically is a practical one. Applying a diabatic kick will in practice show a distorted step function because it requires a wide range of frequencies in Fourier space.

To prevent distortion in the drive pulse, the adiabatic rise is shaped as the left half of a Gaussian curve. This left half contains three standard deviations of the total Gaussian curve. A Gaussian curve is nowhere exactly zero, so a small finite discontinuity of the coupling and driving strength (and their derivatives) will be observed at $t = 0$. However, including three standard deviations is sufficient to neglect this discontinuity and still have an adiabatic transformation.

⁴Technically speaking, the decoherence rates of the qubit and cavity do shift their resonance frequencies, but as this frequency is much larger than the resonator's linewidth (corresponding to a large quality factor), this effect is extremely small and can be neglected.

⁵Note that to better mimic the atomic beam experiment with circuit QED, we should initiate the undriven system in one of its dressed eigenstates and keep the qubit and cavity always maximally coupled. The dressed energy levels in our simulations then correspond to the bare energy levels in the cavity QED experiment. The drive is subsequently adiabatically introduced and adiabatically removed again.

¹SQUID stands for Superconducting Quantum Interference Device.

²<https://github.com/wouterkesselsap/thesis>

³Parts of this section will be submitted for publication.

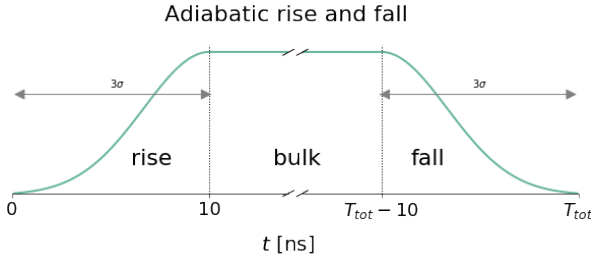


Figure 3.1: Adiabatic rise and fall of the coupling and drive. The rise and fall are both Gaussian-shaped, including three standard deviations each.

After the rise we let the system evolve for a time T_{bulk} at constant, maximum g and ϵ_d . We require $T_{\text{bulk}} \gg T_{\text{rise}}$ to consider the effect of the rise negligible. At the end of the simulation, we adiabatically decrease $g(t)$ and $\epsilon_d(t)$ again, according to the right half of the same Gaussian curve. This *fall* contains three standard deviations over a period of $T_{\text{fall}} = T_{\text{rise}} = 10$ ns as well. The total simulated time period thus equals $T_{\text{tot}} = T_{\text{rise}} + T_{\text{bulk}} + T_{\text{fall}}$.

3.1.3 Batches

The `mesolve` function outputs the quantum states and expectation values of desired operators at predefined points in time. It is desirable for later analysis to save all these quantum states. Especially for large simulations (either in time or in Hilbert space) or when we take very fine time steps, keeping all the states in the working memory quickly consumes all RAM, which will kill the simulation. To save RAM, the total simulation is divided into batches. All quantum states and calculated quantities within one batch are saved to a binary data file using the Python `pickle` package. The last state of a certain batch is used to start the evolution covered by the next batch. When the entire simulation is finalized, the calculated quantities are extracted from all batch files and saved to separate binary files so that they can be read out quickly during analysis of the simulation.

3.1.4 Sideband resonance condition

The resonance condition is found when we observe full sideband oscillations, that is, when they have maximum amplitude and lowest frequency. We find this condition when the drive frequency provides precisely enough energy to induce transitions between the two involved states ($|e, 0\rangle \leftrightarrow |g, 1\rangle$ for the red transitions and $|g, 0\rangle \leftrightarrow |e, 1\rangle$ for blue). Finding this resonance condition is not trivial due to the AC Stark shift and Bloch-Siegert⁶ shift of the levels. The dispersive coupling contributes to these shifts, just as the drive

strength and drive frequency. We can calculate the driven qubit shift $\delta\omega_q$ only to limited accuracy (see section 2.3.3 and appendix D). On top of that, we have assumed that $\delta\omega_q$ does not depend on the dispersive coupling shifts of the levels, but the correlation might not be fully negligible. So how to find the resonance condition for our sideband transitions?

First, we make an estimate of the required drive frequency ω_d for a specified drive strength ϵ_d . We do this by sweeping the drive frequency ω_d . For every value we calculate the dispersive coupling shift numerically by diagonalizing the undriven Hamiltonian, and $\delta\omega_q$ analytically by eq. (2.43) or eq. (D.8). If we sum these two effects, we can determine the energy gap between the two levels relevant for our desired sideband transition. When the drive frequency we sweep best matches the energy gap between the two relevant levels, we have found our estimate of the sideband resonance condition.

This, however, is just an estimate. The next step is to find the resonance condition with numerical time-domain simulations. We sweep the drive frequency ω_d again, this time around the estimate we obtained. For every ω_d we perform a time simulation. From the quantum states $|\psi(t)\rangle$ throughout a simulation we extract the probabilities to measure the system to be in one of the two relevant states. So for the red sideband transitions we calculate the quantities $P_{|e,0\rangle}$ and $P_{|g,1\rangle}$, and for the blue sideband transitions $P_{|g,0\rangle}$ and $P_{|e,1\rangle}$. At the resonance condition, these pairs of probabilities would oscillate in anti-phase (red) or in phase (blue). To catch these probability pairs in one quantity we consider the combined probability $P_{|e,0\rangle} - P_{|g,1\rangle}$ for the red transitions and $P_{|e,1\rangle} - P_{|g,0\rangle}$ for the blue, which oscillate between 1 and -1 . We have found the resonance condition when the oscillation amplitude of the combined probability is largest. Typically, we determine the resonance condition down to 100 kHz precision. Figure 3.2 shows the dependence of the sideband oscillations on the applied drive frequency ω_d . Animations that demonstrate finding the resonance condition can be found on this thesis's GitHub repository.⁷

3.1.5 Convergent method

In section 2.3.3 we have seen that the oscillating drive shifts the qubit frequency by a constant amount $\delta\omega_q$ and an oscillating part $\eta(t)$. During a simulation, we will observe this fast oscillatory effect of $\eta(t)$ in the calculated quantities as so-called *micromotion* (see for example fig. 3.3). This micromotion, however,

⁶Where the AC Stark shift refers to the shift that can be explained within the RWA, the Bloch-Siegert shift refers to the observed additional shift that can only be explained beyond the RWA.

⁷https://github.com/wouterkesselsap/thesis/blob/master/figures/sweepmethod_P_single.gif, https://github.com/wouterkesselsap/thesis/blob/master/figures/sweepmethod_qc_single.gif

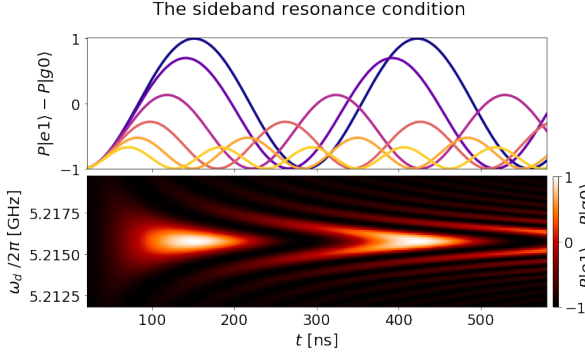


Figure 3.2: Top: Numerically simulated blue sideband oscillations for different drive frequencies ranging from $\omega_d/2\pi = 5.2158$ GHz (blue) to $\omega_d/2\pi = 5.2118$ GHz (yellow). All are performed at equal drive strength $\epsilon_d/2\pi = 0.3$ GHz. The sideband resonance condition is found at full population inversion ($\omega_d/2\pi = 5.2158$ GHz, blue). Bottom: Colour map of $P|e,1\rangle - P|g,0\rangle$, where black is -1 and white is 1 . The oscillations from the top panel are a selection of horizontal cuts from the bottom panel.

is not what we would measure experimentally in a time domain measurement. This is because, in the time-domain measurement, we measure the qubit state after the drive has been turned off, and during the fall of the drive the micromotion vanishes.

In order to obtain the system's evolution without the micromotion, we vary T_{bulk} , which is for every data point preceded by T_{rise} and followed by T_{fall} . The first data point can then be obtained for $T_{\text{bulk}} = 0$ ns after $T_{\text{tot}} = T_{\text{rise}} + T_{\text{fall}} = 20$ ns. Note that the population will not only evolve during T_{bulk} , but during the rising and falling time as well. This results in a global phase shift with respect to the evolution with micromotion. This can be seen from the offset in $P|e,1\rangle - P|g,0\rangle$ in fig. 3.3c at $T_{\text{bulk}} = 0$ ns. Animations of the evolution with the convergent method can be found on this thesis's GitHub repository.⁸

3.1.6 Transition rate

The final goal is to obtain the strength of the sideband coupling for specific device and drive parameters. We can extract that quantity from the sideband transition rate by looking at the distance in time between two subsequent extrema. This is only possible when we use the convergent method, because in that case, the extrema really give direct information about the transition rate. When micromotion is present, there are many local extrema and we cannot directly extract the sideband transition rate. The downside of the convergent method is that it is rather computationally intensive.

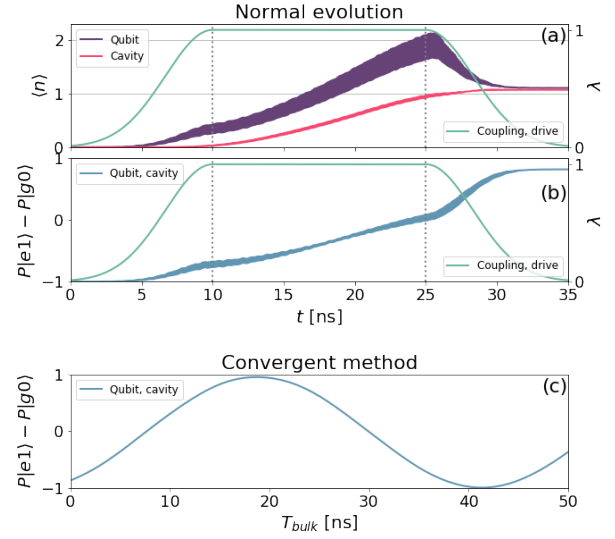


Figure 3.3: Numerical simulations illustrating the micromotion and the convergent method under strong driving ($\epsilon_d/2\pi = 0.7$ GHz). $\lambda = \epsilon_d(t)/\epsilon_{d,\max} = g(t)/g_{\max}$ (a) Expectation values $\langle \hat{b}^\dagger \hat{b} \rangle$ and $\langle \hat{a}^\dagger \hat{a} \rangle$ of the qubit and cavity number operators over time. The lines appear irregularly thick because of the micromotion with frequency $2\omega_d$. The difference in population between the qubit and cavity arises from the fact that the drive populates the qubit. The cavity population reaches a value of slightly more than 1 under this strong driving, because the drive is transferred through the qubit to the cavity as well. During the fall of the drive, the qubit and cavity populations converge to a single value. (b) Combined probability of the two involved eigenstates. (c) Simulation of the resonance condition in (a) and (b) performed with the convergent method. The bulk time T_{bulk} (time where $g(t)$ and $\epsilon_d(t)$ are maximum) is varied between 0 and 50 ns. Because the expectation values of the number operators converge during the fall of the drive, the micromotion is eliminated by the convergent method. The offset at T_{bulk} arises from the fact that the system already experiences a fraction of the sideband transition during only the rise and the fall of the drive.

To extract the transition rate from a signal that contains micromotion, we have to filter out the micromotion.

In an attempt to achieve this, we apply a Savitsky-Golay filter [51] to the combined probability $P|e,0\rangle - P|g,1\rangle$ or $P|e,1\rangle - P|g,0\rangle$. This filter fits a polynomial to the signal's data points in the least-squares sense. How effectively the micromotion is filtered out depends on many factors such as the filter's polynomial order and window length, the sideband transition rate, the micromotion's frequency and amplitude, etc. All these variables make it difficult to estimate the optimal filter settings, and a suboptimal choice of these settings may still leave some micromotion in the filter, resulting in more extrema than desired (see fig. 3.4).

Rather than manually tuning the filter settings, we cluster the local extrema in the remaining micromotion based on their distance from the signal mean. If we then determine the maximum or minimum of these clus-

⁸https://github.com/wouterkesselsap/thesis/blob/master/figures/convmethod_P.gif, https://github.com/wouterkesselsap/thesis/blob/master/figures/convmethod_qc.gif

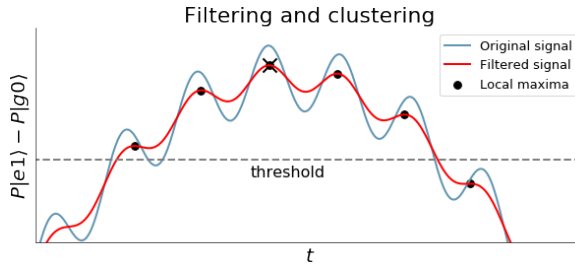


Figure 3.4: Schematic of clustering local extrema into one extremum. The blue signal represents the combined probability $P_{[e,1]} - P_{[g,0]}$ of a blue sideband transition and contains micromotion. The red graph represents the Savitsky-Golay-filtered signal of the original signal. The parameters of the filter in this example are chosen such to illustrate that the micromotion is not completely filtered out, resulting in multiple local maxima (minima), where only one maximum (minimum) is desired to determine the sideband transition rate. For the region of the signal where a maximum is desired, of all local maxima above a certain threshold, only the highest maximum is considered. For the region of the signal where a minimum is desired (not shown in the figure), of all local minima below a certain threshold, only the lowest minimum is considered. With one maximum and one minimum, the sideband transition rate can be determined.

ters, we can determine the sideband transition rate Ω_{sb} through their temporal spacing.

3.1.7 Parameters

For the numerical simulation we have chosen conceptual, experimentally relevant parameters as shown in section 3.1.7. There are simulations performed of the actual chip as well, with the parameters measured in section 3.2. Their values can be found in the next section.

Parameter	Value	Unit
ω_q	6.5	2π GHz
ω_c	4.0	2π GHz
g	0.2	2π GHz
E_C	0.2	2π GHz
N_q	10	
N_c	10	

Table 3.1: Conceptual parameters for the simulations. N_q and N_c are the number of qubit and cavity levels considered, respectively.

3.2 Measurements

We will start this section with a walk through the cryogenic setup. Though circuit QED allows for designing and engineering all parameters and elements of the chip, most parameters of the setup will have to be measured or calculated for the desired precision. We will describe the methods that we have used to determine these parameters and we show the results. We will finish this

section with describing the methodology of measuring the sideband transitions.

3.2.1 Cryogenic setup

The chip is made of a silicon substrate with mounted on it a transmon qubit, a readout CPW resonator, a feedline, a transmission line, a driveline, and an (unused) storage CPW resonator. An optical microscopy image of the chip is shown in fig. 3.6. Fig. 3.5 shows its electric circuit representation.

The transmon qubit consists of two superconducting aluminium electrodes, separated by an aluminium oxide barrier. It is shunted by a capacitance $C_B = 46.7$ fF. The readout cavity is a $\lambda/4$ NbTiN (light color in fig. 3.6) CPW resonator with its open end (the voltage anti-node) near the qubit. We will use this cavity to measure the qubit state as well as to induce the sideband transitions on. The transmission line carries microwave probe signals to one side of the readout cavity and collects what is transmitted from them through the cavity. The driveline is fabricated with its voltage anti-node near the qubit. Although the closed end of the readout cavity is also relatively near to the end of the driveline, the effective direct coupling between the two is negligible.

The second (storage) cavity is a $\lambda/4$ CPW resonator with its first mode resonance at 2.9 GHz and a linewidth of 50 kHz. This cavity is present on the chip for the photon storage in the eventual atomic beam experiment. For our two-photon sideband transitions, though, it stays unused. Its first mode's coupling g_s to the transmon is only 40 MHz. Since the dispersive coupling shifts of the lower levels scale with g_s^2 , the presence of the storage cavity hardly affects the qubit and readout cavity (less than 1 MHz according to numerical diagonalization of the un-driven Hamiltonian). To prevent the qubit from coupling to the first higher mode of the storage cavity, it is positioned at its voltage node. For even higher cavity modes, the detuning between them and the qubit becomes too large to play an effective role.

Because we do not use this storage cavity in the measurements of the thesis, we will simply refer to *the readout cavity as the cavity*.

To detect single-photon excitations we cannot do our experiments at room temperature, since the signal of a single excitation would be undetectable due to the thermal noise. Therefore, we perform our measurements at cryogenic temperatures inside a BlueFors LD dilution refrigerator. Specifically, the thermal occupation of the qubit's and cavity's excited states is negligibly small when $k_B T \ll \hbar\omega_q, \hbar\omega_c$, where k_B is Boltzmann's constant and T is the temperature in Kelvin [30]. In our experiments,

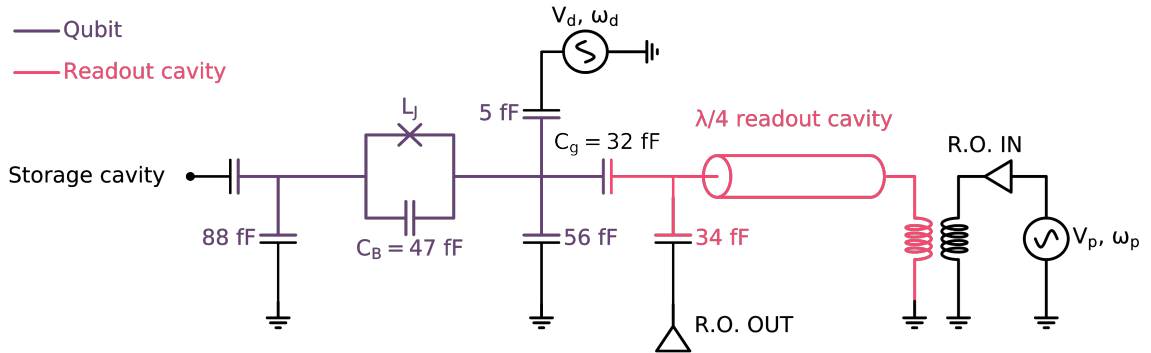


Figure 3.5: Circuit representation of the relevant chip elements and instrumentation.

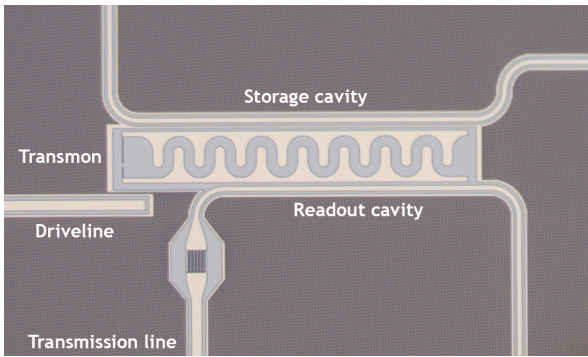


Figure 3.6: Optical microscopy image of the chip. It is (apart from the junction at the left side of the transmon) fabricated of silicon (grey colour) and NbTiN (light colour). Around the different circuit elements, the silicon substrate is covered with a punctured NbTiN layer, which is the reason it appears darker on this image.

we will operate our chip mounted on a $T = 10 \text{ mK}$ plate (see fig. 3.8), which corresponds to $k_b T / \hbar \omega_c \simeq 0.05$ or an average number of excitations of

$$\bar{n} = \frac{1}{\exp\left(\frac{\hbar\omega}{k_b T}\right) - 1} \simeq 10^{-9}. \quad (3.2)$$

This shows us that our device is well in the ground state and hardly affected by thermal excitations.

3.2.2 Noise reduction

Besides temperature-dependent quantum fluctuations, there are many sources of noise that we have to suppress in order to obtain valuable data. This section will cover several of the noise sources and methods to reduce their effects.

The signals to and from the readout cavity are generated and processed by a vector network analyzer

(VNA)⁹ at room temperature. The weakest controlled signals it can produce are still of too high power to be useful for our low-excitation experiments. Therefore, we need to attenuate the power. The distribution of the attenuators over the different temperature stages is shown in fig. 3.7. The reason to distribute them in this manner is because attenuators always produce heat and worsen the signal-to-noise ratio. Letting all attenuation happen at room temperature would produce a lot of thermal noise. On the other hand, if we did all the attenuation at the 10 mK stage where there is much less thermal noise, it would heat up the fridge, which would in return again add more thermal noise. The distribution as in fig. 3.7 is thus a compromise.

High-frequency noise from the driveline may unintentionally excite the qubit. To shield the qubit from this, a VLF-3800+ low-pass filter is positioned at the 10 mK stage [52]. Furthermore, high-frequency radiation from the environment can excite both the qubit and the cavity. Therefore, the chip is additionally shielded by a silicon-oxide cylinder.

Other noise sources may come from cable losses and resonances, spin vortices in the NbTiN layer¹⁰, fluctuations in the Josephson energy E_J due to defects in the junction's aluminium-oxide layer or in the dielectric environment, uncontrolled defects at surfaces and interfaces of the junction, or material contaminants [53].

The VNA offers several features to reduce trace noise and the noise floor [54]. One of the two that we will use is averaging, with which each data point is based on the average of multiple independent measurements. This thus reduces the effect of random noise. Since the

⁹We have used a VNA of Keysight and one of Rohde & Schwarz.

¹⁰These spin vortices may create small magnetic fields that affect the currents through the junction. To suppress the presence of spin vortices in the NbTiN layer, the layer is pinned with a grid of holes, which gives the visually darker shaded area in fig. 3.6.

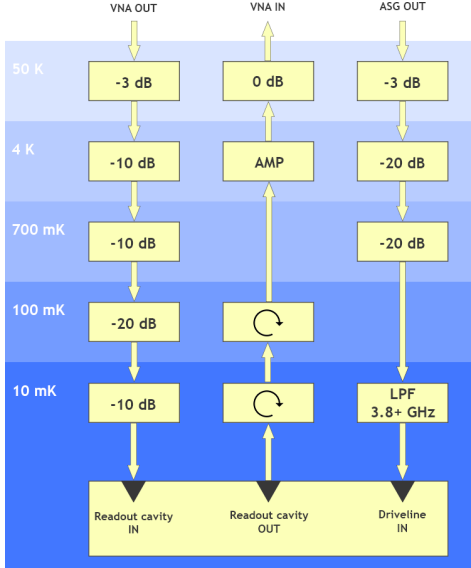


Figure 3.7: Distribution of attenuations, circulators and lowpass filter over the different temperature stages. The vector network analyzer (VNA) applies a probe tone to the readout cavity and measures the transmitted signal. The drive is generated by an arbitrary signal generator (ASG).

radio frequency (RF) signal from the device is usually much too high in microwave systems to process its information, the frequency is down-converted to an intermediate frequency (IF) using a local oscillator (LO) and a non-linear mixer [55]. We can see this conversion in the trigonometric identity

$$\sin \omega_{\text{RF}} t \cdot \sin \omega_{\text{LO}} t = \frac{1}{2} [\cos(\omega_{\text{RF}} - \omega_{\text{LO}})t - \cos(\omega_{\text{RF}} + \omega_{\text{LO}})t], \quad (3.3)$$

where the RF and LO signals are combined to a difference and sum frequency signal. The VNA sends the IF signal through an adjustable band-pass filter, which can go down to a minimum width of 1 Hz. Each tenfold reduction of the IF bandwidth lowers the noise floor by 10 dB. The practical trade-off, however, is that narrower IF bandwidths require longer sweep times.

3.2.3 Device parameters

This section covers the methods to determine some specific parameters of the chip. Though the chip is carefully fabricated, the production process never yields the exact same values for the physical parameters as designed. Per parameter we will describe the method used to determine it and show the results.

Dressed cavity resonance

For measuring the dressed cavity frequency $\tilde{\omega}_c$, we sweep the probe frequency ω_p to the cavity at low power

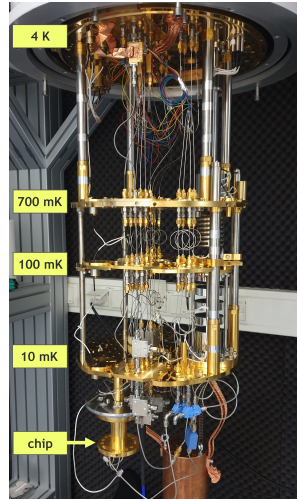


Figure 3.8: Photograph of the inside of the BlueFors LD dilution refrigerator. The different temperature stages are indicated.

and measure the squared transmission amplitude $|S_{21}|^2$. When the probe is at resonance with the cavity, the cavity becomes populated with probe photons. Since a CPW resonator is effectively a Fabry-Perot cavity, the transmitted signal intensity $|S_{21}|^2$ increases.

We retrieve the dressed cavity resonance $\tilde{\omega}_c$ and the cavity linewidth κ from a least-squares Lorentzian fit to the measured spectrum:

$$|S_{21}|^2 = \frac{A}{2\pi} \frac{\kappa}{(\omega - \tilde{\omega}_c)^2 + \kappa^2/4} + B. \quad (3.4)$$

This yields $\tilde{\omega}_c/2\pi = 4.0753$ GHz, corresponding to ω_p with the highest transmission amplitude in the top panel of fig. 3.9. The cavity linewidth κ is determined to be 10 MHz. This readout CPW is designed to have such a large linewidth to make it easy to find its resonance. The dominant source of dissipation is the loss of photons through the input and output ports [3].

It is important that the qubit stays in its ground state during these measurements, because we have seen in section 2.2 that a change in the qubit state will shift the cavity resonance.

Undressed cavity resonance

Since the qubit and cavity are mounted on the chip substrate, we cannot uncouple them. There is, however, a way to directly measure the undressed cavity frequency ω_c , which is extensively described in [32]. If we apply a very high probe power to the cavity, the states above the system's cosine potential become populated. Here, the cavity adopts the transition frequency ω_c , independent of which state is populated. Effectively, the cavity is then decoupled from the qubit and we can make a

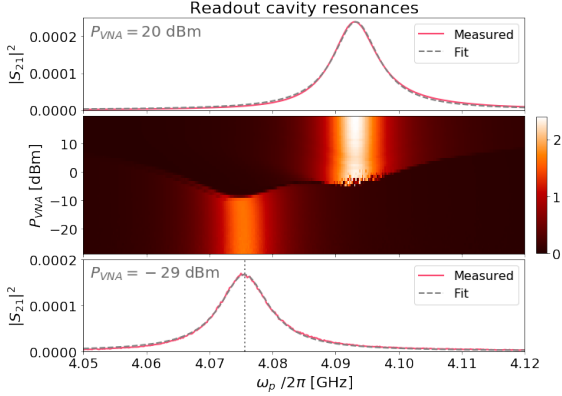


Figure 3.9: Measurement of dressed and undressed readout cavity resonances ($\tilde{\omega}_c$ and ω_c , respectively). **Top:** Measurement and Lorentzian fit of undressed ω_c . The transmission spectrum $|S_{21}|^2$ is obtained by sweeping the probe frequency at constant high power $P_{VNA} = 20$ dBm. The graph is a horizontal cut from the most upper region of the 2D plot in the middle panel. **Middle:** Measured squared cavity transmission amplitude $|S_{21}|^2$, obtained by sweeping the probe frequency ω_p and probe power P_{VNA} at the VNA output port. **Bottom:** Measurement and Lorentzian fit of dressed $\tilde{\omega}_c$. The transmission spectrum $|S_{21}|^2$ is obtained by sweeping the probe frequency at constant low power $P_{VNA} = -29$ dBm. The graph is a horizontal cut from the most lower region of the 2D plot in the middle panel.

measurement of the undressed cavity frequency ω_c . We find $\omega_c/2\pi = 4.0931$ GHz (cyan line in fig. 3.9).

Dressed qubit resonance

To measure the dressed qubit frequency $\tilde{\omega}_q$ we use two-tone spectroscopy and perform a QND measurement. We fix a low-power probe to the cavity at $\omega_p = \tilde{\omega}_c$ and simultaneously apply a pump to the qubit. When we sweep the pump frequency ω_d and hit the dressed qubit resonance $\tilde{\omega}_q$, the qubit will become excited. When monitored, the cavity's transmission S_{21} will be observed to go down since the dressed cavity resonance has shifted. This is shown in fig. 3.10.

The dressed qubit resonance $\tilde{\omega}_q$ and the linewidth γ are obtained from a Lorentzian fit through the measured

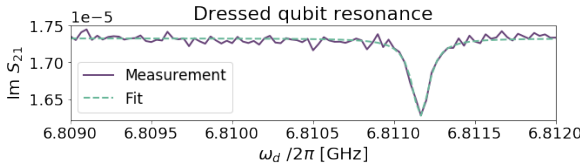


Figure 3.10: Two-tone spectroscopy measurement of the first, dressed qubit transition frequency $\tilde{\omega}_q$. The imaginary part $\text{Im } S_{21}$ of the cavity transmission is obtained by sweeping the drive frequency ω_d to the qubit, while keeping the probe frequency ω_p fixed at the dressed cavity resonance $\tilde{\omega}_c$. A Lorentzian fit through the spectrum is used to determine $\tilde{\omega}_q$ and the qubit linewidth γ as the spectrum's FWHM.

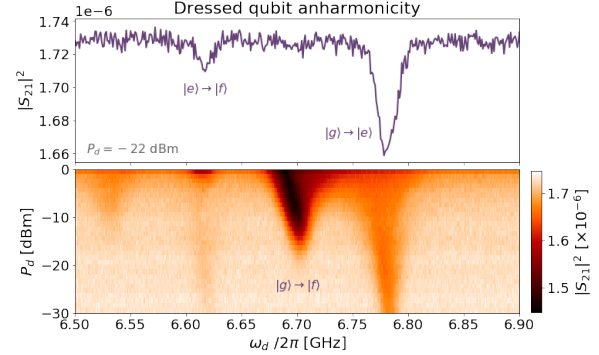


Figure 3.11: Two-tone spectroscopy measurement of the qubit anharmonicity. Data is obtained with 20 dB less attenuation at room temperature compared to the other measurements in this thesis. **Top:** Squared cavity transmission amplitude $|S_{21}|^2$, obtained by sweeping the drive frequency ω_d to the qubit, while keeping the probe frequency ω_p fixed at the dressed cavity resonance $\tilde{\omega}_c$. When the qubit is excited by ω_d , the cavity requires a different frequency to become populated. Because ω_p is fixed at $\tilde{\omega}_c$, this results in a drop of the transmission S_{21} . The graph is a horizontal cut at drive power $P_d = -22$ dBm from the 2D plot in the bottom panel. **Bottom:** Measured squared cavity transmission amplitude $|S_{21}|^2$, obtained by sweeping the drive frequency ω_d at fixed probe frequency ω_p for different drive powers P_d at the output port of the arbitrary signal generator (ASG). The different transitions shift in frequency as a function of the drive power P_d .

spectrum. We find $\tilde{\omega}_q/2\pi = 6.811$ GHz and $\gamma/2\pi = 129$ kHz.

Where the cavity linewidth κ does not depend on the probe power, the qubit linewidth γ does, because high probe power excites the qubit through the dispersive coupling [38]. The pump and drive power affect the qubit's decoherence rate as well.

Dressed qubit anharmonicity

The qubit's dressed anharmonicity $\tilde{\zeta}_q$ can be measured with two-tone spectroscopy as well. In that case, we also sweep the pump power. In the colour plot of fig. 3.11 of $|S_{21}|^2$, we see that at certain combinations of pump power and frequency, higher qubit transitions are induced, like $|e\rangle \rightarrow |f\rangle$ with a single photon (because the qubit is weakly thermally excited) or $|g\rangle \rightarrow |f\rangle$ with two photons. From the peak-to-peak distance in the top panel of fig. 3.11, we find the dressed qubit anharmonicity to be $\tilde{\zeta}_q = 150$ MHz.

Non-measurables

With circuit QED it is impossible to measure certain quantities directly, such as the undressed qubit frequency ω_q , the charging energy E_C , and the coupling strength g . Instead, we have to numerically estimate them, based on the parameters that we have measured. To this extend, we diagonalize the Hamiltonian $\hat{\mathcal{H}}_D$ in the Duffing approximation (eq. (2.25)) to obtain the

dressed energy levels. For a specific set of ω_q , E_C , and g , we can compare these levels to the measured $\tilde{\omega}_q$, $\tilde{\omega}_c$, and $\tilde{\zeta}_q$.

We perform this comparison through a cost function R which is based on the variables that we have measured. By defining a grid in the parameter space spanned by ω_q , E_C , and g , we can calculate the value of R at every point in this grid. A single point in this space thus corresponds to a single set of ω_q , E_C , and g . If we substitute these parameters, together with the measured value for ω_c , into the Duffing Hamiltonian $\hat{\mathcal{H}}_D$, we can calculate $\tilde{\omega}_q$, $\tilde{\omega}_c$, and $\tilde{\zeta}_q$ by diagonalizing $\hat{\mathcal{H}}_D$. The cost function R then gives a measure for how close these values of the specific model are compared to what we have measured. Specifically,

$$\begin{aligned} R^2(\omega_q, E_C, g) = & (\tilde{\omega}_q, \text{meas} - \tilde{\omega}_q, \text{calc})^2 \\ & + (\tilde{\omega}_c, \text{meas} - \tilde{\omega}_c, \text{calc})^2 \\ & + (\tilde{\zeta}_q, \text{meas} - \tilde{\zeta}_q, \text{calc})^2. \end{aligned} \quad (3.5)$$

The coordinates (ω_q, E_C, g) where we find the minimum of R is then the best estimate of ω_q , E_C , and g . Figure 3.12 shows the heat map of R on three two-dimensional, mutually orthogonal slices through the coordinate (ω_q, E_C, g) where R is minimized. Each slice has one of these parameters taken constant and the other two as independent variable. We find $\min R$ at $\omega_q/2\pi = 6.807$ GHz, $E_C/h = 138$ MHz, and $g/2\pi = 193$ MHz. Furthermore, we note that ω_q , E_C , and g are clearly correlated in $\min R$.

3.2.4 Sideband transitions

Now that we have obtained values for the relevant parameters of our device, we can discuss how to demonstrate the sideband transitions experimentally. This last section of the methodology chapter will set out the methods to measure the blue and red sideband transitions,

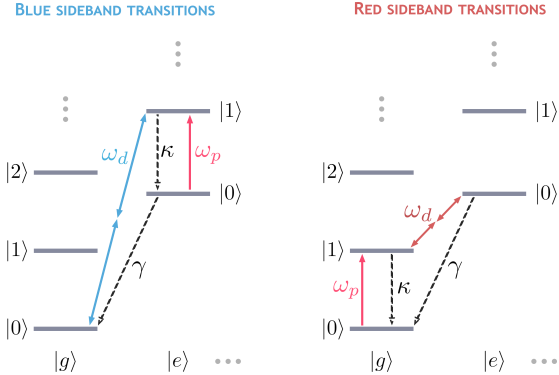


Figure 3.13: Energy level diagram with relevant interactions for blue and red sideband transitions. ω_d indicates the drive frequency that induces the sideband transitions, ω_p is the probe frequency to the cavity, κ is the cavity decay rate (fast) and γ the qubit decay rate (slow).

and introduce the models from which we will extract the sideband coupling.

Blue sideband transitions

To measure the blue sideband transitions we make use of two-tone spectroscopy. A drive is applied to the qubit at fixed power, of which we sweep the frequency ω_d . When ω_d matches half of the energy difference between $|g, 0\rangle$ and $|e, 1\rangle$, both the qubit and cavity become simultaneously populated. The system is transferred from $|g, 0\rangle$ to $|e, 1\rangle$. Since the cavity has a much larger linewidth than the qubit ($\kappa \gg \gamma$), the system decays quickly to $|e, 0\rangle$. A probe tone to the cavity at its resonance frequency $\tilde{\omega}_c$ brings the system back to $|e, 1\rangle$. The drive returns it subsequently to $|g, 0\rangle$ again [56]. This so-called Lambda system is schematically shown in fig. 3.13.¹¹

¹¹Note that because the transition frequency of $|g, 0\rangle \rightarrow |g, 1\rangle$ is close to $|e, 0\rangle \rightarrow |e, 1\rangle$ (~ 2 MHz difference), and that of $|g, 0\rangle \rightarrow |e, 1\rangle$ close to $|g, 1\rangle \rightarrow |e, 2\rangle$ (~ 3 MHz difference), we will probably induce sideband transitions between $|g, 1\rangle$ and $|e, 2\rangle$ as well [56].

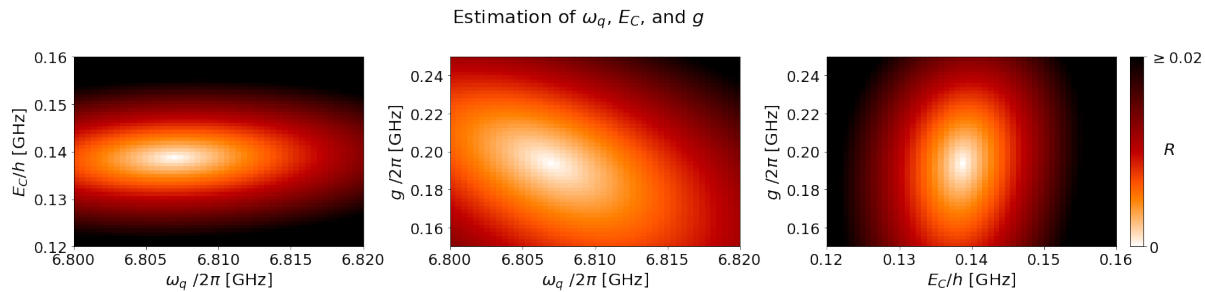


Figure 3.12: Heat maps of the cost function R of eq. (3.5) on different, mutually orthogonal slices from the (ω_q, E_C, g) parameter space. Each slice contains the coordinates (ω_q, E_C, g) where R has its minimum, and has one of these parameters taken constant while the other two are independent variables. The coordinate where R is minimized corresponds to the best estimate of ω_q , E_C , and g in $\hat{\mathcal{H}}_D$.

To extract the sideband coupling g_{sb} , we fit a model to our obtained data. To reduce computation times, we use a simplified model in the normal mode basis that contains only the relevant interactions at the sideband resonance condition. The model is described by the Hamiltonian

$$\begin{aligned}\hat{\mathcal{H}}'_{f,B} = & (\tilde{\omega}_q - 2\omega_d + \omega_p)\hat{\beta}^\dagger\hat{\beta} - \frac{\zeta_q}{2}\hat{\beta}^\dagger\hat{\beta}^\dagger\hat{\beta}\hat{\beta} \\ & + (\tilde{\omega}_c - \omega_p)\hat{\alpha}^\dagger\hat{\alpha} - 2\chi_{qc}\hat{\beta}^\dagger\hat{\beta}\hat{\alpha}^\dagger\hat{\alpha} \\ & - g_{sb}(\hat{\alpha}\hat{\beta} + \hat{\alpha}^\dagger\hat{\beta}^\dagger) + i\epsilon_p(\hat{\alpha}^\dagger - \hat{\alpha}).\end{aligned}\quad (3.6)$$

The derivation of this model can be found in appendix E.

We link this model to our measurements of S_{21} through the expectation value $\langle\hat{\alpha}\rangle$ of the cavity field on the steady-state solution ρ_{ss} . These are calculated with QuTiP's `expect` and `steadystate` functions, respectively. There are several unknown (free) parameters in this model when we fit it to our measurement data —the qubit depolarization rate γ_1 (because driving the qubit changes its depolarization time T_1), the driven qubit shift $\delta\omega_q$, the scaling factor A , the noise floor B , the dressed cavity frequency $\tilde{\omega}_c$ (which appears to fluctuate by a few hundred kHz), and of course the sideband coupling g_{sb} . We fit the quadrature $|\text{Tr}(\rho_{ss}\hat{a})|^2$ to the measurement data in the least-squares sense and extract from this fit the sideband transition rate g_{sb} .

Red sideband transitions

We use two-tone spectroscopy to measure the red sideband transitions as well. A probe tone is applied to the cavity at fixed power of which the frequency is swept around the dressed cavity resonance $\tilde{\omega}_c$. When the probe is at resonance with the cavity, it brings the system from $|g,0\rangle$ to $|g,1\rangle$. Simultaneously, we apply a drive to the qubit. We fix its power but sweep the frequency ω_d . When $2\omega_d$ matches the energy difference between $|g,1\rangle$ and $|e,0\rangle$, the cavity depopulates and the energy flows to the qubit.

To extract the sideband coupling g_{sb} for the red sideband transitions, we fit a model to our measurement data that is obtained in a way similar to that of the blue sideband case. The simplified red model is characterized by the Hamiltonian

$$\begin{aligned}\hat{\mathcal{H}}'_{f,R} = & (\tilde{\omega}_q - 2\omega_d - \omega_p)\hat{\beta}^\dagger\hat{\beta} - \frac{\zeta_q}{2}\hat{\beta}^\dagger\hat{\beta}^\dagger\hat{\beta}\hat{\beta} \\ & + (\tilde{\omega}_c - \omega_p)\hat{\alpha}^\dagger\hat{\alpha} - 2\chi_{qc}\hat{\beta}^\dagger\hat{\beta}\hat{\alpha}^\dagger\hat{\alpha} \\ & - g_{sb}(\hat{\alpha}^\dagger\hat{\beta} + \hat{\alpha}\hat{\beta}^\dagger) + i\epsilon_p(\hat{\alpha}^\dagger - \hat{\alpha}).\end{aligned}\quad (3.7)$$

The sideband coupling g_{sb} is in the same way extracted from a fit of $|\text{Tr}(\rho_{ss}\hat{a})|^2$ to the measurement data as a function of the free parameters.



4. Results

In this chapter, we show and discuss the most important findings regarding sideband transitions between a superconducting qubit and cavity. First, we demonstrate the significant difference between the Duffing and Kerr approximations in the sideband transition rate. From numerical simulations, the red sideband transition rate appears to be 2.8 times faster within the Duffing approximation and the blue sideband transition rate 1.9 times faster. Secondly, we prove the importance of including the counter-rotating terms in the Hamiltonian representation of the microwave drive. In the case of the red sideband transitions, this increases the transition rate by a factor 3. Finally, we discuss the results of experimental measurements of sideband transitions. We measure the red sideband transition rate to be 57% of the simulated rate and the blue sideband transition rate to be between 59% and 65% of the simulated rate. We find, however, an unexpected non-linear dependence of the blue sideband transition rate on the applied driving power.

4.1 Comparison of the Duffing and Kerr approximation

The first striking result we find in comparing the Duffing oscillator to the Kerr oscillator. In section 2.1.3 and section 2.1.5, we have seen that the Duffing oscillator is derived from the Cooper pair box by assuming only small phase deviations from $\varphi = 0$. The Kerr oscillator is subsequently derived by neglecting the Duffing oscillator's self-interaction, which corresponds to applying the rotating wave approximation. The Duffing and Kerr systems are defined as the undriven Duffing and Kerr oscillator, respectively, coupled to a cavity:

$$\hat{\mathcal{H}}_D = (\hbar\omega_q + E_C)\hat{b}^\dagger\hat{b} - \frac{E_C}{12}(\hat{b} + \hat{b}^\dagger)^4 + \hbar\omega_c\hat{a}^\dagger\hat{a} + \hbar g(\hat{b} + \hat{b}^\dagger)(\hat{a} + \hat{a}^\dagger), \quad (4.1)$$

$$\hat{\mathcal{H}}_K = \hbar\omega_q\hat{b}^\dagger\hat{b} - \frac{E_C}{2}\hat{b}^\dagger\hat{b}^\dagger\hat{b}\hat{b} + \hbar\omega_c\hat{a}^\dagger\hat{a} + \hbar g(\hat{b} + \hat{b}^\dagger)(\hat{a} + \hat{a}^\dagger). \quad (4.2)$$

We have performed time domain simulations of sideband transitions with the Duffing oscillator and Kerr oscillator, according to the methods presented in section 3.1. The parameters of the models are of experimentally relevant values. The qubit has the frequency parameter $\omega_q/2\pi = 6.5$ GHz and charging energy $E_C/h = 0.2$ GHz. The cavity has a frequency $\omega_c/2\pi = 4.0$ GHz. The vacuum Rabi coupling strength is $g = 0.2$ GHz. Figure 4.1 shows the important differences in the simulation results between the Duffing and Kerr oscillator.

First of all, the required drive frequencies to obtain the resonance condition for sideband transitions is very different for both oscillators. For drive strengths ϵ_d ranging from 0.2 to 0.6 GHz, the required ω_d for the red sideband transitions differ between 7 and 14 MHz between the Duffing and Kerr approximation. For the blue sideband transitions the difference is between 11 and 37 MHz.

On one side, this is due to the fact that the system with the Duffing oscillator undergoes different level shifts due to the dispersive coupling, than the system with the Kerr oscillator. The energy gap between the undriven $|g, 1\rangle$ and $|e, 0\rangle$ levels (involved in the red transitions) is in the Kerr approximation 13 MHz larger than in the Duffing approximation. This explains why we need a larger ω_d for the red sideband transitions when using the Kerr oscillator. For the blue sideband transitions, the larger required ω_d for the Kerr's transitions can be understood from the finding that the energy gap between the undriven $|g, 0\rangle$ and $|e, 1\rangle$ levels within the Kerr approximation is 17 MHz larger than in the Duffing approximation.

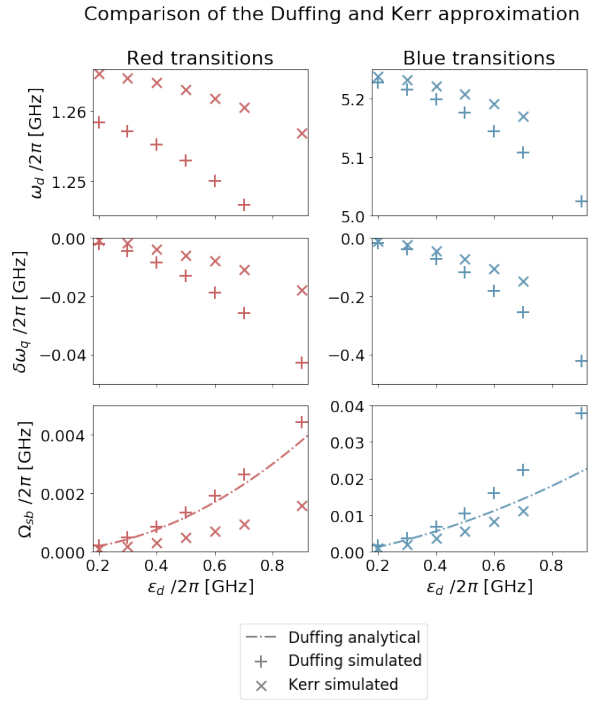


Figure 4.1: Comparison of numerical sideband simulations between the Duffing and Kerr approximation. **Top:** Required drive frequency ω_d for the resonance condition as a function of drive strength ϵ_d . **Middle:** Driven qubit shift $\delta\omega_q$, calculated by comparing ω_d to the dispersive coupling shifts. **Bottom:** Observed sideband transition rate. Comparison to analytical theory is used as benchmark for the validity of the simulation results. The graph of the analytically calculated Ω_{sb} is a second-order polynomial fit through the analytical data obtained at the same values of ϵ_d as used for the simulations.

On the other side, the differences in required ω_d arise from the fact that the Duffing oscillator responds differently to being driven than the Kerr oscillator, as can be seen from the two middle panels in fig. 4.1. The driven qubit shift $\delta\omega_q$ is determined by comparing $2\omega_d$ to the dressed energy levels in question:

$$\delta\omega_q = \begin{cases} 2\omega_d - (E_{|e,0\rangle} - E_{|g,1\rangle}) & (\text{red}) \\ 2\omega_d - (E_{|e,1\rangle} - E_{|g,0\rangle}) & (\text{blue}). \end{cases} \quad (4.3)$$

The most important difference between the Duffing and Kerr approximation, though, is that the sideband transition rate, for a given drive strength ϵ_d , is significantly higher in the Duffing oscillator. On average, the red sideband transitions occur 2.8 times faster and the blue sideband transitions 1.9 times faster (see two lowest panels in fig. 4.1). Figure 4.2 shows four time-domain simulations that immediately clarify the difference. From our derivation in chapter 2 we know that the Duffing oscillator is always a better approximation of the transmon

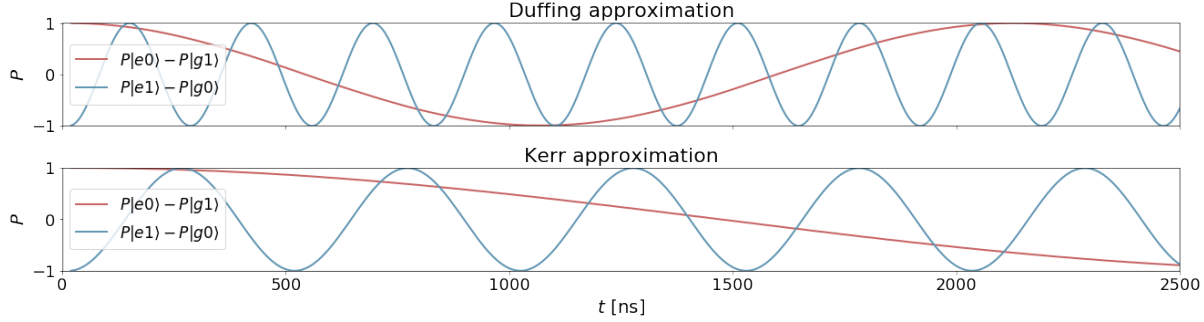


Figure 4.2: Time-domain simulation of sideband transitions within the Duffing and Kerr approximation. The colour indicates the type of transitions. The blue sideband transition rate is clearly faster than the red, and the transition rates with the Duffing oscillator are faster than with the Kerr oscillator. The conceptual parameters from section 3.1.7 are used, together with the covgent method and a drive strength $\epsilon_d/2\pi = 0.3$ GHz.

than the Kerr oscillator. In the case of sideband transitions, however, the impact of the Kerr approximation on the transition rate appears to be significant. Our simulation data shows that when considering sideband transitions in a qubit-cavity system, the Duffing approximation is significantly better than the Kerr approximation.

4.2 Counter-rotating drive terms

The second finding regards another rotating wave approximation that is commonly made —neglecting the counter-rotating terms in the drive Hamiltonian. The full drive Hamiltonian $\hat{\mathcal{H}}_d$ is given by

$$\hat{\mathcal{H}}_d = 2\epsilon_d \cos(\omega_d t) (\hat{b} + \hat{b}^\dagger). \quad (4.4)$$

When we discard the fast oscillating terms of this Hamiltonian in the interaction picture (applying a RWA), we obtain

$$\hat{\mathcal{H}}'_d = \epsilon_d (\hat{b} e^{+i\omega_d t} + \hat{b}^\dagger e^{-i\omega_d t}), \quad (4.5)$$

where we have assumed ϵ_d to be real-valued.

To investigate the impact of neglecting the counter-rotating terms in $\hat{\mathcal{H}}_d$, we have performed several time-domain simulations within the Duffing approximation with $\epsilon_d/2\pi = 0.3$ GHz and $\epsilon_d/2\pi = 0.7$ GHz. In both cases we have found that neglecting the counter-rotating drive terms significantly reduce the sideband transition rate (see table 4.1). The blue sideband transition rate is around 20% slower. The red sideband transition rate has been reduced by a striking factor of 3.

These results show the breakdown of the RWA in the drive. In fact, the RWA is only valid when $\Delta_{qd} \ll \Sigma_{qd}$. With the experimentally relevant parameters that we have chosen ($\omega_q/2\pi = 6.5$ GHz, $\omega_c/2\pi = 4.0$ GHz), the error on the blue sideband transitions is smaller, where we have $\Delta_{qd}/2\pi \approx 1.3$ GHz and $\Sigma_{qd}/2\pi \approx 11.8$

GHz. The impact is much higher on the red sideband transition rate, though, since there $\Delta_{qd}/2\pi \approx 5.3$ GHz is much more similar in size to $\Sigma_{qd}/2\pi \approx 7.8$ GHz.

We see that even when Δ_{qd} and Σ_{qd} differ an order of magnitude in size, the impact on the sideband coupling can still be a significant 20%. The required precision depends on the aim of a specific experiment, but for most relevant circuit QED setups involving sideband transitions, the counter-rotating drive terms play a significant role in the system dynamics.

	$\epsilon_d/2\pi$ [GHz]	$\frac{\Omega_{sb}/2\pi}{\hat{\mathcal{H}}_d}$ [MHz]	$\frac{\Omega_{sb}/2\pi}{\hat{\mathcal{H}}'_d}$ [MHz]	ratio
Red	0.3	0.4760	0.1664	0.35
	0.7	2.641	0.9120	0.34
Blue	0.3	3.678	2.902	0.79
	0.7	22.21	17.12	0.77

Table 4.1: Sideband transitions rates within the Duffing approximation for a full drive Hamiltonian $\hat{\mathcal{H}}_d$ (eq. (4.4)) and $\hat{\mathcal{H}}'_d$ which lacks the counter-rotating terms (eq. (4.5)).

4.3 Experimental demonstration of sideband transitions

In this section, the results of the actual measurements of sideband transitions are shown. We find the red and blue sideband transitions by sweeping a probe tone to the cavity around the cavity resonance $\tilde{\omega}_c$ and sweeping a drive tone to the qubit. The sideband coupling is extracted from a least-squares Lorentzian model fit to the data. Figures 4.3 and 4.4 show an example of blue and red sideband measurements and their fitted models.

The sideband transitions are measured for different drive powers P_d at the output port of an arbitrary signal

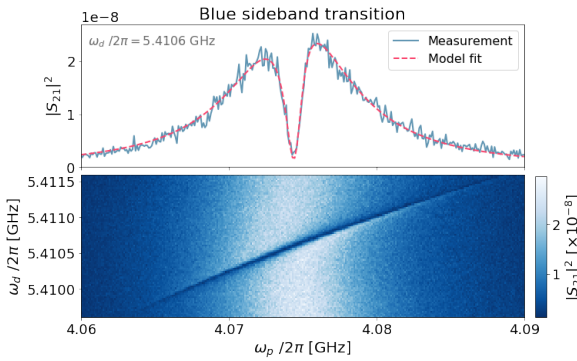


Figure 4.3: Measurement and fit of blue sideband transitions. **Top:** Cavity transmission spectrum $|S_{21}|^2$, obtained by sweeping the probe frequency ω_p at fixed drive frequency $\omega_d/2\pi = 5.4106$ GHz. The graph is a horizontal cut from the bottom 2D plot. Pink striped line is a least-squares Lorentzian model fit of eq. (3.6) through the measurement data. **Bottom:** Measured squared cavity transmission amplitude $|S_{21}|^2$, obtained by sweeping both the probe frequency ω_p and drive frequency ω_d . Probe and drive power are kept constant at -20 dBm and 1 dBm, respectively. The transparency window through this two-dimensional frequency space is slightly curved since the qubit frequency is shifted by ω_d .

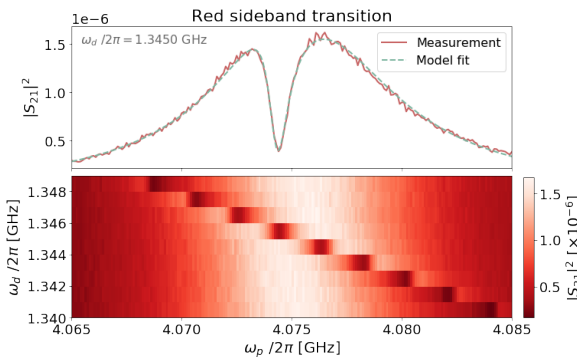


Figure 4.4: Measurement and fit of red sideband transitions. **Top:** Cavity transmission spectrum $|S_{21}|^2$, obtained by sweeping the probe frequency ω_p at fixed drive frequency $\omega_d/2\pi = 1.3450$ GHz. The graph is a horizontal cut from the bottom 2D plot. Striped line is a least-squares Lorentzian model fit of eq. (3.7) through the measurement data. **Bottom:** Measured squared cavity transmission amplitude $|S_{21}|^2$, obtained by sweeping both the probe frequency ω_p and drive frequency ω_d . Probe and drive power are kept constant at -30 dBm and 7 dBm, respectively.

generator (ASG). Since we use a single-junction qubit, we do not have a direct method to accurately calibrate the drive strength ϵ_d at the chip to the ASG's drive power P_d , based on solely measurements. Therefore, we have to compare the measurements to simulations. Specifically, we relate ϵ_d to P_d through the driven qubit shift $\delta\omega_q$. At the sideband resonance condition, $2\omega_d$ must bridge the energy gap between the two energy levels involved. Together with our knowledge of the dressed energy levels (remember that we have measured $\tilde{\omega}_q$ and $\tilde{\omega}_c$, and that we can find $E_{|e,1\rangle}$ through diagonalization of $\hat{\mathcal{H}}_D$), we can determine $\delta\omega_q$.

We have performed simulations of the sideband transitions for various ϵ_d , with the parameters of our chip substituted into the system Hamiltonian $\hat{\mathcal{H}}_D$ (see appendix H for the results). If we map $\delta\omega_q$ of our measurements onto a polynomial fit through $\delta\omega_q$ of our simulations as a function of ϵ_d , we can get an estimate of ϵ_d for our different measurements. The result of this calibration can be seen in the top panel of fig. 4.5. These values of ϵ_d are subsequently used to plot the sideband transition rate of the measurements as a function of ϵ_d .

We have benchmarked our simulations by the analytical theory of the sideband transition rate provided in section 2.3.4. For weak driving ($\epsilon_d \leq 0.3$ GHz), the error of the simulated rate compared to analytical theory is below 1%. For stronger driving (up to $\epsilon_d = 0.7$ GHz) we find a maximum error of 14%. The good agreement justifies the use of our simulation methods.

4.3.1 Red sideband transitions

Figure 4.4 shows an example measurement of the red sideband transition. The bottom panel demonstrates that the transparency window shifts as we sweep the drive frequency ω_d or the probe frequency ω_p . Figure 3.13 schematically showed that the probe is used to bring the system to $|g, 1\rangle$ and the right drive frequency depopulates the cavity by inducing a transition to $|e, 0\rangle$. However, if ω_p is not exactly at resonance with the $|g, 0\rangle \leftrightarrow |g, 1\rangle$ transition, the difference in energy can be compensated for by the drive frequency. Together, the probe and the drive mediate the transitions between $|g, 0\rangle$ and $|e, 0\rangle$. Specifically, we observe red sideband transitions if

$$2\omega_d + \omega_p = (E_{|e,0\rangle} - E_{|g,0\rangle}) / h = \tilde{\omega}_q + \delta\omega_q. \quad (4.6)$$

The measurement data of the red sideband transitions is taken at drive powers P_d ranging between -1 and 5 dBm at the ASG output port. These are mapped to

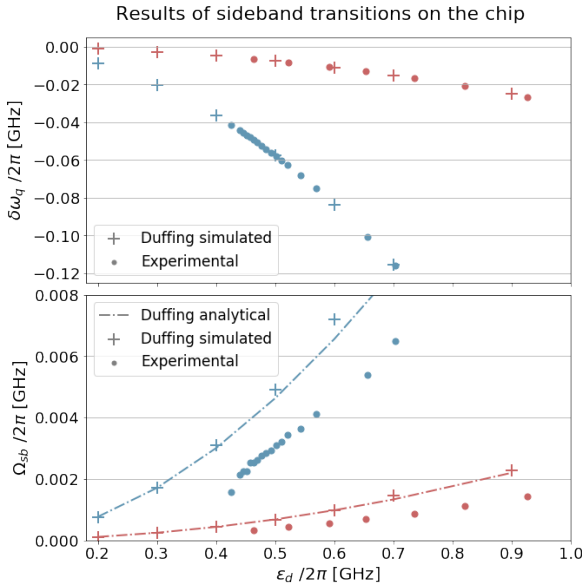


Figure 4.5: Simulation, measurement and analytical results of the sideband transitions on the chip. The Duffing approximation is used for the simulations and in the analytical theory. **Top:** Measured and simulated driven qubit shift $\delta\omega_q$. The measurements are linked to the drive strength ϵ_d through $\delta\omega_q$ by mapping them to a polynomial that is fitted through the simulation data. The colour indicates the type of sideband transitions. **Bottom:** Simulated, measured and analytical sideband transition rate as a function of chosen or fitted drive strength ϵ_d .

values of ϵ_d between 0.48 GHz and 0.93 GHz. Table B.1 shows the values of the red sideband measurements.

In the bottom panel of fig. 4.5, we have plotted the sideband transition rate Ω_{sb} against the drive strength ϵ_d . The transition rate of all measurement data is about 57% of that of the simulations.¹ This result shows us that we have been able to capture the major part of the relevant physics involved in the sideband transitions in our simulation algorithm and analytical theory. Though our model is a very simplified version of reality, established by many approximations, the fact that there is only a 43% difference between measurements and simulations shows the power of our model.

Nonetheless, in an attempt to explain the difference between the measurements on one side and the simulations and theory on the other, we examine the influence of some of the approximations and simplifications made in our model.

The first simplification is that the simulations are per-

formed without decoherence effects. This is because of practical reasons, such as shorter computation times and the fact that the large cavity linewidth prevents us from observing full sideband oscillations. From a theoretical perspective, damping shifts a resonator's resonant frequency with respect to its undamped version:

$$\omega = \omega_0 \sqrt{1 - \frac{1}{4Q^2}}, \quad (4.7)$$

where ω_0 is the undamped resonance frequency and Q is the resonator's quality factor. Simulations that do include the finite qubit and cavity linewidths γ and κ show us the resonance conditions at exactly the same ω_d as without decoherence (to 100 kHz precision).

This can be understood from the cavity's quality factor $Q_c = \omega_c/\kappa \approx 400$. Though 10 MHz is for many practical purposes a rather large linewidth, its effect on the cavity's resonance frequency is negligible.

Another possibility could be that strong driving increases the transmon's phase deviations from $\varphi = 0$ such that they cannot be properly captured anymore by only a fourth-order cosine expansion. In the quantum rotor analogy, the drive is represented by a constant magnetic field that works on the charged mass. A simulation including the sixth-order cosine expansion with $\epsilon_d = 0.7$ GHz shows an 8.4% decrease of the sideband transition rate.²

Though this brings the simulated rate closer to the measured transition rate, the effect is too small to explain the 43% difference. Moreover, to be a valid explanation for the difference, the presumable effect of the higher cosine term should decrease the transition rate at any ϵ_d . However, at $\epsilon_d = 0.4$ GHz, the inclusion of the sixth-order cosine expansion does not decrease the transition rate but in fact increases it with 0.1%.

Of the readout cavity we have so far considered only its lowest mode $\tilde{\omega}_c = 4.0753$ GHz. Since it is a $\lambda/4$ -cavity, the first higher mode can be expected around $\omega_{c_2} \approx 12$ GHz with a coupling strength to the qubit of $g_2 \approx 0.6$ GHz. Note that although g_2 is notably larger than g , the detuning $\omega_{c_2} - \omega_q$ is also much larger compared to the first mode.

Including this second mode shifts the dressed energy levels dramatically. With $\epsilon_d = 0.7$ GHz, for example, the required drive frequency for the resonance condition differs by about 50 MHz, compared to not considering the higher mode. Unfortunately, the effect on the rate of the red sideband transitions is an increase of 1%,

¹Because the measurement data corresponds to different drive strengths ϵ_d than in the simulation data, the measured Ω_{sb} is compared to a second-order polynomial fit through the simulation data.

²Note that when including the sixth-order cosine expansion, we have to redo the calculation of the parameters ω_q , E_C , and g . In that case, these come down to $\omega_q/2\pi = 6.804$ GHz, $E_C/h = 0.145$ GHz, and $g/2\pi = 0.193$ GHz.

so neglecting the higher cavity mode cannot account for the mismatch in Ω_{sb} between the simulations and measurements.

Although the above three simplifications —neglecting decoherence, truncation of the cosine expansion of the transmon’s potential after the fourth power, and neglecting the higher modes of the readout cavity —have appeared not to be responsible for the mismatch in Ω_{sb} between the simulations and measurements, our rigorous examination of them justifies these approximations in the picture of sideband transitions.

4.3.2 Blue sideband transitions

An example of blue sideband transitions is given in fig. 4.3. The drive mediates the transitions between $|g, 0\rangle$ and $|e, 1\rangle$, the probe between $|e, 1\rangle$ and $|e, 0\rangle$. We notice that, in contrast to the red sideband case, to obtain the transparency window an increase in probe frequency requires an increase in drive frequency as well. This is because in our Lambda system, the drive and probe together induce transitions between $|g, 0\rangle$ and $|e, 0\rangle$. So specifically, blue sideband transitions are observed when

$$2\omega_d - \omega_p = (E_{|e,0\rangle} - E_{|g,0\rangle}) / h = \tilde{\omega}_q + \delta\omega_q. \quad (4.8)$$

The measurement data of the blue sideband transitions is taken at drive powers P_d ranging between -12 and 12 dBm at the ASG output port. These are mapped to values of ϵ_d between 0.43 GHz and 0.70 GHz. All values can be found in table B.2. When plotting the observed transition rates in fig. 4.5, we see that they are quite close to the simulations and analytical theory. In fact, there is between 59% and 65% agreement in Ω_{sb} (the data point with the lowest drive power $P_d = -12$ dBm is an exception with 47%). This even exceeds the accuracy of the red sideband predictions.

From the numbers in table B.2 and the top panel in fig. 4.5, we observe two curious results. Firstly, we note that the range of used ASG output powers is much larger for the blue sideband transitions than for the red (compare $[-12, 12]$ dBm (blue) to $[-1, 5]$ dBm (red)), while the range of ϵ_d what they are mapped to is shorter for the blue transitions. This is due to the curve of the driven qubit shift $\delta\omega_q$ as a function of ϵ_d being steeper for the simulated blue sideband transitions (see fig. 4.5). This has the consequence that an equal increase in ϵ_d results in a larger driven qubit shift $\delta\omega_q$.

Secondly, $\delta\omega_q$ of the measurements starts with an offset of -42 MHz at $P_d = -12$ dBm (most left blue

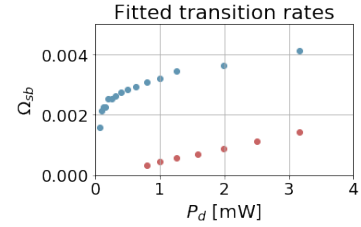


Figure 4.6: Sideband transition rate Ω_{sb} of measurements as a function of applied drive power P_d at the output port of the ASG.

measurement data point in the top panel of fig. 4.5). At very low drive powers, we expect the driven qubit frequency $\delta\omega_q$ to go to zero, though. One could argue measuring at even lower P_d to find $\delta\omega_q$ going to zero. However, measurements at lower drive power than $P_d = -12$ dBm were unsuccessful because of the sideband transitions being too weak to be observable.

A possible source of the shorter ϵ_d range and the offset in $\delta\omega_q$ can be the frequency dependence of the ratio between the drive power at the output port of the ASG and the drive power at the chip. For a given drive power at the chip, we need a specific frequency to induce the sideband transitions. If, due to the many attenuators, cables, and electronics between the ASG and the chip, the transmitted power depends strongly on frequency, unexpected results can be observed. If for one frequency, for example, the power is strongly attenuated, we require a different frequency to find the sideband resonance condition. But this new frequency results in yet a different power attenuation which requires another drive frequency, etc.

We see the effect of this in the transition rate as a function of the applied drive power. We would expect the transition rate to scale linearly with the applied power [18], and go to zero as the power goes to zero. However, from fig. 4.6 we see that this linearity does not hold for the blue sideband transitions.

A possible source of this non-linear relation could be the VLF-3800+ lowpass filter (LPF) that is located at the 10 mK stage in the driveline. This LPF is positioned here to shield the qubit from high-frequency noise. However, from the documentation in [52] we learn that it exhibits strong frequency dependence of the insertion loss around 5.5 GHz. This is exactly the frequency region in which we apply the drive for the blue sideband transitions. This unfortunate choice of LPF results in unpredictably strong attenuations of the drive power.

Within the measurements of this thesis, the drive power at the sample is not calibrated directly to the power coming from the ASG. Instead, simulations are

required for this calibration. Having a direct relationship between P_d and ϵ_d , together with the replacement of the current LPF by one with a suitable range, would be an important improvement in the experimental setup.



5. Conclusions

We have seen that circuit quantum electrodynamics provides all-electrical control over the interactions between a superconducting artificial atom and a cavity. Performing the atomic beam experiment on such a superconducting chip will gain better understanding of the interaction between matter and individual quanta of light. Furthermore, the aim to control the photonic state of the cavity will contribute to the rapidly developing field of quantum engineering, where we control the interaction between light and matter on the smallest scales. We have argued that two-photon sideband transitions are a suitable method to realize the controllable coupling between a transmon qubit and a cavity, and provide a recipe for the atomic beam experiment on a chip.

Numerical simulations of these sideband transitions between a transmon qubit and cavity have shown that there exists a significant difference in transition rates between the Duffing and the Kerr approximation. Modelling the transmon by a Duffing oscillator yields a 2.8 times faster transition rate of the red sideband transitions than when the transmon is modelled by a Kerr oscillator. In the case of blue sideband transitions, the Duffing oscillator shows a 1.9 times faster transition rate. This significant difference proves the breakdown of the rotating wave approximation on the Duffing oscillator's self-interaction when considering sideband transitions.

Numerical simulations of sideband transitions between a Duffing oscillator and a cavity have shown that the counter-rotating terms in the Hamiltonian description of the microwave drive field have a significant impact on the sideband transition rate. Neglecting these counter-rotating terms reduces the red sideband transition rate by a factor 3 and the blue sideband transition rate by 20%. This demonstrates the breakdown of the rotating wave approximation on the counter-rotating terms in the drive Hamiltonian.

We have experimentally demonstrated the red and blue sideband transitions, and compared them to numerical simulations and analytical theory. The measured red sideband transition rate is around 57% of the simulated red transition rate. For the blue sideband transitions this is between 59% and 65%. These numbers show that our model has been able to capture a significant part of the physics that play a role in sideband transitions on our chip.

The measurements of the blue sideband transitions show a large driven qubit shift $\delta\omega_q$ of 43 MHz at the lowest drive power P_d where the transitions were still visible. A shorter range of drive strengths ϵ_d at the chip

has been found, compared to the red sideband measurements, while a larger range of drive powers is used at the output port of the arbitrary signal generator. A potential source of this unexpected behaviour is the lowpass filter at the 10 mK stage, which shows strong frequency dependencies of its insertion loss around the frequencies that are required for the blue sideband drive.



6. Outlook

With the knowledge gained from this thesis, we are one step closer to performing the atomic beam experiment on a chip. Our findings of the effects of the rotating wave approximations on the system Hamiltonians yield the ability to better predict the effective coupling between the artificial atom and the cavity.

Where we have now induced the sideband transitions on the readout cavity, one of the next steps will be to induce them on the storage cavity, for this is the cavity of which we eventually aim to control the photonic state. These measurements will be preceded by simulations to predict the required drive frequency and effective sideband coupling.

During this thesis there are already simulations performed of the atomic beam experiment. The results of these simulations can be found in appendix A. They show that with the knowledge of the effective sideband coupling and decay rates, it is possible to gain control over the state of the storage cavity. This competence will contribute to the numerous applications from the fast growing field of quantum engineering, where we take advantage of nature's characteristics at the very smallest scales.

Uncertainty estimate of the sideband coupling

We have seen that the measured red sideband transition rate is 43% smaller than the simulated transition rate. The question arises whether we have missed relevant physics in our model or if this is reasonable within the uncertainties of our measurements. Some of the parameters in our model are obtained by measurements and fitting. The uncertainties in these fits then influence the estimation of the non-measurable parameters ω_q , E_C , and g . The desired information is the scale of the impact of different parameters on the sideband transition rate.

We can, for example, perform multiple simulations with different sets of (ω_q, E_C, g) . For each simulation we examine the impact on the driven qubit shift $\delta\omega_q$ (for this is the quantity we use to determine the measured drive strength ϵ_d) and the sideband transition rate Ω_{sb} . Together with the uncertainties in the fits through the directly measured parameters, we make an estimate of the uncertainty in Ω_{sb} .

The objective is then to know to what extend we have to tune the parameters in order to let the simulated sideband coupling agree with the measured sideband coupling. If these parameter modifications are reasonable within the uncertainties of our measurements, it can be valid to adjust them. This will consequently lead to better predictions and control over the red sideband coupling.

Lowpass filter

Regarding the setup, there are several improvements that we can make. In the case of the blue sideband transitions, we have seen that the transition rate Ω_{sb} does not scale linearly with drive power P_d , though this is expected from literature [18]. We have argued that the lowpass filter at the 10 mK stage could be the source of this unexpected non-linearity, because its insertion loss depends strongly on the drive frequency around the frequencies that we require for the blue sideband transitions. This attenuates the drive power in an unpredictable and uncontrollable way. An improvement of the setup would be to replace this filter with a different low-pass filter that has a flat frequency dependence around $\omega_d/2\pi = 5.4$ GHz but shields the qubit from charge noise at frequencies around 6.8 GHz.

Drive power calibration

Beside this technical improvement, it is desirable to be able to directly calibrate the drive power P_d at the ASG output port to the drive strength ϵ_d at the chip. Within this thesis, we have had to rely on calibration to simulation results. However, we would like to relate ϵ_d to P_d solely on measurements. One way to realize this is by replacing the single-junction transmon qubit with a flux-tunable SQUID [17, 18] and calibrate ϵ_d based on Rabi oscillations.

Let us briefly discuss this procedure here. A SQUID consists of a superconducting loop interrupted by two Josephson junctions. It has the advantageous property that its dressed frequency $\tilde{\omega}_q$ can be tuned in situ by applying a magnetic flux through its superconducting loop. If we additionally apply a drive to the SQUID of power P_d and frequency ω_d , we can sweep $\tilde{\omega}_q$ to resonance with ω_d . A drive pulse will rotate the SQUID's state around the x -axis of the Bloch sphere. Specifically, this so-called Rabi angle θ_R is determined by

$$\theta_R = \int_0^{t_0} \epsilon_d(t) dt. \quad (6.1)$$

If we, for example, initiate the SQUID in its ground state $|g\rangle$, a π -pulse would excite qubit to $|e\rangle$ and a $\frac{\pi}{2}$ -pulse to $\frac{1}{\sqrt{2}}(|g\rangle + |e\rangle)$. By measuring the SQUID's state after the pulse, we know the Rabi angle within the domain $(0, 2\pi]$, which results in a measurement of the drive strength ϵ_d at the chip. We see that this calibration is entirely independent of simulations and the driven qubit shift $\delta\omega_q$.

Floquet formalism in the simulations

A final remark we will make on the simulation methods. We can make our simulation results more reliable by implementing the Floquet formalism [50]. This theory originates from solid-state physics with periodic lattices, but can also be applied in driven circuit QED systems [57].

The main reason for using Floquet theory is that it is valid for any drive strength, where the Lindblad master equation is strictly speaking not. Another advantage is that the Floquet formalism transforms a time-dependent problem with a time-periodic Hamiltonian into a time-independent problem, which is often solved much more efficiently.

Since our drive is periodic, our total Hamiltonian $\hat{\mathcal{H}}$ is too. From $\hat{\mathcal{H}}(t) = \hat{\mathcal{H}}(t + T)$, where T is the period, we can calculate the periodic Floquet modes $\Phi_\alpha(t) = \Phi_\alpha(t + T)$ and their quasi-energy levels which are uniquely defined up to multiples of $2\pi/T$. Any state can be decomposed into these Floquet modes and hence we can find the Floquet state at any arbitrary t . Beside improving the efficiency of the simulation code, we can use Floquet theory to check the validity of the current simulations where the Lindblad master equation is solved under strong driving.

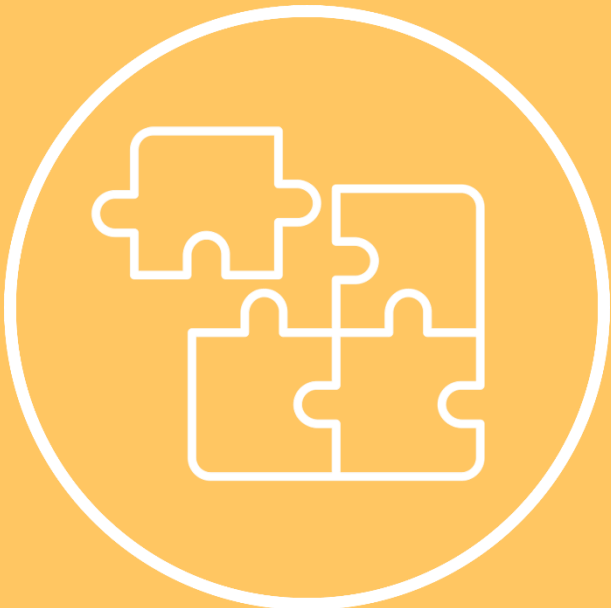
Bibliography

- [1] S. Haroche. Nobel Lecture: Controlling photons in a box and exploring the quantum to classical boundary. *Reviews of Modern Physics*, 85, July 2013. doi: 10.1103/RevModPhys.85.1083.
- [2] J.M. Raimond, J. Brune, and S. Haroche. Manipulating quantum entanglement with atoms and photons in a cavity. *Reviews of Modern Physics*, 73, July 2001.
- [3] A. Wallraff, D.I. Schuster, A. Blais, L. Frunzio, R.-S. Huang, J. Majer, S. Kumar, S.M. Girvin, and R.J. Schoelkopf. Strong coupling of a single photon to a superconducting qubit using circuit quantum electrodynamics. *Nature*, 431:162–167, September 2004. doi: 10.1038/nature02851.
- [4] L.a. Tuan. Frequency- and time-domain characterization of a transmon qubit in a transmission line. Master's thesis, Technische Universität München, February 2017. Retrieved from https://www.wmi.badw.de/publications/theses/Le%20anh_Tuan_Masterarbeit_2017.pdf.
- [5] V.B. Braginsky, Y.I. Vorontsov, and F.Y. Khalili. Quantum singularities of a ponderomotive meter of electromagnetic energy. *Journal of Experimental and Theoretical Physics*, 73(1340), 1977.
- [6] D.J. Wineland. Nobel Lecture: Superposition, Entanglement, and Raising Schrödinger's Cat, December 2012.
- [7] The Nobel Prize. Press release, October 2012. From <https://www.nobelprize.org/prizes/physics/2012/press-release/>.
- [8] Y.V. Nazarov and J. Danon. *Advanced Quantum Mechanics*. Cambridge University Press, 1 edition, 2013. ISBN 978-0-521-76150-5.
- [9] M.D. Reed. *Entanglement and Quantum Error Correction with Superconducting Qubits*. PhD thesis, Yale University, May 2013. Retrieved from <https://arxiv.org/abs/1311.6759>.
- [10] S. Haroche, M. Brune, and J.M. Raimond. From cavity to circuit quantum electrodynamics. *Nature Physics*, March 2020. doi: 10.1038/s41567-020-0812-1.
- [11] A. Blais, S.M. Girvin, and W.D. Oliver. Quantum information processing and quantum optics with circuit quantum electrodynamics. *Nature Physics*, 17, March 2020. doi: 10.1038/s41567-020-0806-z.
- [12] Y.A. Pashkin, O. Astafiev, T. Yamamoto, Y. Nakamura, and J.S. Tsai. Josephson charge qubits: a brief review. *Quantum Information Processing*, 8:55–80, February 2009. doi: 10.1007/s11128-009-0101-5.
- [13] B.D. Josephson. Possible new effects in superconducting tunneling. *Physics Letters*, 1–7:251–253, 1962. doi: 10.1016/0031-9163(62)91369-0.
- [14] J.M. Martinis, M.H. Devoret, and J. Clarke. Energy-Level Quantization in the Zero-Voltage State of a Current-Biased Josephson Junction. *Physical Review Letters*, 55(1543), October 1985. doi: 10.1103/PhysRevLett.55.1543.
- [15] J.E. Mooij, T.P. Orlando, L. Levitov, L. Tian, C.H. van der Wal, and S. Lloyd. Josephson persistent-current qubit. *Science*, 285(5430), August 1999. doi: 10.1126/science.285.5430.1036.
- [16] V. Bouchiat, D. Vion, P. Joyez, D. Esteve, and M.H. Devoret. Quantum Coherence with a Single Cooper Pair. *Physica Scripta*, T76:165–170, 1998. doi: 10.1238/Physica.Topical.076a00165.
- [17] J. Koch, T.M. Yu, J. Gambetta, A.A. Houck, D.I. Schuster, J. Majer, A. Blais, M.H. Devoret, S.M. Girvin, and R.J. Schoelkopf. Charge insensitive qubit design derived from the Cooper pair box. *Physical Review A*, 76(4), March 2007. doi: 10.1103/PhysRevA.76.042319.

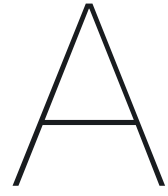
- [18] A. Wallraff, D.I. Schuster, A. Blais, J.M. Gambetta, J. Schreier, L. Frunzio, and M.H. Devoret. Sideband Transitions and Two-Tone Spectroscopy of a Superconducting Qubit Strongly Coupled to an On-Chip Cavity. *Physical Review Letters*, 99(050501), July 2007. doi: 10.1103/PhysRevLett.99.050501.
- [19] P.J. Leek, S. Filipp, P. Maurer, M. Baur, R. Bianchetti, J.M. Fink, M. Göppl, L. Steffen, and A. Wallraff. Using Sideband Transitions for Two-Qubit Operations in Superconducting Circuits. *Physical Review B*, 79(180511(R)), May 2009. doi: 10.1103/PhysRevB.79.180511.
- [20] A. Blais, J. Gambetta, A. Wallraff, D.I. Schuster, S.M. Girvin, M.H. Devoret, and R.J. Schoelkopf. Quantum-information processing with circuit quantum electrodynamics. *Physical Review A*, 75(032329), March 2007. doi: 10.1103/PhysRevA.75.032329.
- [21] S. Bader. The Transmon Qubit, December 2013. Retrieved from <https://pdfs.semanticscholar.org/b219/01aa5b1a8302ee9601c0aa25c4a4425d9d72.pdf>.
- [22] R.P. Feynman. Simulating physics with computers. *International Journal of Theoretical Physics*, 22:467–488, 1982.
- [23] A. Kandala, A. Mezzacapo, K. Temme, M. Takita, M. Brink, J.M. Chow, and J.M. Gambetta. Hardware-efficient variational quantum eigensolver for small molecules and quantum magnets. *Nature*, 549:242–246, September 2017. doi: 10.1038/nature23879.
- [24] P.J.J O’Malley and et al. Scalable Quantum Simulation of Molecular Energies. *Physical Review X*, 6(031007), July 2016. doi: 10.1103/PhysRevX.6.031007.
- [25] C.S. Wang, J.C. Curtis, and B.J. et al. Lester. Efficient multiphoton sampling of molecular vibronic spectra on a superconducting bosonic processor, August 2019. Preprint at arXiv: <https://arxiv.org/abs/1908.03598>.
- [26] X. Gu, A.F. Kockum, A. Miranowicz, Y.-x. Liu, and F. Nori. Microwave photonics with superconducting quantum circuits. *Physics Reports*, 718–719:1–102, October 2017. doi: 10.1016/j.physrep.2017.10.002.
- [27] J.M. Martinis, H. Neven, and et al. Quantum supremacy using a programmable superconducting processor. *Nature*, 574, October 2019. doi: 10.1038/s41586-019-1666-5.
- [28] E. Pednault, J. Gunnels, D. Maslov, and J. Gambetta. On “Quantum Supremacy”, October 2019. Retrieved from <https://www.ibm.com/blogs/research/2019/10/on-quantum-supremacy/>.
- [29] J.M. Martinis and K. Osborne. Superconducting Qubits and the Physics of Josephson Junctions, 2004. Retrieved from <https://arxiv.org/abs/cond-mat/0402415>.
- [30] J.M. Fink. Quantum Nonlinearities in Strong Coupling Circuit QED. Retrieved from https://quantumids.files.wordpress.com/2015/07/fink_lap_book.pdf.
- [31] S.M. Girvin. Circuit QED: Superconducting Qubits Coupled to Microwave Photons. In M.H. Devoret, R.J. Schoelkopf, and B. Huard, editors, *Proceedings of the 2011 Les Houches Summer School on Quantum Machines*. Oxford University Press, June 2014.
- [32] R. Lescanne, L. Verney, Q. Ficheux, M.H. Devoret, B. Huard, M. Mazyar, and Z. Leghtas. Escape of a Driven Quantum Josephson Circuit into Unconfined States. *Physical Review Applied*, 11(014030), January 2019. doi: 10.1103/PhysRevApplied.11.014030.
- [33] M. Kounalakis. *Nonlinear coupling for quantum control of superconducting qubits and electrical/mechanical resonators*. PhD thesis, Delft University of Technology, 2019.
- [34] L.S. Bishop. *Circuit Quantum Electrodynamics*. PhD thesis, Yale University, May 2010. Retrieved from <https://arxiv.org/abs/1007.3520>.
- [35] S. Filipp. Qubit manipulation and rotating wave approximation, April 2012. Retrieved from https://qudev.phys.ethz.ch/static/content/courses/QSIT12/QSIT12_qubitmanipulation.pdf.

- [36] M. Abdi, M. Pernpeintner, R. Gross, H. Huebl, and M.J. Hartmann. Quantum State Engineering with Circuit Electromechanical Three-Body Interactions. *Physical Review Letters*, 114(17), February 2015. doi: 10.1103/PhysRevLett.114.173602.
- [37] A. Blais, R.-S. Huang, A. Wallraff, S.M. Girvin, and R.J. Schoelkopf. Cavity quantum electrodynamics for superconducting electrical circuits: an architecture for quantum computation. *Physical Review A*, 69(062320), June 2004. doi: 10.1103/PhysRevA.69.062320.
- [38] D.I. Schuster, A. Wallraff, A. Blais, L. Frunzio, R.-S. Huang, J. Majer, S.M. Girvin, and R.J. Schoelkopf. AC-Stark Shift and Dephasing of a Superconducting Qubit Strongly Coupled to a Cavity Field. *Physical Review Letters*, 94(123602), March 2005. doi: 10.1103/PhysRevLett.94.123602.
- [39] D.I. Schuster. *Circuit Quantum Electrodynamics*. PhD thesis, Yale University, May 2007. Retrieved from https://rsl.yale.edu/sites/default/files/files/RSL_Theses/SchusterThesis.pdf.
- [40] M.F. Gely, M. Kounalakis, C. Dickel, J. Dalle, R. Vatré, B. Baker, M.D. Jenkins, and G.A. Steele. Observation and stabilization of photonic Fock states in a hot radio-frequency resonator. *Science*, 363(6431):1072–1075, March 2019. doi: 10.1126/science.aaw3101.
- [41] M.F. Gely, G.A. Steele, and D. Bothner. The nature of the lamb shift in weakly-anharmonic atoms: from normal mode splitting to quantum fluctuations. *Physical Review A*, 98(053808), November 2018. doi: 10.1103/PhysRevA.98.053808.
- [42] M. Aspelmeyer, T.J. Kippenberg, and F. Marquardt. Cavity optomechanics. *Reviews of Modern Physics*, 86(1391), December 2014. doi: 10.1103/RevModPhys.86.1391.
- [43] J. Clarke and F.K. Wilhelm. Superconducting quantum bits. *Nature*, 453(7198), July 2008. doi: 10.1038/nature07128.
- [44] N.F. Ramsey. A Molecular Beam Resonance Method with Separated Oscillating Fields. *Physical Review*, 78(695), June 1950. doi: 10.1103/PhysRev.78.695.
- [45] E. Hahn. Spin Echoes. *Physical Review*, 80:580–594, November 1950. doi: 10.1063/1.3066708.
- [46] C.A. Brasil, F.F. Fanchini, and R. de Jesus Napolitano. A simple derivation of the Lindblad equation. *Revista Brasileira de Ensino de Física*, 35(1), October 2011. doi: 10.1590/S1806-11172013000100003.
- [47] C. Dickel. *Scalability and modularity for transmon-based quantum processors*. PhD thesis, Delft University of Technology, 2018.
- [48] J.R. Johansson, D. Nation, and F. Nori. QuTiP: An open-source Python framework for the dynamics of open quantum systems. *Computer Physics Communications*, 183(8):1760–1772, August 2012. doi: 10.1016/j.cpc.2012.02.021.
- [49] J.R. Johansson, D. Nation, and F. Nori. QuTiP: An open-source Python framework for the dynamics of open quantum systems. *Computer Physics Communications*, 184(4):1234–1240, April 2013. doi: 10.1016/j.cpc.2012.11.019.
- [50] QuTiP: Quantum Toolbox in Python. Floquet Formalism. <http://qutip.org/docs/4.0.2/guide/dynamics/dynamics-floquet.html>.
- [51] A. Savitsky and M.J.E. Golay. Smoothing and Differentiation of Data by Simplified Least Squares Procedures. *Analytical Chemistry*, 36(8):1627–1639, 1964. doi: 10.1021/ac60214a047.
- [52] Mini-Circuits. Low Pass Filter VLF-3800+. <https://www.minicircuits.com/pdfs/VLF-3800+.pdf>.
- [53] A.P.M. Place, L.V.H. Rodgers, P. Mundada, and et al. New material platform for superconducting transmon qubits with coherence times exceeding 0.3 milliseconds, February 2020. Preprint at arXiv: <https://arxiv.org/abs/2003.00024>.

- [54] Keysight Network Analyzer Support. Noise Reduction Techniques. http://na.support.keysight.com/pna/help/latest/S2_Opt/Trce_Noise.htm.
- [55] Microwaves101. Mixers. <https://www.microwaves101.com/encyclopedias/mixers>.
- [56] S. Novikov, T. Sweeney, J.E. Robinson, S.P. Premaratne, B. Suri, F.C. Wellstood, and B.S. Palmer. Raman coherence in a circuit quantum electrodynamics lambda system. *Nature Physics*, 12:75–79, January 2016. doi: 10.1038/nphys3537.
- [57] M. Grifoni and P. Hänggi. Driven quantum tunneling. *Physics Reports*, 304(5–6):229–354, October 1998. doi: 10.1016/S0370-1573(98)00022-2.
- [58] R.H. Dicke. Coherence in Spontaneous Radiation Processes. *Physical Review*, 93(99), January 1954. doi: 10.1103/PhysRev.93.99.
- [59] J.A. Mlynek, A.A. Abdumalikov, C. Eichler, and A. Wallraff. Observation of Dicke superradiance for two artificial atoms in a cavity with high decay rate. *Nature Communications*, 5(5186), November 2014. doi: <https://doi.org/10.1038/ncomms6186>.
- [60] M. Delanty, S. Rebić, and J. Twamley. Superradiance and phase multistability in circuit quantum electrodynamics. *New Journal of Physics*, 13, May 2011. doi: 10.1088/1367-2630/13/5/053032.
- [61] L. García-Álvarez, S. Felicetti, E. Rico, E. Solano, and C. Sabín. Entanglement of superconducting qubits via acceleration radiation. *Scientific Reports*, 7(657), April 2017. doi: 10.1038/s41598-017-00770-z.



Appendices



Simulations of the atomic beam experiment

In this appendix, we discuss and demonstrate time domain simulations of the atomic beam experiment. In this experiment, a multi-level transmon qubit is coupled to a storage cavity and a readout cavity. The scope of performing the atomic beam experiment on a chip is to be able to control the photonic state of the storage cavity. Controlling this state to the scale of individual photon levels can contribute to applications in the field of quantum engineering.

A.1 Setup

In this thesis, we have argued that the passage of an atom through the cavity in the atomic beam experiment (the storage cavity on our chip) can be imitated by inducing sideband transitions with a drive. When we do not drive the transmon qubit, it does not exchange energy with the storage cavity because they are dispersively coupled. This represents the atom being outside of the cavity. We make the effective (sideband) coupling g_s tunable by being able to control the sideband drive. The drive is turned on when the atom enters the cavity and turned off when it leaves the cavity. By letting the storage cavity operate in the strong coupling regime where $g_s \gg \kappa_s$, it can coherently exchange energy with the qubit.

In the atomic beam experiment, the atoms pass through the storage cavity one by one. To mimic this, we reset the qubit to its ground state after it has ‘left’ the storage cavity. This is what we use the readout cavity for, which operates in the weak coupling regime ($g_r \ll \kappa_r$).

The above motivates for the following pulse sequence. The entire system is initialized in its ground state. A pump to the qubit (realized through the drive line) applies a $\frac{\pi}{2}$ -pulse, which prepares the qubit in an equal superposition of its ground state $|g\rangle$ and excited state $|e\rangle$. Subsequently, the coupling to the storage cavity is turned on (start of the sideband drive at the resonance condition), which corresponds to the atom entering the cavity. As long as this sideband coupling is present, the qubit and storage cavity will coherently exchange energy. Next, the atom ‘leaves’ the cavity by turning off the sideband coupling to the storage cavity. Finally, a drive pulse which creates the sideband coupling to the readout cavity resets the qubit, because the energy in the qubit will flow to the readout cavity and quickly dissipate to the environment. This pulse sequence is repeated to mimic the

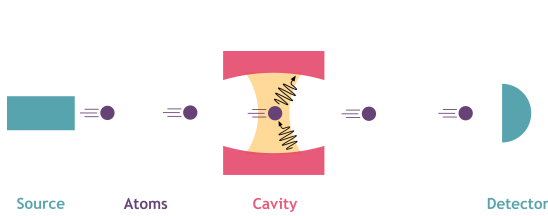


Figure A.1: Simple, schematic setup of the atomic beam experiment.

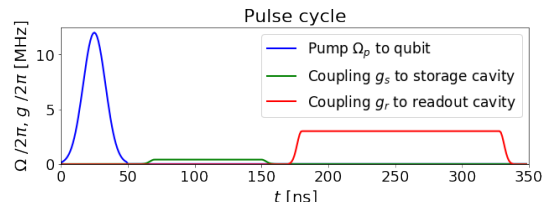


Figure A.2: Pulse sequence of the atomic beam experiment on a chip.

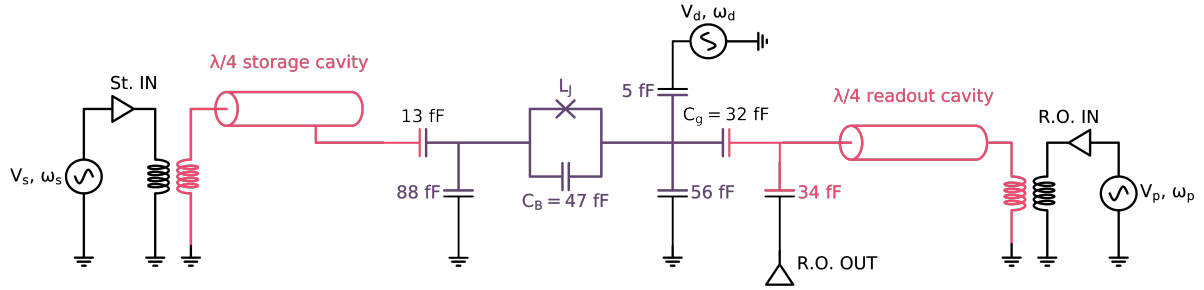


Figure A.3: Circuit representation of the chip. The cavities are drawn in pink, the qubit in purple.

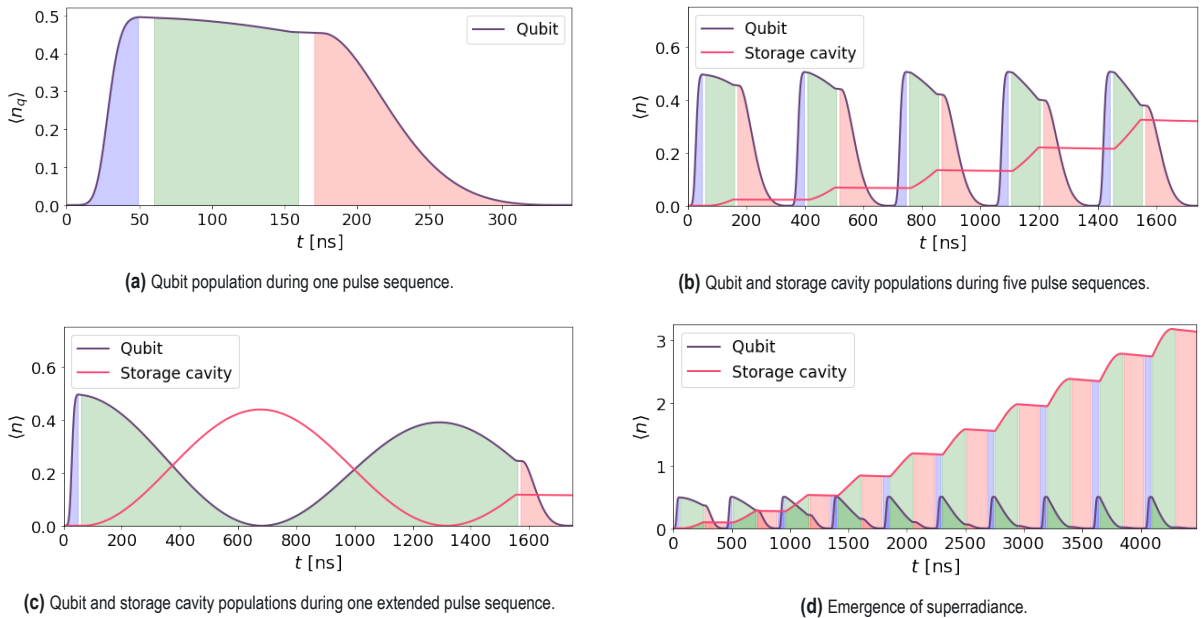


Figure A.4: Results of simulations of the atomic beam experiment. The area below the qubit population has been filled with the colours corresponding to the applied pulses.

next atom. Figure A.2 shows an example of the pulses over time. Note that all pulses have a Gaussian rise and fall as discussed in section 3.1.2.

The Hamiltonian represents a simplified model in which all interactions between the qubit and the cavities are mediated by the red sideband couplings g_s and g_r . This Hamiltonian is obtained after a similar transformation as discussed in section 3.2.4.

$$\begin{aligned} \hat{\mathcal{H}} = & -\frac{E_c}{2}\hat{b}^\dagger\hat{b}^\dagger\hat{b}\hat{b} + \chi_s n_q \hat{a}_s^\dagger \hat{a}_s + \chi_r n_q \hat{a}_r^\dagger \hat{a}_r \\ & + g_s(t) (\hat{a}_s \hat{b}^\dagger + \hat{b} \hat{a}_s^\dagger) + g_r(t) (\hat{a}_r \hat{b}^\dagger + \hat{b} \hat{a}_r^\dagger) + \frac{1}{2}\Omega_p(t) (\hat{b} + \hat{b}^\dagger) \end{aligned} \quad (\text{A.1})$$

The simulations are performed by calculation of the full Lindblad master equation of eq. (2.48). The code can be found in the Jupyter Notebook `atomic_beam.ipynb` this thesis' GitHub repository.¹

¹<https://github.com/wouterkesselsap/thesis>

A.2 Results

The impact of the pulse cycle on the qubit can be recognized well from fig. A.4a. The pump brings the qubit to an equal superposition of $|g\rangle$ and $|e\rangle$, where the probability of measuring a qubit excitation is $1/2$. Hence, $\langle n_q \rangle = \langle \hat{b}^\dagger \hat{b} \rangle = 1/2$. During the coupling to the storage cavity, the energy flows from the qubit to the storage cavity, which can be seen from fig. A.4b. The coupling to the readout cavity is tuned such as to completely reset the qubit to its ground state.

From figures A.4b and A.4c, we see that the qubit and storage cavity lose photons to the environment but only very slowly due to their high quality factors. Figure A.4c clearly shows the coherent exchange of energy between the two. With the knowledge of this transition rate and the decay rates, we gain full control over the photonic state of the storage cavity.

Another very interesting result is the finding of superradiance. Figures A.4b and A.4d show that the more photons are present in the storage cavity, the faster flows the energy from the qubit to the storage cavity. Superradiance is observed when multiple emitters are so close together that they alter the others' decay rates and decay coherently, even if only one atom contains an excitation and the others are in their ground states [58]. This superradiant behaviour has been demonstrated as well in circuit QED [59–61], but only with multiple artificial atoms. Figure A.4d suggests that we can observe superradiance in circuit QED even with only a single artificial atom.

B

Measurement and fitting data

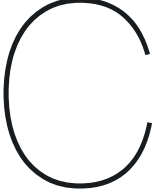
This appendix shows the measurement and fitting results of the red and blue sideband transitions. The methodology is described in section 3.2. P_d is the drive power at the output port of the ASG, ϵ_d is the drive strength or half of the drive amplitude at the chip, ω_d is the drive frequency, $\delta\omega_q$ is the shift the first qubit transition experiences due to the drive, Ω_{sb} is the sideband transition rate, and ε_Ω is the fitting error in Ω_{sb} .

Measured red sideband transitions					
P_d [dBm]	$\epsilon_d/2\pi$ [GHz]	$\omega_d/2\pi$ [GHz]	$\delta\omega_q/2\pi$ [GHz]	$\Omega_{sb}/2\pi$ [MHz]	ε_Ω [%]
-1	0.479	1.3646	-0.007	0.318	4.36
0	0.536	1.3637	-0.008	0.430	2.67
1	0.603	1.3625	-0.011	0.553	3.06
2	0.664	1.3613	-0.013	0.702	2.14
3	0.745	1.3595	-0.017	0.877	1.47
4	0.830	1.3574	-0.021	1.131	1.16
5	0.934	1.3545	-0.027	1.423	0.94

Table B.1: Measurement and fitting data of red sideband transitions.

Measured blue sideband transitions					
P_d [dBm]	$\epsilon_d/2\pi$ [GHz]	$\omega_d/2\pi$ [GHz]	$\delta\omega_q/2\pi$ [GHz]	$\Omega_{sb}/2\pi$ [MHz]	ε_Ω [%]
-12	0.426	5.42121	-0.042	1.573	2.67
-10	0.440	5.4198	-0.044	2.127	1.96
-9	0.446	5.4192	-0.046	2.247	1.60
-8	0.451	5.4186	-0.047	2.247	1.50
-7	0.457	5.41795	-0.048	2.524	1.27
-6	0.463	5.4173	-0.049	2.543	1.15
-5	0.470	5.4166	-0.051	2.627	1.13
-4	0.477	5.4158	-0.052	2.749	0.98
-3	0.485	5.4149	-0.054	2.842	0.90
-2	0.493	5.4140	-0.056	2.933	0.89
-1	0.501	5.4130	-0.058	3.088	0.81
0	0.511	5.41185	-0.060	3.207	0.73
1	0.520	5.41065	-0.063	3.440	0.68
3	0.543	5.40785	-0.068	3.646	0.71
5	0.569	5.4044	-0.075	4.123	0.72
10	0.656	5.3917	-0.101	5.403	0.75
12	0.703	5.38407	-0.116	6.483	0.98

Table B.2: Measurement and fitting data of blue sideband transitions.



Analytical derivation of the sideband coupling

For controlling the effective sideband coupling, we are interested in the rate at which the sideband transitions will occur. We can analytically calculate this rate for the Duffing oscillator and the quantum Rabi model, thanks to theory Byoung-moo Ann developed during this thesis project.¹

In the derivation of the sideband transition rate, we start with the undriven Hamiltonian $\hat{\mathcal{H}}_D$ in eq. (2.25) of the Duffing model. The first step is going to the system's normal mode basis where the coupling term is eliminated. In this basis, the new qubit-like operator $\hat{\beta}$ and cavity-like operator $\hat{\alpha}$ are linear combinations of \hat{b} and \hat{a} , respectively. The dressed states $|e, 0\rangle$ and $|g, 1\rangle$ are eigenstates of the new normal mode Hamiltonian, with $\tilde{\omega}_q$ and $\tilde{\omega}_c$ as corresponding eigenvalues. This Hamiltonian is given by

$$\hat{\mathcal{H}}'_D = \tilde{\omega}_q \hat{\beta}^\dagger \hat{\beta} + \tilde{\omega}_c \hat{\alpha}^\dagger \hat{\alpha} - \frac{1}{12} [\chi_q^{1/4} (\hat{\beta} + \hat{\beta}^\dagger) + \chi_c^{1/4} (\hat{\alpha} + \hat{\alpha}^\dagger)]^4 \quad (\text{C.1})$$

[41], where χ_q and χ_c are the self-Kerr of the qubit and cavity, respectively. Subsequently, we add the drive to the system. Strictly speaking, this drive only acts directly on the qubit through $(\hat{b} + \hat{b}^\dagger)$, but since we operate in the dispersive coupling regime we approximate \hat{b} in $\hat{\mathcal{H}}_d$ by $\hat{\beta}$.² Thus, we have

$$\hat{\mathcal{H}}'_d = 2\epsilon_d \cos(\omega_d t) (\hat{\beta} + \hat{\beta}^\dagger). \quad (\text{C.2})$$

To go to the displaced frame of the drive, we apply the Schrieffer-Wolff transformation \hat{U}' of eq. (2.41) but with normal mode operators $\hat{\beta}$ and $\hat{\beta}^\dagger$ instead. We use the same $\xi(t)$ as before as well, but now replace ω_q by the dressed qubit frequency $\tilde{\omega}_q$,

$$\xi(t) = \frac{\epsilon_d}{\tilde{\Delta}_{dq}} e^{-i\omega_d t} - \frac{\epsilon_d}{\tilde{\Sigma}_{dq}} e^{+i\omega_d t}, \quad (\text{C.3})$$

with $\tilde{\Delta}_{dq} = \omega_d - \tilde{\omega}_q$ and $\tilde{\Sigma}_{dq} = \omega_d + \tilde{\omega}_q$. This leads us to the displaced Hamiltonian

$$\begin{aligned} \hat{\mathcal{H}}''_D &= \hat{U} (\hat{\mathcal{H}}'_D + \hat{\mathcal{H}}'_d) \hat{U}^\dagger + i(\partial_t \hat{U}) \hat{U}^\dagger \\ &= \tilde{\omega}_q \hat{\beta}^\dagger \hat{\beta} + \tilde{\omega}_c \hat{\alpha}^\dagger \hat{\alpha} - \frac{1}{12} [\chi_q^{1/4} (\hat{\beta} + \hat{\beta}^\dagger + \xi + \xi^*) + \chi_c^{1/4} (\hat{\alpha} + \hat{\alpha}^\dagger)]^4. \end{aligned} \quad (\text{C.4})$$

We clearly recognize the dressed qubit and cavity states in the first two terms of the second line. In this basis, the interactions are mediated by the sideband drive, so we find the sideband coupling in the terms between the square brackets. When we write out these terms, only those dependent on ξ are relevant, since they represent

¹Therefore it has not yet been published. This derivation will be submitted for publication.

²Note that this is a similar approximation as in section 2.3.3 where we assumed the drive to only affect the qubit transition frequencies and not those of the cavity.

the effect of the drive on the system. To obtain the sideband coupling to first-order we keep only the first-order cross-terms of the normal mode operators. This gives us

$$-\frac{1}{12} \left[\chi_q^{1/4} (\hat{\beta} + \hat{\beta}^\dagger + \xi + \xi^*) + \chi_c^{1/4} (\hat{\alpha} + \hat{\alpha}^\dagger) \right]^4 \chi_q^{3/4} \chi_c^{1/4} (\xi + \xi^*)^2 (\hat{\beta} + \hat{\beta}^\dagger)(\hat{\alpha} + \hat{\alpha}^\dagger) + \mathcal{O}. \quad (\text{C.5})$$

We see that the sideband coupling is given by the prefactor $\chi_q^{3/4} \chi_c^{1/4} (\xi + \xi^*)^2$. If we remove all terms oscillating at $2\omega_d$, we arrive at the Duffing model's sideband transition rate

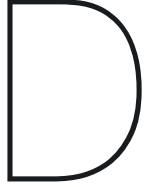
$$\Omega_{sb} = 2\chi_q^{3/4} \chi_c^{1/4} \epsilon_d^2 \left(\frac{1}{\tilde{\Delta}_{dq}^2} + \frac{1}{\tilde{\Sigma}_{dq}^2} - \frac{2}{\tilde{\Delta}_{dq} \tilde{\Sigma}_{dq}} \right), \quad (\text{C.6})$$

where the qubit's self-Kerr is given by

$$\chi_q = E_C \left(1 - 4g^2 \frac{\omega_c}{\omega_q} \frac{\omega_q^2 - \omega_c^2}{\Delta_{dq}^2 \Sigma_{dq}^2} \right) \quad (\text{C.7})$$

[41]. Note that in eq. (C.7), g is the bare qubit-cavity coupling strength and Δ_{dq} , Σ_{dq} consider the undressed ω_q . The cavity's self-Kerr χ_c is related to χ_q through the cross-Kerr as $\chi_{qc} = \sqrt{\chi_q \chi_c}$, which can be calculated by diagonalization of the undriven Hamiltonian $\hat{\mathcal{H}}_D$ as $2\chi_{qc} = (E_{|e0\rangle} - E_{|g1\rangle}) - (E_{|e1\rangle} - E_{|g2\rangle})$.

From eq. (C.6) we see that the transition rate scales quadratically with the drive strength and linear with drive power. From this formula we can also expect that the blue transitions will be characterized by a faster rate than the red (for equal ϵ_d), for $\tilde{\Delta}_{dq}$ will be much smaller than in the red case, having a large impact on Ω_{sb} .



Drive effects on the qubit

To calculate the effect of the drive on the Duffing or Kerr oscillator's resonance frequency, we apply a mathematical transformation that will provide us with insight in the system dynamics.¹ The first step is moving to the displaced frame of the drive by the unitary Schrieffer-Wolff transformation

$$\hat{\mathcal{U}} = e^{-\xi(t)\hat{b}^\dagger + \xi^*(t)\hat{b}} \quad (\text{D.1})$$

[40]. Not discriminating between the Kerr and Duffing oscillator, this transformation simply displaces the field \hat{b} to $\hat{b} + \xi(t)$ and \hat{b}^\dagger to $\hat{b}^\dagger + \xi^*(t)$. The parameter $\xi(t)$ is defined through the differential equation of motion

$$\partial_t \xi(t) = -i\omega_q \xi(t) - i\epsilon_d (e^{-i\omega_d t} + e^{+i\omega_d t}) \quad (\text{D.2})$$

[40]. The general solution to this is

$$\xi(t) = c_1 e^{-i\omega_q t} + \frac{\epsilon_d}{\Delta_{dq}} e^{-i\omega_d t} - \frac{\epsilon_d}{\Sigma_{dq}} e^{+i\omega_d t}, \quad (\text{D.3})$$

where $\Delta_{dq} = \omega_d - \omega_q$ and $\Sigma_{dq} = \omega_d + \omega_q$. The drive amplitude $2\epsilon_d$ is assumed to be real-valued. The first term can be dropped by choosing the arbitrary constant c_1 zero. The transformed Hamiltonian is obtained from

$$\hat{\mathcal{H}}' = \hat{\mathcal{U}} \hat{H} \hat{\mathcal{U}}^\dagger + i(\partial_t \hat{\mathcal{U}}) \hat{\mathcal{U}}^\dagger \quad (\text{D.4})$$

The first term transfers all $\hat{b} \rightarrow \hat{b} + \xi(t)$ and $\hat{b}^\dagger \rightarrow \hat{b}^\dagger + \xi^*(t)$. Then the second term, together with $\omega_q(\xi(t)^*\hat{b} + \xi(t)\hat{b}^\dagger)$ produced from the first, cancels the drive:

$$i(\partial_t \hat{\mathcal{U}}) \hat{\mathcal{U}}^\dagger + \omega_q (\xi^*(t)\hat{b} + \xi(t)\hat{b}^\dagger) = \epsilon_d \cos(\omega_d t) (\hat{b} + \hat{b}^\dagger). \quad (\text{D.5})$$

D.1 Kerr oscillator

Now let's first consider the Kerr Hamiltonian of eq. (2.27). The resulting transformed Kerr Hamiltonian in the displaced frame of the drive is

$$\hat{\mathcal{H}}'_K = \omega_q \hat{b}^\dagger \hat{b} - \frac{E_C}{2} (\hat{b}^\dagger + \xi^*)^2 (\hat{b} + \xi)^2 + \omega_c \hat{a}^\dagger \hat{a} - g (\hat{b} + \hat{b}^\dagger + \xi + \xi^*) (\hat{a} + \hat{a}^\dagger), \quad (\text{D.6})$$

where the explicit time dependence of ξ is dropped for the sake of readability. The qubit's frequency modulation then follows from the second term in eq. (D.6). If we dissolve that term, we have

$$-\frac{E_C}{2} (\hat{b}^\dagger + \xi^*)^2 (\hat{b} + \xi)^2 - \frac{E_C}{2} (\hat{b}^\dagger \hat{b}^\dagger \hat{b} \hat{b} + 4\xi^* \xi \hat{b}^\dagger \hat{b}) + \text{off-diagonal} + \phi, \quad (\text{D.7})$$

¹This method has been worked out by Byoung-moo Ann and will be submitted for publication.

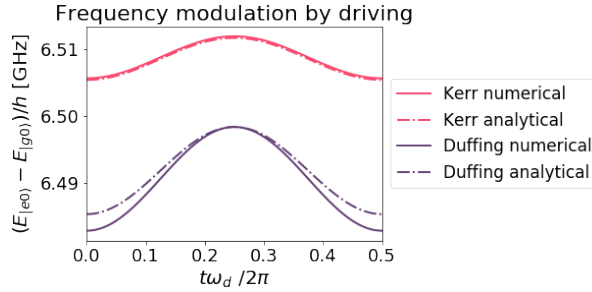


Figure D.1: Frequency modulation by driving in the driven Duffing and Kerr model. Analytically, it is calculated according to eq. (2.43) and eq. (D.8). The numerical values are obtained by direct diagonalization of $\hat{\mathcal{H}}_D + \hat{\mathcal{H}}_d$ and $\hat{\mathcal{H}}_K + \hat{\mathcal{H}}_d$ for different values of t . The parameters are $\omega_q/2\pi = 6.5$ GHz, $\epsilon_d/2\pi = 0.4$ GHz, and $\omega_d/2\pi = 1.25$ GHz.

where ϕ denotes a global phase shift to the system. The off-diagonal elements are non-conserving terms and therefore do not contribute to the modulation. The modulation amplitude is given by the term with $\hat{b}^\dagger \hat{b}$, which adds to the first term in eq. (D.6).

$$\begin{aligned} -4 \frac{E_C}{2} \xi^* \xi &= -2\epsilon_d^2 E_C \left(\frac{1}{\Delta_{dq}^2} + \frac{1}{\Sigma_{dq}^2} - \frac{2}{\Delta_{dq}\Sigma_{dq}} \cos 2\omega_d t \right) \\ &= \delta\omega_q + \eta(t). \end{aligned} \quad (\text{D.8})$$

This expression shows us two contributions —a constant frequency shift $\delta\omega_q = -2\epsilon_d^2 E_C (\Delta_{dq}^{-2} + \Sigma_{dq}^{-2})$ and an oscillating part $\eta(t) = 4\epsilon_d^2 E_C / (\Delta_{dq}\Sigma_{dq}) \cos 2\omega_d t$ at twice the drive frequency. The effects of both terms will become clear from chapters 3 and 4.

D.2 Duffing oscillator

If we instead consider the Duffing Hamiltonian of eq. (2.25), $\hat{\mathcal{U}}$ displaces $-\frac{E_C}{12}(\hat{b}^\dagger + \hat{b})$ to

$$-\frac{E_C}{12} (\hat{b} + \hat{b}^\dagger + \xi + \xi^*)^4 = 6\hat{b}^\dagger \hat{b}^\dagger \hat{b} \hat{b} + 12\hat{b}^\dagger \hat{b} + 12(\xi + \xi^*)^2 \hat{b}^\dagger \hat{b} + \text{off-diagonal} + \phi. \quad (\text{D.9})$$

Again, we are not interested in the off-diagonal elements and the global phase shift ϕ . The Duffing oscillator's modulation amplitude is then given by

$$\begin{aligned} \delta\omega_q + \eta(t) &= -12 \frac{E_C}{12} (\xi + \xi^*)^2 \\ &= -2\epsilon_d^2 E_C \left(\frac{1}{\Delta_{dq}^2} + \frac{1}{\Sigma_{dq}^2} - \frac{2}{\Delta_{dq}\Sigma_{dq}} \right) (1 + \cos 2\omega_d t). \end{aligned} \quad (\text{D.10})$$

We see that the Duffing oscillator experiences a constant frequency shift $\delta\omega_q$ and an oscillating shift $\eta(t)$ as well. The oscillating part has the same $2\omega_d$ frequency as with the Kerr oscillator. The difference is that the amplitude of $\delta\omega_q$ and of $\eta(t)$ are equal now. We can see the difference in amplitude clearly from fig. D.1, where the analytical qubit shifts by driving are plotted against direct diagonalization of the driven $\hat{\mathcal{H}}_D$ and $\hat{\mathcal{H}}_K$.

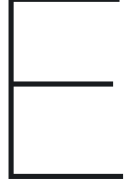
D.3 Two-level system

In the case of a two-level qubit, the qubit's frequency shift under driving is a well-known and explored effect, and it is calculated by means of second-order perturbation theory. The shift $\delta\omega_q$ is given by the sum of the AC-Stark

shift [18] and the additional Bloch-Siegert shift:

$$\delta\omega_q = \underbrace{\frac{(2\epsilon_d)^2}{2(\omega_q - \omega_d)}_{\text{AC-Stark}}} + \underbrace{\frac{(2\epsilon_d)^2}{2(\omega_q + \omega_d)}_{\text{Bloch-Siegert}}} = 2\epsilon_d^2 \left(\frac{1}{\Delta_{qd}} + \frac{1}{\Sigma_{qd}} \right). \quad (\text{D.11})$$

The AC Stark shift is given by the difference frequency term and the Bloch-Siegert shift by the sum frequency term. In literature, it is common to neglect the Bloch-Siegert shift, since in many cases it is much smaller than the AC Stark shift. However, with a red sideband drive, for example, ω_d is far detuned from ω_q and the Bloch-Siegert shift cannot be neglected. Note that eq. (D.11) is only accurate in the limit where the drive tone is sufficiently detuned from the qubit frequency so that the first term does not diverge.



Derivation of the sideband fitting models

E.1 Blue sideband transitions

To fit the blue sideband measurement data, we use a simplified model that contains only the relevant interactions at the sideband resonance condition. We start with the Hamiltonian in the normal mode basis:

$$\begin{aligned} \hat{\mathcal{H}}_{f,B} = & \tilde{\omega}_q \hat{\beta}^\dagger \hat{\beta} - \frac{\tilde{\zeta}_q}{2} \hat{\beta}^\dagger \hat{\beta}^\dagger \hat{\beta} \hat{\beta} + \tilde{\omega}_c \hat{\alpha}^\dagger \hat{\alpha} - 2\chi_{qc} \hat{\beta}^\dagger \hat{\beta} \hat{\alpha}^\dagger \hat{\alpha} \\ & + g_{sb} (\hat{\alpha} \hat{\beta} + \hat{\alpha}^\dagger \hat{\beta}^\dagger) \cos 2\omega_d t + \epsilon_p (\hat{\alpha} + \hat{\alpha}^\dagger) \cos \omega_p t, \end{aligned} \quad (\text{E.1})$$

where $2\omega_d = \tilde{\omega}_q + \tilde{\omega}_c + \delta\omega_q$, and ϵ_p is the probe strength. At the sideband resonance condition, $2\omega_d$ is at resonance with the transitions $\hat{\alpha}\hat{\beta}$ and $\hat{\alpha}^\dagger\hat{\beta}^\dagger$ induce. Specifically,

$$|2\omega_d - (E_{|e1\rangle} - E_{|g0\rangle})| \ll 2\omega_d + (E_{|e1\rangle} - E_{|g0\rangle}). \quad (\text{E.2})$$

Together with the fact that $g_{sb} \ll 2\omega_d$, it is valid to apply a RWA on the counter-rotating terms in the second line of eq. (E.1). The same argumentation holds for the probe term. ω_p is at resonance with the transitions induced by $\hat{\alpha}$ and $\hat{\alpha}^\dagger$ and we keep ϵ_p as small as possible. This gives us the Hamiltonian within the RWA:

$$\begin{aligned} \hat{\mathcal{H}}_{f,B} \simeq & \tilde{\omega}_q \hat{\beta}^\dagger \hat{\beta} - \frac{\tilde{\zeta}_q}{2} \hat{\beta}^\dagger \hat{\beta}^\dagger \hat{\beta} \hat{\beta} + \tilde{\omega}_c \hat{\alpha}^\dagger \hat{\alpha} - 2\chi_{qc} \hat{\beta}^\dagger \hat{\beta} \hat{\alpha}^\dagger \hat{\alpha} \\ & + g_{sb} (\hat{\alpha} \hat{\beta} e^{-2i\omega_d t} + \hat{\alpha}^\dagger \hat{\beta}^\dagger e^{+2i\omega_d t}) + \epsilon_p (\hat{\alpha} e^{-i\omega_p t} + \hat{\alpha}^\dagger e^{+i\omega_p t}), \end{aligned} \quad (\text{E.3})$$

To remove the time dependence, we move to a rotating frame through the unitary operator

$$\hat{U} = \exp [i\omega_p t \hat{a}^\dagger \hat{a} + i(2\omega_d - \omega_p) t \hat{b}^\dagger \hat{b}]. \quad (\text{E.4})$$

This results in our simplified model for the blue sideband transitions:

$$\begin{aligned} \hat{\mathcal{H}}'_{f,B} = & (\tilde{\omega}_q - 2\omega_d + \omega_p) \hat{\beta}^\dagger \hat{\beta} - \frac{\tilde{\zeta}_q}{2} \hat{\beta}^\dagger \hat{\beta}^\dagger \hat{\beta} \hat{\beta} + (\tilde{\omega}_c - \omega_p) \hat{\alpha}^\dagger \hat{\alpha} - 2\chi_{qc} \hat{\beta}^\dagger \hat{\beta} \hat{\alpha}^\dagger \hat{\alpha} \\ & - g_{sb} (\hat{\alpha} \hat{\beta} + \hat{\alpha}^\dagger \hat{\beta}^\dagger) + i\epsilon_p (\hat{\alpha}^\dagger - \hat{\alpha}). \end{aligned} \quad (\text{E.5})$$

E.2 Red sideband transitions

The model for the red sideband transitions is obtained in a similar way. Now we start with the Hamiltonian

$$\begin{aligned}\hat{\mathcal{H}}_{f,B} = & \tilde{\omega}_q \hat{\beta}^\dagger \hat{\beta} - \frac{\tilde{\zeta}_q}{2} \hat{\beta}^\dagger \hat{\beta}^\dagger \hat{\beta} \hat{\beta} + \tilde{\omega}_c \hat{\alpha}^\dagger \hat{\alpha} - 2\chi_{qc} \hat{\beta}^\dagger \hat{\beta} \hat{\alpha}^\dagger \hat{\alpha} \\ & + g_{sb} (\hat{\alpha}^\dagger \hat{\beta} + \hat{\alpha} \hat{\beta}^\dagger) \cos 2\omega_d t + \epsilon_p (\hat{\alpha} + \hat{\alpha}^\dagger) \cos \omega_p t,\end{aligned}\quad (\text{E.6})$$

where the only difference with eq. (E.1) is the transitions induced by the sideband drive. Once again, because $2\omega_d$ is at resonance with $\hat{\alpha}^\dagger \hat{\beta}$, $\hat{\alpha} \hat{\beta}^\dagger$, and ω_p with $\hat{\alpha}$, $\hat{\alpha}^\dagger$, it is justified to apply the RWA on the counter-rotating terms. We obtain

$$\begin{aligned}\hat{\mathcal{H}}_{f,B} \simeq & \tilde{\omega}_q \hat{\beta}^\dagger \hat{\beta} - \frac{\tilde{\zeta}_q}{2} \hat{\beta}^\dagger \hat{\beta}^\dagger \hat{\beta} \hat{\beta} + \tilde{\omega}_c \hat{\alpha}^\dagger \hat{\alpha} - 2\chi_{qc} \hat{\beta}^\dagger \hat{\beta} \hat{\alpha}^\dagger \hat{\alpha} \\ & + g_{sb} (\hat{\alpha}^\dagger \hat{\beta} e^{-2i\omega_d t} + \hat{\alpha} \hat{\beta}^\dagger e^{+2i\omega_d t}) + \epsilon_p (\hat{\alpha} e^{-i\omega_p t} + \hat{\alpha}^\dagger e^{+i\omega_p t}).\end{aligned}\quad (\text{E.7})$$

Finally, removal of the time dependence by moving to a rotating frame, yields our fitting model for the red sideband transitions:

$$\begin{aligned}\hat{\mathcal{H}}'_{f,R} = & (\tilde{\omega}_q - 2\omega_d - \omega_p) \hat{\beta}^\dagger \hat{\beta} - \frac{\tilde{\zeta}_q}{2} \hat{\beta}^\dagger \hat{\beta}^\dagger \hat{\beta} \hat{\beta} \\ & + (\tilde{\omega}_c - \omega_p) \hat{\alpha}^\dagger \hat{\alpha} - 2\chi_{qc} \hat{\beta}^\dagger \hat{\beta} \hat{\alpha}^\dagger \hat{\alpha} - g_{sb} (\hat{\alpha}^\dagger \hat{\beta} + \hat{\alpha} \hat{\beta}^\dagger) + i\epsilon_p (\hat{\alpha}^\dagger - \hat{\alpha}).\end{aligned}\quad (\text{E.8})$$

F

Simulations of the quantum Rabi model

In this appendix, we very briefly show and discuss the results of simulations of sideband transitions in the quantum Rabi model and compare them to those of the Duffing system. We have seen that the transmon qubit can be approximated by an effective two-level system (TLS) if the probability of occupying higher excited states is negligibly small. Specifically, we require $g \ll |\omega_q - \omega_c| \ll E_C$. When we couple the TLS to a cavity we obtain the QRM.

$$\hat{\mathcal{H}}_R = \frac{\hbar}{2}\omega_q\hat{\sigma}_z - \hbar\omega_c\hat{a}^\dagger\hat{a} + \hbar g\hat{\sigma}_x(\hat{a} + \hat{a}^\dagger). \quad (\text{F.1})$$

Subsequently, the famous Jaynes-Cummings Hamiltonian $\hat{\mathcal{H}}_{JC}$ is obtained by the RWA that drops the counter-rotating terms in the interaction, so that we have

$$\hat{\mathcal{H}}_{JC} = \frac{\hbar}{2}\omega_q\hat{\sigma}_z - \hbar\omega_c\hat{a}^\dagger\hat{a} + \hbar g(\hat{a}\hat{\sigma}_+ + \hat{a}^\dagger\hat{\sigma}_-). \quad (\text{F.2})$$

The dropped counter-rotating terms, however, cannot necessarily be neglected in the case of strong coupling g or large detuning between the qubit and cavity [31]. For the conceptual cases considered in this thesis, we use $g = 200$ MHz and $|\Delta_{qc}| = 2.5$ GHz, which is the regime where they play a significant role in the dynamics of the system. That is why for the simulations where we approximate the qubit by a TLS, we will include these counter-rotating terms and use the Rabi Hamiltonian $\hat{\mathcal{H}}_R$ rather than the Jaynes-Cummings Hamiltonian $\hat{\mathcal{H}}_{JC}$.

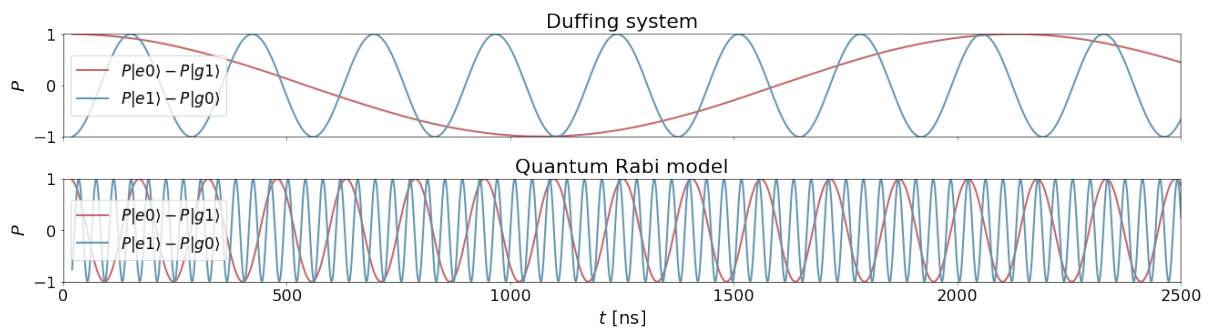


Figure F.1: Time-domain simulation of sideband transitions in the Duffing system and quantum Rabi model. The colour indicates the type of transitions. The sideband transition rate in the quantum Rabi model is much higher than in the Duffings system, because a valid two-level approximation of the transmon corresponds to a very large charging energy E_C . The conceptual parameters from section 3.1.7 are used, together with the covgent method and drive strength $\epsilon_d/2\pi = 0.3$ GHz.

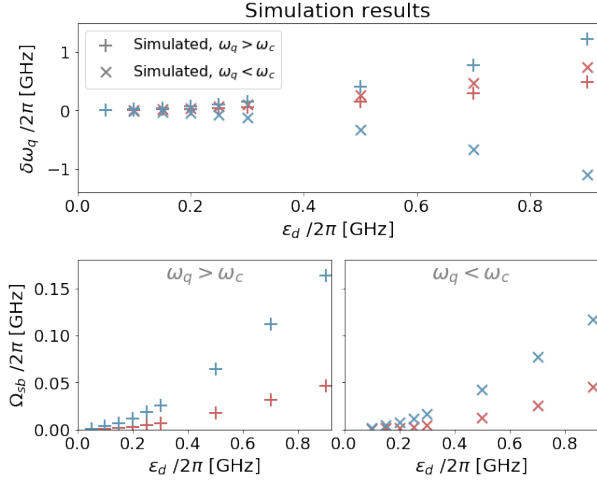


Figure F.2: Numerical simulation results of sideband transitions in the quantum Rabi model. $\omega_q > \omega_c$ corresponds to $\omega_q/2\pi = 6.5$ GHz and $\omega_c/2\pi = 4.0$ GHz, $\omega_q < \omega_c$ to $\omega_q/2\pi = 4.0$ GHz and $\omega_c/2\pi = 6.5$ GHz.

F.1 Results

From fig. F.1 we immediately see that the sideband transitions in the QRM take place at a significantly higher rate than in the Duffing system. This is because what we effectively did by applying the two-level approximation is increasing the charging energy from $E_C = 200$ MHz to $E_C \gg |\Delta_{qc}|$ (since we have chosen g , ω_q , and ω_c to be equal for both the Duffing system and the QRM). From eq. (2.45) and eq. (C.7) we learn that the sideband transition rate Ω_{sb} scales with $\sqrt{E_C}$, so the transition rate is expected to be higher in the QRM.

Beside this quantitative difference to the Duffing oscillator, the simulations show an important qualitative difference as well. For a multi-level Duffing oscillator, the driven qubit shift $\delta\omega_q$ is always negative, regardless of our values ω_q and ω_d . That is because, looking at eq. (2.43), there are no solutions for the inequality

$$\frac{1}{\Delta_{dq}^2} + \frac{1}{\Sigma_{dq}^2} - \frac{2}{\Delta_{dq}\Sigma_{dq}} < 0. \quad (\text{F.3})$$

In fig. F.2, however, we see that when $\omega_q/2\pi = 6.5$ GHz $> \omega_c/2\pi = 4.0$ GHz the driven qubit shift is positive. This can be understood from eq. (D.11), where $\delta\omega_q > 0$ if $\omega_q > \omega_d$. This is the case for both the red and blue sideband transitions if $\omega_q > \omega_c$. When we swap the qubit and cavity frequency such that $\omega_q/2\pi = 4.0$ GHz $< \omega_c/2\pi = 6.5$ GHz, we that, when driven by a blue sideband drive, the qubit frequency does go down. This is because in this case

$$\omega_d = \tilde{\omega}_q + \delta\omega_q \tilde{\omega}_c > \omega_q. \quad (\text{F.4})$$

The red sideband drive still has a smaller frequency than the qubit and thus $\delta\omega_q > 0$.¹

All simulation results for the QRM can be found in appendix H.

¹Note that when $\omega_q < \omega_c$, a positive driven qubit shift $\delta\omega_q$ actually decreases the required drive frequency ω_d for the sideband resonance condition.

G

Bichromatic driving

Up to now, we have only considered monochromatic driving within this thesis. This means that the two photons involved in a sideband transition are of equal energy. Another possible method is to induce the transitions with two photons of different energies, known as bichromatic driving.

The bichromatic drive can be realized in two different ways. It can either be considered as a single drive line carrying a signal with two different frequencies with each a specific amplitude. On the other hand, it may be realized as two separate drive lines, each with its own unique frequency and amplitude. The experimental setup determines which of the two is the case, but for our mathematical description they are one and the same. The frequencies of the two tones can be chosen at will as long as their sum or difference equals the energy gap between the relevant levels [18].

The easiest choice is to tune one tone to be near the qubit frequency and the other near the cavity frequency. This would be like normal spectroscopy, where we induce transitions in the qubit with one tone and in the cavity with the other. However, that way there will be no correlations between the processes in the qubit and those in the cavity, and we will not be able to control the desired sideband transitions [39].

The clever way is to modify both tones by a frequency δ such that their sum and difference frequencies stay fixed. We fix the cavity-friendly drive tone at frequency $\omega_{d_c} = \tilde{\omega}_c - \delta$ with strength ϵ_{d_c} . The qubit-friendly drive tone with frequency $\omega_{d_q} = \tilde{\omega}_q + \delta\omega_q \pm \delta$ and strength ϵ_{d_q} then induces the red (-) or blue (+) sideband transitions. This way, energy conservation is only satisfied when a quantum is exchanged between the qubit and cavity (red transition), or when both are simultaneously (de)excited (blue transition) [39].

The choice of the detuning δ in this setup is important. The drive power that is coupled to the qubit scales with $1/\delta^2$, so small detunings produce high transition rates [18]. On the other hand, as discussed, the detuning should be sufficiently large such that there is no independent absorption and emission [17]. The drive Hamiltonian is the sum of the two separate drive tones.

$$\begin{aligned}\hat{\mathcal{H}}_d &= \hat{\mathcal{H}}_{d_q} + \hat{\mathcal{H}}_{d_c} \\ &= 2\epsilon_{d_q} \cos(\omega_{d_q} t) (\hat{b} + \hat{b}^\dagger) + 2\epsilon_{d_c} \cos(\omega_{d_c} t) (\hat{b} + \hat{b}^\dagger).\end{aligned}\tag{G.1}$$

Appendix H shows the results of the simulations run of bichromatically driven sideband transitions. In these simulations $\epsilon_{d_c} \gg \epsilon_{d_q}$. This is because both drive tones operate on the qubit, so the cavity-friendly drive strength is needed to be larger for better effective coupling to the cavity.



Simulation results

This appendix contains the results of numerical time-domain simulations of sideband transitions. These are performed with the use of the Python QuTiP package [48, 49] and Python code specifically developed for this thesis.¹ The detailed methodology is described in section 3.1.

There are two sets of simulations performed, each with its own parameters. The first set is of the experimental chip. The parameters are obtained by the methods explained in section 3.2: $\omega_q/2\pi = 6.807$ GHz, $\omega_c/2\pi = 4.0928$ GHz, $E_C/h = 0.138$ GHz, $g/2\pi = 0.193$ GHz. For both the qubit and cavity 10 energy levels are incorporated. The system is approximated by a Duffing oscillator coupled to a cavity. This system is described by $\hat{\mathcal{H}}_D$ of eq. (2.25). The drive is monochromatic and given by $\hat{\mathcal{H}}_d$ of eq. (2.38).

The second set of simulations is based on conceptual parameters. Here we use $E_C/h = g/2\pi = 0.2$ GHz. For the qubit and cavity frequencies there are two possibilities chosen. Either $\omega_q/2\pi = 6.5$ GHz > $\omega_c/2\pi = 4.0$ GHz, or $\omega_q/2\pi = 4.0$ GHz < $\omega_c/2\pi = 6.5$ GHz. Simulations are performed for a Duffing oscillator, Kerr oscillator, and a TLS. The Duffing and Kerr oscillators have 10 energy levels included. The sideband transitions with the TLS are in practice performed with $\hat{\mathcal{H}}_K$ with the restriction that the qubit has only two levels. Note that in this case, the Kerr non-linearity $\frac{E_C}{2} \hat{b}^\dagger \hat{b}^\dagger \hat{b} \hat{b}$ returns the zero matrix.

In the case of conceptual parameters there are two types of drive used —monochromatic (section 2.3.1) and bichromatic driving (appendix G). In the table on the next pages, dw is the detuning δ of the cavity-friendly drive tone ω_{d_e} from the undressed cavity frequency ω_c . c_{eps} is the drive factor c_ϵ that determines the strength of both the qubit-friendly and cavity-friendly drive tone:

$$\begin{aligned}\epsilon_{d_q} &= c_\epsilon \cdot 0.025 \text{ GHz}, \\ \epsilon_{d_c} &= c_\epsilon \cdot 0.317 \text{ GHz}.\end{aligned}\tag{H.1}$$

The last column in the table is a measure for the effect of the drive on the dressed energy levels. Specifically, it shows by how much the required $\omega_{d_{(q)}}$ for the sideband resonance condition deviates from the energy spacing between the dressed, undriven energy levels that are involved in the sideband transition. Note that this is similar to $\delta\omega_q$, expect for the red sideband transition when $\omega_q < \omega_c$.

Some simulations are performed for special situations or an adjusted model. These cases are presented in separate boxes. Supplementary notes are provided if necessary.

An Excel format of the table is publicly available at the GitHub repository of this thesis.¹

The main platform for simulating sideband transitions is the Jupyter notebook `2p_sideband.ipynb`.¹ Beside the main code, this notebook contains extensive descriptions of the usage of the code so that it is readily available for anyone who is interested in using it.

¹ <https://github.com/wouterkesselsap/thesis>

# of qubit levels	undressed qubit freq.						Drive tones	Drive strength	eps factor	Type of transition	Qubit model	Cavity-friendly detuning	Drive freq.	Qubit-friendly drive freq.	Cavity-friendly drive freq.	Notes	Transition rate (simulated)	Transition rate (theoretical)	Om_sb_sm / Om_sb_lh	Om_sb_sm - Om_sb_lh	Deviation of drive frequency from undriven coupled case (simulated)	
	Nq	wq	wc	Nt	eps	c_eps	SB	dw	wd	wdq	woc	Om_sb_sim	Om_sb_th									
Experimental device																						
10	6.807	4.0928	single	0.2		red	Duffing		1.36736								0.0001082	0.0001087	1.00	-0.000001	-0.001	
10	6.807	4.0928	single	0.3		red	Duffing		1.36660								0.0002441	0.0002446	1.00	-0.000001	-0.003	
10	6.807	4.0928	single	0.4		red	Duffing		1.36556								0.0004334	0.0004349	1.00	-0.000001	-0.005	
10	6.807	4.0928	single	0.5		red	Duffing		1.36420								0.0006784	0.0006793	1.00	-0.000001	-0.008	
10	6.807	4.0928	single	0.6		red	Duffing		1.3625								0.0009815	0.0009781	1.00	0.000003	-0.011	
10	6.807	4.0928	single	0.7		red	Duffing		1.3603								0.001462	0.0013309	1.10	0.000131	-0.015	
10	6.807	4.0928	single	0.9		red	Duffing		1.3554								0.002291	0.0021987	1.04	0.000093	-0.025	
10	6.807	4.0928	single	0.2		blue	Duffing		5.4375								0.0007594	0.0007646	0.99	-0.000005	-0.009	
10	6.807	4.0928	single	0.3		blue	Duffing		5.4318								0.001719	0.0017077	1.01	0.000011	-0.020	
10	6.807	4.0928	single	0.4		blue	Duffing		5.4238								0.003103	0.0030048	1.03	0.000098	-0.036	
10	6.807	4.0928	single	0.5		blue	Duffing		5.4131								0.004899	0.0046312	1.06	0.000267	-0.058	
10	6.807	4.0928	single	0.6		blue	Duffing		5.4002								0.007200	0.0065611	1.10	0.000639	-0.084	
10	6.807	4.0928	single	0.7		blue	Duffing		5.3843								0.009999	0.0087547	1.14	0.001244	-0.115	
10	6.807	4.0928	single	0.9		blue	Duffing		5.3460								0.01812	0.0138098	1.31	0.004313	-0.192	
10	6.807	4.0928	single	0.2		red	Kerr		1.37045													
10	6.807	4.0928	single	0.3		red	Kerr		1.37011								0.00009646	0.0002447	0.39	-0.000148	0.026	
10	6.807	4.0928	single	0.4		red	Kerr		1.36962								0.0001720	0.0004351	0.40	-0.000263	0.025	
10	6.807	4.0928	single	0.5		red	Kerr		1.36901								0.0002682	0.0006798	0.39	-0.000412	0.024	
10	6.807	4.0928	single	0.6		red	Kerr		1.3682								0.0003965	0.0009787	0.41	-0.000582	0.022	
10	6.807	4.0928	single	0.7		red	Kerr		1.3673								0.0005348	0.0013320	0.40	-0.000797	0.020	
10	6.807	4.0928	single	0.9		red	Kerr		1.3652								0.0008842	0.0022014	0.40	-0.001317	0.016	
10	6.807	4.0928	single	0.2		blue	Kerr		5.4424								0.0004543	0.0007695	0.59	-0.000315	-0.015	
10	6.807	4.0928	single	0.3		blue	Kerr		5.4384								0.001014	0.0017223	0.59	-0.000708	-0.023	
10	6.807	4.0928	single	0.4		blue	Kerr		5.4327								0.001807	0.0030394	0.59	-0.001232	-0.034	
10	6.807	4.0928	single	0.5		blue	Kerr		5.4254								0.002842	0.0047046	0.60	-0.001863	-0.049	
10	6.807	4.0928	single	0.6		blue	Kerr		5.4164								0.004125	0.0066970	0.62	-0.002572	-0.067	
10	6.807	4.0928	single	0.7		blue	Kerr		5.4057								0.005648	0.0089925	0.63	-0.003344	-0.088	
10	6.807	4.0928	single	0.9		blue	Kerr		5.3791								0.009512	0.0143790	0.66	-0.004867	-0.142	
10	6.807	4.0928	single	0.4		red	Duffing		1.36549								Sixth-order cosine					
10	6.807	4.0928	single	0.7		red	Duffing		1.3605								0.0004371					
10	6.807	4.0928	single	0.4		blue	Duffing		5.4236								0.001339					
10	6.807	4.0928	single	0.7		blue	Duffing		5.3846								0.003095					
10	6.807	4.0928	single	0.7		red	Duffing		1.3174								Incl. higher cavity mode					
10	6.807	4.0928	single	0.7		blue	Duffing		5.332								0.001479	0.0011688			-0.015	
10	6.807	4.0928	single	0.7		blue	Duffing		5.382								0.01138	0.007250			-0.125	
10	6.805	4.0928	single	0.7		blue	Duffing		5.384								g = 0.209, Ec = 0.1385				-0.116	
10	6.809	4.0928	single	0.7		blue	Duffing		5.384								g = 0.174, Ec = 0.138				-0.120	
Conceptual Duffing system																						
10	6.5	4	single	0.2		red	Duffing		1.2584								0.0002106	0.0001880	1.12	0.000023	-0.002	
10	6.5	4	single	0.3		red	Duffing		1.2571								0.0004760	0.0004230	1.13	0.000053	-0.005	
10	6.5	4	single	0.4		red	Duffing		1.2552								0.0008513	0.0007518	1.13	0.000099	-0.008	
10	6.5	4	single	0.5		red	Duffing		1.2529								0.001328	0.0011744	1.13	0.000154	-0.013	
10	6.5	4	single	0.6		red	Duffing		1.2500								0.001923	0.0016905	1.14	0.000233	-0.019	
10	6.5	4	single	0.7		red	Duffing		1.2465								0.002641	0.0023000	1.15	0.000341	-0.026	
10	6.5	4	single	0.9		red	Duffing		1.2380								0.004443	0.0037981	1.17	0.000644	-0.043	
10	6.5	4	single	0.2		blue	Duffing		5.2274								0.001606	0.0013961	1.15	0.000210	-0.018	
10	6.5	4	single	0.3		blue	Duffing		5.2158								0.003678	0.0030906	1.19	0.000587	-0.041	
10	6.5	4	single	0.4		blue	Duffing		5.1988								0.006717	0.0053678	1.25	0.001349	-0.075	
10	6.5	4	single	0.5		blue	Duffing		5.1767								Irregular expectation peaks					
10	6.5	4	single	0.6		blue	Duffing		5.1447								0.01048	0.0081401	1.29	0.002340	-0.119	
10	6.5	4	single	0.7		blue	Duffing		5.1078								0.01597	0.0112362	1.42	0.004737	-0.183	
10	6.5	4	single	0.9		blue	Duffing		5.0245								Shift not observable with probe					
10	4	6.5	single	0.2		red	Duffing		1.2833								0.02221	0.0145860	1.52	0.007624	-0.257	
10	4	6.5	single	0.3		red	Duffing		1.2884								0.03798	0.0217774	1.74	0.016200	-0.424	
10	4	6.5	single	0.4		red	Duffing		1.2958								0.0005165	0.0004040	1.30	0.000119	0.008	
10	4	6.5	single	0.5		red	Duffing		1.3064								0.001128	0.000990	1.26	0.000232	0.018	
10	4	6.5	single	0.6		red	Duffing		1.3187								0.001996	0.00160	1.25	0.000398	0.033	
10	4	6.5	single	0.7		red	Duffing		1.3350								0.003153	0.00251	1.26	0.000647	0.054	
10	4	6.5	single	0.9		red	Duffing		1.3816								0.004547	0.00363	1.25	0.000922	0.079	
10	4	6.5	single	0.2		blue	Duffing		5.2283								0.006282	0.00496	1.27	0.001318	0.112	
10	4	6.5	single	0.3		blue	Duffing		5.2230								0.01132	0.00835	1.36	0.002970	0.205	
10	4	6.5	single	0.4		blue	Duffing		5.2156								0.0005638	0.00064	0.88	-0.000074	-0.008	
10	4	6.5	single	0.5		blue	Duffing		5.2060								0.001269					

10	4	6.5	double	2	red	Duffing	0.5	3.4002	6	0.001510	-0.158
10	4	6.5	double	2.5	red	Duffing	0.5	3.3798	6	0.002294	-0.179
10	4	6.5	double	3	red	Duffing	0.5			Extremely chaotic, no transitions	
10	4	6.5	double	1	blue	Duffing	0.5	4.4573	6	0.0005706	-0.008
10	4	6.5	double	1.5	blue	Duffing	0.5	4.4468	6	0.0007796	-0.018
10	4	6.5	double	2	blue	Duffing	0.5	4.4325	6	0.001385	-0.032
10	4	6.5	double	2.5	blue	Duffing	0.5	4.4147	6	0.002148	-0.050
10	4	6.5	double	3	blue	Duffing	0.5	4.3929	6	0.003091	-0.072

10	6.5	4	single	0.3	red	Duffing	1.2586	No CR drive terms	0.0001664	
10	6.5	4	single	0.7	red	Duffing	1.2549	No CR drive terms	0.0009120	
10	6.5	4	single	0.3	blue	Duffing	5.2200	No CR drive terms	0.002902	
10	6.5	4	single	0.7	blue	Duffing	5.1389	No CR drive terms	0.01712	

Conceptual Kerr system											
10	6.5	4	single	0.2	red	Kerr	1.2654		0.000079	-0.001	
10	6.5	4	single	0.3	red	Kerr	1.2648		0.000170	-0.002	
10	6.5	4	single	0.4	red	Kerr	1.2641		0.000307	-0.004	
10	6.5	4	single	0.5	red	Kerr	1.2631		0.000488	-0.006	
10	6.5	4	single	0.6	red	Kerr	1.2619		0.000691	-0.008	
10	6.5	4	single	0.7	red	Kerr	1.2605		0.000943	-0.011	
10	6.5	4	single	0.9	red	Kerr	1.2569		0.001568	-0.018	
10	6.5	4	single	0.2	blue	Kerr	5.2387		0.0009179	-0.012	
10	6.5	4	single	0.3	blue	Kerr	5.2316		0.00198	-0.026	
10	6.5	4	single	0.4	blue	Kerr	5.2212		0.00355	-0.047	
10	6.5	4	single	0.5	blue	Kerr	5.2078		0.00560	-0.074	
10	6.5	4	single	0.6	blue	Kerr	5.1909		0.00814	-0.107	
10	6.5	4	single	0.7	blue	Kerr	5.1704		0.01122	-0.148	
10	6.5	4	single	0.9	blue	Kerr					
10	4	6.5	single	0.2	red	Kerr	1.2675		0.0001758	0.003	
10	4	6.5	single	0.3	red	Kerr	1.2695		0.000371	0.007	
10	4	6.5	single	0.4	red	Kerr	1.2721		0.000665	0.012	
10	4	6.5	single	0.5	red	Kerr	1.2754		0.000983	0.019	
10	4	6.5	single	0.6	red	Kerr	1.2796		0.001402	0.027	
10	4	6.5	single	0.7	red	Kerr	1.2845		0.00194	0.037	
10	4	6.5	single	0.9	red	Kerr	1.2965		0.003177	0.061	
10	4	6.5	single	0.2	blue	Kerr	5.2405		0.0007755	-0.009	
10	4	6.5	single	0.3	blue	Kerr	5.2352		0.001726	-0.020	
10	4	6.5	single	0.4	blue	Kerr	5.2276		0.003057	-0.035	
10	4	6.5	single	0.5	blue	Kerr	5.2179		0.004736	-0.054	
10	4	6.5	single	0.6	blue	Kerr	5.2061		0.006772	-0.078	
10	4	6.5	single	0.7	blue	Kerr	5.1922		0.009120	-0.106	
10	4	6.5	single	0.9	blue	Kerr	5.1581		0.01471	-0.174	
10	6.5	4	double	1	red	Kerr	0.5	6.0243	3.5		
10	6.5	4	double	1.5	red	Kerr	0.5	6.0147	3.5		
10	6.5	4	double	2	red	Kerr	0.5	6.0017	3.5		
10	6.5	4	double	2.5	red	Kerr	0.5	5.9845	3.5		
10	6.5	4	double	3	red	Kerr	0.5	5.9630	3.5		
10	6.5	4	double	1	blue	Kerr	0.5	6.9829	3.5		
10	6.5	4	double	1.5	blue	Kerr	0.5	6.9748	3.5		
10	6.5	4	double	2	blue	Kerr	0.5	6.9629	3.5		
10	6.5	4	double	2.5	blue	Kerr	0.5	6.9485	3.5		
10	6.5	4	double	3	blue	Kerr	0.5	6.9299	3.5		
10	4	6.5	double	1	red	Kerr	0.5	3.4576	6		
10	4	6.5	double	1.5	red	Kerr	0.5	3.4449	6		
10	4	6.5	double	2	red	Kerr	0.5	3.4273	6		
10	4	6.5	double	2.5	red	Kerr	0.5	3.4050	6		
10	4	6.5	double	3	red	Kerr	0.5	3.3793	6		
10	4	6.5	double	1	blue	Kerr	0.5	4.4799	6		
10	4	6.5	double	1.5	blue	Kerr	0.5	4.4682	6		
10	4	6.5	double	2	blue	Kerr	0.5	4.4518	6		
10	4	6.5	double	2.5	blue	Kerr	0.5	4.4310	6		
10	4	6.5	double	3	blue	Kerr	0.5	4.4061	6		

Conceptual Quantum Rabi model											
2	6.5	4	single	0.1	red	TLS	1.2728		0.0007435	0.007	
2	6.5	4	single	0.1	red	TLS	1.2728		0.0007450	0.007	
2	6.5	4	single	0.15	red	TLS	1.2767		0.001667	0.014	
2	6.5	4	single	0.2	red	TLS	1.2821		0.00294	0.025	
2	6.5	4	single	0.25	red	TLS	1.2890		0.004549	0.039	
2	6.5	4	single	0.3	red	TLS	1.2974		0.006461	0.056	
2	6.5	4	single	0.5	red	TLS	1.3474		0.01697	0.156	
2	6.5	4	single	0.7	red	TLS	1.4171		0.03078	0.295	
2	6.5	4	single	0.9	red	TLS	1.5095		0.04553	0.480	
2	6.5	4	single	0.05	blue	TLS	5.2716		0.0007608	0.004	
2	6.5	4	single	0.1	blue	TLS	5.2781		0.003020	0.017	
2	6.5	4	single	0.15	blue	TLS	5.2887		0.006727	0.038	
2	6.5	4	single	0.2	blue	TLS	5.3032		0.01183	0.067	
2	6.5	4	single	0.25	blue	TLS	5.3224		0.01815	0.106	
2	6.5	4	single	0.3	blue	TLS	5.3452		0.02563	0.151	
2	6.5	4	single	0.5	blue	TLS	5.474		0.06456	0.409	
2	6.5	4	single	0.7	blue	TLS	5.6562		0.11186	0.773	
2	6.5	4	single	0.9	blue	TLS	5.8829		0.16296	1.227	
2	4	6.5	single	0.1	red	TLS	1.2566		0.0004685	-0.011	
2	4	6.5	single	0.1	red	TLS	1.2566		0.0004604	-0.011	
2	4	6.5	single	0.15	red	TLS	1.2497		0.00104	-0.025	
2	4	6.5	single	0.2	red	TLS	1.2402		0.001855	-0.044	

2	4	6.5	single	0.25	red	TLS	1.2281	0.00291	-0.068
2	4	6.5	single	0.3	red	TLS	1.2135	0.004213	-0.097
2	4	6.5	single	0.5	red	TLS	1.1337	0.01215	-0.257
2	4	6.5	single	0.7	red	TLS	1.0248	0.02523	-0.475
2	4	6.5	single	0.9	red	TLS	0.8936	0.04529	-0.737
2	4	6.5	single	0.1	blue	TLS	5.2312	0.001896	-0.010
2	4	6.5	single	0.1	blue	TLS	5.2312	0.001895	-0.010
2	4	6.5	single	0.15	blue	TLS	5.2227	0.004239	-0.027
2	4	6.5	single	0.2	blue	TLS	5.2108	0.007476	-0.050
2	4	6.5	single	0.25	blue	TLS	5.1956	0.01156	-0.081
2	4	6.5	single	0.3	blue	TLS	5.177	0.01644	-0.118
2	4	6.5	single	0.5	blue	TLS	5.0683	0.04267	-0.335
2	4	6.5	single	0.7	blue	TLS	4.9041	0.07652	-0.664
2	4	6.5	single	0.9	blue	TLS	4.6878	0.117058	-1.096
2	6.5	4	double	0.5	red	TLS	0.5	6.061	3.5
2	6.5	4	double	1	red	TLS	0.5	6.1248	3.5
2	6.5	4	double	1.5	red	TLS	0.5	6.2281	3.5
2	6.5	4	double	2	red	TLS	0.5	6.3668	3.5
2	6.5	4	double	2.5	red	TLS	0.5	6.5352	3.5
2	6.5	4	double	3	red	TLS	0.5	6.7317	3.5
2	6.5	4	double	0.5	blue	TLS	0.5	7.0595	3.5
2	6.5	4	double	1	blue	TLS	0.5	7.1204	3.5
2	6.5	4	double	1.5	blue	TLS	0.5	7.2191	3.5
2	6.5	4	double	2	blue	TLS	0.5	7.3519	3.5
2	6.5	4	double	2.5	blue	TLS	0.5	7.5146	3.5
2	6.5	4	double	3	blue	TLS	0.5	7.7032	3.5
2	4	6.5	double	0.5	red	TLS	0.5	3.4568	6
2	4	6.5	double	1	red	TLS	0.5	3.4015	6
2	4	6.5	double	1.5	red	TLS	0.5	3.3125	6
2	4	6.5	double	2	red	TLS	0.5	3.1939	6
2	4	6.5	double	2.5	red	TLS	0.5	3.0511	6
2	4	6.5	double	3	red	TLS	0.5	2.8873	6
2	4	6.5	double	0.5	blue	TLS	0.5	4.4558	6
2	4	6.5	double	1	blue	TLS	0.5	4.3964	6
2	4	6.5	double	1.5	blue	TLS	0.5	4.3012	6
2	4	6.5	double	2	blue	TLS	0.5	4.1747	6
2	4	6.5	double	2.3	blue	TLS	0.5	4.0864	6
2	4	6.5	double	2.4	blue	TLS	0.5	4.0549	6
2	4	6.5	double	2.5	blue	TLS	0.5	4.0229	6
2	4	6.5	double	2.6	blue	TLS	0.5	3.9894	6
2	4	6.5	double	2.7	blue	TLS	0.5	3.9566	6
2	4	6.5	double	3	blue	TLS	0.5	3.8518	6
2	6.5	4	single	0.1	red	TLS	1.2580	g = 0.1 GHz	
2	6.5	4	single	0.3	blue	TLS	5.3452	Smooth gaussian and tg scaling with Omega do NOT improve	
2	6.5	4	single	0.3	blue	TLS	5.3452	Much longer tg worsens	
2	6.5	4	double	1	red	TLS	0.2	Highest combined probability	
2	6.5	4	double	1	blue	TLS	0.2	Cavity peaks at n=1	
2	6.5	4	double	1	blue	TLS	0.2	0.01308	
2	6.5	4	double	1	blue	TLS	0.2	0.01328	

